The Astrophysical Journal, 880:88 (41pp), 2019 August 1 https://doi.org/10.3847/1538-4357/ab2a70

CO ($J = 1$–0) Observations toward Filamentary Molecular Clouds in the Galactic Region with $l = [169.^{\circ}75, 174.^{\circ}75]$, $b = [-0.^{\circ}75, 0.^{\circ}5]$

Fang Xiong[1,2,3], Xuepeng Chen[1,4], Qizhou Zhang[3], Ji Yang[1,4], Min Fang[5], Miaomiao Zhang[1,6], Weihua Guo[1,4], and Li Sun[1,4]

[1] Purple Mountain Observatory, and Key Laboratory of Radio Astronomy, Chinese Academy of Sciences, 8 Yuanhua Road, Nanjing 210034, People's Republic of China; fangxiong@pmo.ac.cn, xpchen@pmo.ac.cn
[2] University of Chinese Academy of Sciences, 19A Yuquan Road, Shijingshan District, Beijing 100049, People's Republic of China
[3] Harvard-Smithsonian Center for Astrophysics, 60 Garden Street, Cambridge, MA 02138, USA
[4] School of Astronomy and Space Science, University of Science and Technology of China, Hefei, Anhui 230026, People's Republic of China
[5] Department of Astronomy, University of Arizona, 933 North Cherry Avenue, Tucson, AZ 85721, USA
[6] Max-Planck-Institut für Astronomie, Königstuhl 17, D-69117 Heidelberg, Germany
Received 2018 November 15; revised 2019 June 7; accepted 2019 June 16; published 2019 July 30

Abstract

We present observations of the CO isotopologues (^{12}CO, ^{13}CO, and C^{18}O) toward the Galactic region with $169.^{\circ}75 \leqslant l \leqslant 174.^{\circ}75$ and $-0.^{\circ}75 \leqslant b \leqslant 0.^{\circ}5$ using the Purple Mountain Observatory 13.7 m millimeter-wavelength telescope. Based on the ^{13}CO ($J = 1 - 0$) data, we find five molecular clouds within the velocity range between -25 and 8 km s^{-1} that are all characterized by conspicuous filamentary structures. We have identified eight filaments with a length of 6.38–28.45 pc, a mean H_2 column density of 0.70×10^{21}–6.53×10^{21} cm^{-2}, and a line mass of 20.24–161.91 $M_{\odot}$ pc^{-1}, assuming a distance of ∼1.7 kpc. Gaussian fittings to the inner parts of the radial density profiles lead to a mean FWHM width of 1.13 ± 0.01 pc. The velocity structures of most filaments present continuous distributions with slight velocity gradients. We find that turbulence is the dominant internal pressure to support the fragmentation of filaments instead of thermal pressure. Most filaments have virial parameters smaller than 2; thus, they are gravitationally bound. Four filaments have an LTE line mass close to the virial line mass. We further extract dense clumps using the ^{13}CO data and find that 64% of the clumps are associated with the filaments. According to the complementary IR data, most filaments have associated Class II young stellar objects. Class I objects are mainly found to be located in the filaments with a virial parameter close to 1. Within two virialized filaments, ^{12}CO outflows have been detected, indicating ongoing star-forming activity therein.

Key words: ISM: clouds – ISM: molecules – ISM: structure – stars: formation

1. Introduction

Filamentary structures are ubiquitous in molecular clouds and have been known for several decades (Schneider & Elmegreen 1979; Bally et al. 1987; Loren 1989; Abergel et al. 1994; Hatchell et al. 2005; Myers 2009). The mid-IR observations conducted by the *Midcourse Space Experiment* (*MSX*; Carey et al. 1998, 2000) and *Spitzer* (Churchwell et al. 2009; Peretto & Fuller 2009) and submillimeter observations conducted by *Herschel* (André et al. 2010; Men'shchikov et al. 2010; Molinari et al. 2010) and *Planck* (Planck Collaboration et al. 2015, 2016) have also demonstrated the omnipresence of filamentary structures in the infrared dark clouds (IRDCs) and cold interstellar medium (ISM). Numerous studies employed the data from previous surveys to identify the large-scale filamentary structures within the Milky Way. Ragan et al. (2014) made use of Galactic Ring Survey (GRS; Jackson et al. 2006) data and identified seven giant filaments with a length of ∼100 pc in the first Galactic quadrant. Wang et al. (2015) found nine prominent filaments with a length of 37–99 pc in the region with $15^{\circ} < l < 56^{\circ}$, $|b| \leqslant 1^{\circ}$ using the *Herschel* Infrared Galactic Plane Survey (Hi-GAL; Molinari et al. 2010). Zucker et al. (2015) investigated the region ($|l| < 62^{\circ}$, $|b| < 1^{\circ}$) covered by the *Spitzer* MIPS Galactic Plane Survey (MIPSGAL; Carey et al. 2009) and found 10 "bone" filaments with a length of 13–52 pc. Li et al. (2016) identified 486 spatially and kinematically coherent filaments with a length of 2–20 pc in the inner Galactic plane based on the APEX Telescope Large Area Survey of the Galaxy (ATLASGAL; Schuller et al. 2009).

As pointed out by André et al. (2010) and Men'shchikov et al. (2010), there is an intimate correspondence between the spatial distribution of dense cores and the filamentary network. Theoretical works have shown that filamentary molecular clouds can fragment into clumps as a result of gravitational instability (Nakamura et al. 1993; Tomisaka 1995; Van Loo et al. 2014), and some of these clumps have sufficient density to evolve, collapse, and form stars (Contreras et al. 2016). Henning et al. (2010) found that about 75% of the pre- and protostellar cores detected by *Herschel* PACS observations are located within the filamentary IRDC G011.11−0.12. Könyves et al. (2015) also found that about 78% of prestellar cores lie within a 0.1 pc width (Arzoumanian et al. 2011) of the filaments' footprints traced by the DisPerSE algorithm (Sousbie 2011) in the Aquila cloud. It is reasonable to believe that filamentary structures, as the most common shape of molecular clouds, may be the preferred birthplace of dense clumps and prestellar cores (André et al. 2010; Busquet et al. 2013; Lu et al. 2018).

Magnetic fields also play an important role in the formation of filamentary structures. Inoue & Fukui (2013) and Inoue et al. (2018) proposed a scenario that a filament is formed due to the convergence of an inhomogeneous cloud, which is caused by the bending of the ambient magnetic field, when sweeping by a magnetohydrodynamics (MHD) shock wave. This scenario is

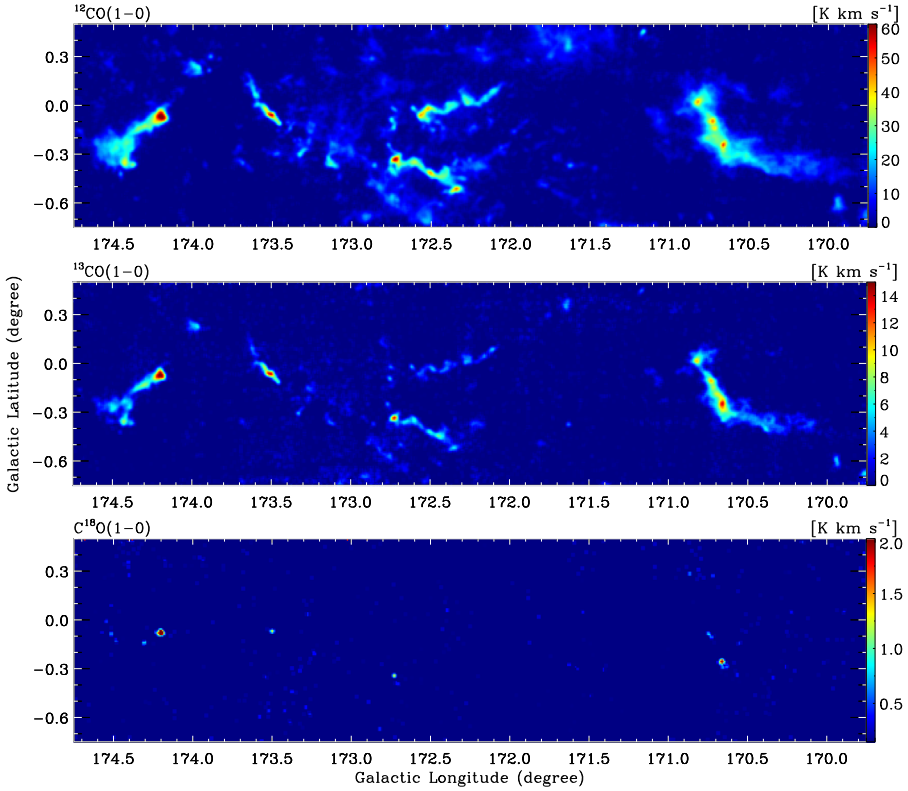

Figure 1. Top panel: integrated intensity map of the G172 region in the ^{12}CO emission with a velocity range from −24.5 to 7.5 km s^{-1}. Middle panel: integrated intensity map of the G172 region in the ^{13}CO emission with a velocity range from −24.5 to 7.5 km s^{-1}. Bottom panel: integrated intensity map of the G172 region in the C^{18}O emission with a velocity range from −24.5 to 7.5 km s^{-1}.

compatible with the CO observations toward the filamentary molecular cloud in Taurus (Arzoumanian et al. 2018). In addition, magnetic fields also help to shape and stabilize the filaments (Palmeirim et al. 2013; Kirk et al. 2015). Kusune et al. (2016) found that the magnetic field appears to be perpendicular to the inner "ridge filaments" in Vela C. The similar magnetic field running perpendicular to the filament is also found in the B211 region of Taurus (Palmeirim et al. 2013) and IRDC G14.225−0.506 (Busquet et al. 2013; Santos et al. 2016). Arzoumanian et al. (2019) pointed out that thermally supercritical filaments tend to be mostly perpendicular to the magnetic field lines and are the main sites of prestellar core formation (André et al. 2010; Könyves et al. 2015), while thermally subcritical filaments are well aligned with the local magnetic field lines and without any star-forming activity (Arzoumanian et al. 2013; Hacar et al. 2016).

Hence, it is of great importance to study various filamentary structures (e.g., small-scale and large-scale, low-mass and high-mass) within the Milky Way, characterizing their properties in detail and understanding the star-forming activity therein. We have conducted molecular line observations toward two Galactic regions centered at $l = 150°$, $b = 3.°5$ (referred to hereafter as the "G150 region") and $l = 172°$, $b = -0.°2$ (referred to hereafter as the "G172 region"), both of which have significant filamentary structures within. Our work is part of the Milky Way Imaging Scroll Painting (MWISP) project,[7] conducted by the Purple Mountain Observatory (PMO) using the PMO 13.7 m radio telescope to investigate the molecular gas along the northern Galactic plane with the ^{12}CO, ^{13}CO, and C^{18}O ($J = 1 - 0$) lines. Our work in the G150 region (see Xiong et al. 2017) showed that the molecular gas in this region consists of one main filament in the inner area with a higher column density and 11 subfilaments in the outer area with lower column densities, forming the so-called "ridge-nest" structure. About 75% of the CO dense clumps are associated with the filaments, and 56% of the virialized clumps are associated with the gravitationally bound filaments. For the G172 region, our observations reveal that most of the molecular clouds in this region present filamentary structures (see Figure 1). However, so far, there has been no detailed study of these filamentary molecular clouds, and the properties of the filaments and dense clumps within are still unknown.

In this paper, we present the MWISP CO ($J = 1 - 0$) observations toward the G172 region in the CO isotopologues. With the multiline observations (the angular resolution of the MWISP survey is ∼50″, and the velocity resolution is ∼0.16 km s^{-1}), we identify five different velocity components characterized by filamentary structures, study in detail their dynamical properties, and investigate the molecular clumps and young stellar objects (YSOs) associated with them. In Section 2, we describe the CO line observations and data reduction. We present our main results in Section 3 and discussions in Section 4. The conclusions are summarized in Section 5.

2. Observations and Data Reduction

2.1. CO Data

Our observations of the G172 region covered an area within $169.°75 \leqslant l \leqslant 174.°75$ and $-0.°75 \leqslant b \leqslant 0.°5$. The operation

[7] http://english.dlh.pmo.cas.cn/ic/in/ and http://www.radioast.nsdc.cn/mwisp.php.

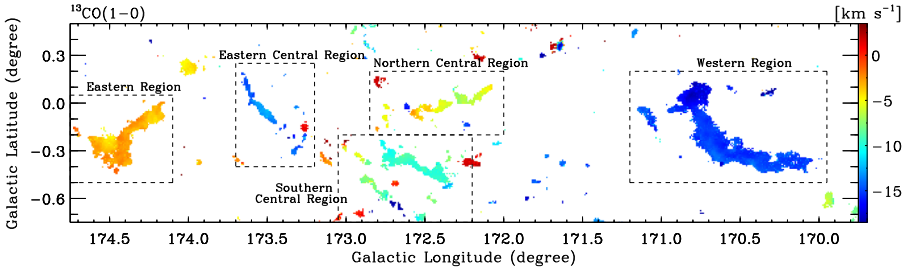

Figure 2. Velocity distribution map of molecular clouds in the G172 region traced by the ^{13}CO emission. The velocity range is from −18.5 to 3.5 km s^{-1}. The name of each region is marked beside it.

of observations was conducted by the 13.7 m millimeter-wavelength PMO telescope located in Delingha, China, from 2015 November to 2016 December. The ^{12}CO ($J = 1 - 0$), ^{13}CO ($J = 1 - 0$), and C^{18}O ($J = 1 - 0$) emission lines were observed simultaneously with the nine-beam Superconducting Spectroscopic Array Receiver (SSAR; Shan et al. 2012). The half-power beamwidth of the telescope was about 52″ at 115.2 GHz and 55″ at 110.2 GHz.

The telescope scanned the sky along both the longitude and latitude directions at a constant rate of 50″ s^{-1} using the on-the-fly (OTF) observation mode. During the observations, the typical system temperature was 270 K for the ^{12}CO line and 175 K for the ^{13}CO and C^{18}O lines. The antenna temperature (T_A^*) was calibrated to the main beam temperature (T_{MB}) by using $T_{MB} = T_A^*/\eta_{MB}$, with a main beam efficiency (η_{MB}) of 44% for the ^{12}CO line and 48% for the ^{13}CO and C^{18}O lines.

The bad channels and standing waves were removed when checking the spectra after we derived the original OTF data. Using the GILDAS software package (Guilloteau & Lucas 2000; Pety 2005; Gildas Team 2013), we regridded the data into 30″ × 30″ pixels (which is approximately half of the beam size based on the unified data reduction for the MWISP project) and converted them into the standard FITS files. We further used the IDL software to mosaic these FITS files together to generate the final data cube of the G172 region. As a result, the rms noise level is 0.49 K for ^{12}CO and 0.26 K for ^{13}CO and C^{18}O, and the velocity resolution is 0.16 km s^{-1} for ^{12}CO and 0.17 km s^{-1} for ^{13}CO and C^{18}O.

For the ^{12}CO and C^{18}O emission lines, we further applied Gaussian fitting to the spectra using the IDL software. The ^{13}CO ($J = 1 - 0$) line has two hyperfine lines, which are ^{13}CO ($J = 1 - 0$, $F = 1/2 - 1/2$) ($\nu = 110.20132180$ GHz) and ^{13}CO ($J = 1 - 0$, $F = 3/2 - 1/2$) ($\nu = 110.20137040$ GHz). We used the hyperfine line model from the Python package to fit the hyperfine structures of ^{13}CO. The fitting results are presented in Section 3.

2.2. IR Data

In this work, we used the complementary IR data from the Two Micron All Sky Survey (2MASS; Skrutskie et al. 2006) with near-IR J (1.25 μm), H (1.65 μm), and K_s (2.16 μm) bands; the *Wide-field Infrared Survey Explorer* (*WISE*; Wright et al. 2010) with four IR bands, $W1$ (3.4 μm), $W2$ (4.6 μm), $W3$ (12 μm), and $W4$ (22 μm); and the *Spitzer* (Werner et al. 2004) Galactic Legacy Infrared Mid-Plane Survey Extraordinaire (GLIMPSE; Benjamin et al. 2003; Churchwell et al. 2009; Whitney et al. 2011) with two IRAC bands, [3.6 μm] and [4.5 μm]. The IR data were retrieved from the NASA/IPAC Infrared Science Archive (IRSA).[8]

3. Results

3.1. Overview and Identification of Filamentary Structures

As shown in Figure 1, our CO observations of the G172 region reveal several filamentary molecular clouds in this region. The CO emission within this region covers the velocity range from −24.5 to 7.5 km s^{-1}. Due to isotopic abundance ratios, the transitions of rare isotopologues (e.g., ^{12}CO ($J = 1 - 0$), ^{13}CO ($J = 1 - 0$), and C^{18}O ($J = 1 - 0$)) would have smaller optical depths (see Section 3.2) at the same densities. Moreover, the $J = 1 - 0$ transitions of ^{12}CO, ^{13}CO, and C^{18}O have slightly different excitation conditions (e.g., Mangum & Shirley 2015). The different excitation conditions, along with the different optical depths, would further result in the $J = 1 - 0$ transitions of various CO isotopologues being able to trace different gas densities. The ^{12}CO emission traces the outlines of filamentary structures with a density of $\sim 10^2$ cm^{-3}, while the ^{13}CO emission reveals the skeletons of filamentary structures with a typical density of $\sim 10^3$ cm^{-3}. The C^{18}O emission marks the densest parts of the ^{13}CO emission with a higher density of $\sim 10^4$ cm^{-3}. The two filamentary clouds in the outer area (the one in the east and the one in the west) have stronger integrated intensities than those in the inner area. The emission of the C^{18}O line is also mainly located in the outer area.

Based on the ^{13}CO data, we derived the velocity distribution map shown in Figure 2. The filamentary molecular clouds in this region cover a wide range of velocity components, ranging from −15 km s^{-1} (the one in the west[9]) to −2 km s^{-1} (the one in the east). To illustrate the velocity components more directly, we derived a longitude–velocity map of this region, shown in the middle panel of Figure 3. It is evident that these filamentary molecular clouds have quite different velocity components. According to the difference in velocity and spatial distributions (see the middle panel of Figure 1), we divide the filamentary molecular clouds of the G172 region into five main subregions—i.e., the eastern region, eastern central region, northern central region, southern central region, and western region—in order to study their properties separately and in detail. The velocity components of these five subregions are presented in the top and bottom panels of Figure 3.

As defined by André et al. (2014), a "filament" is any elongated ISM structure with an aspect ratio larger than ∼5–10 that is significantly overdense with respect to its surroundings.

[8] http://irsa.ipac.caltech.edu/frontpage/

[9] The direction words in this work refer to the Galactic coordinate.

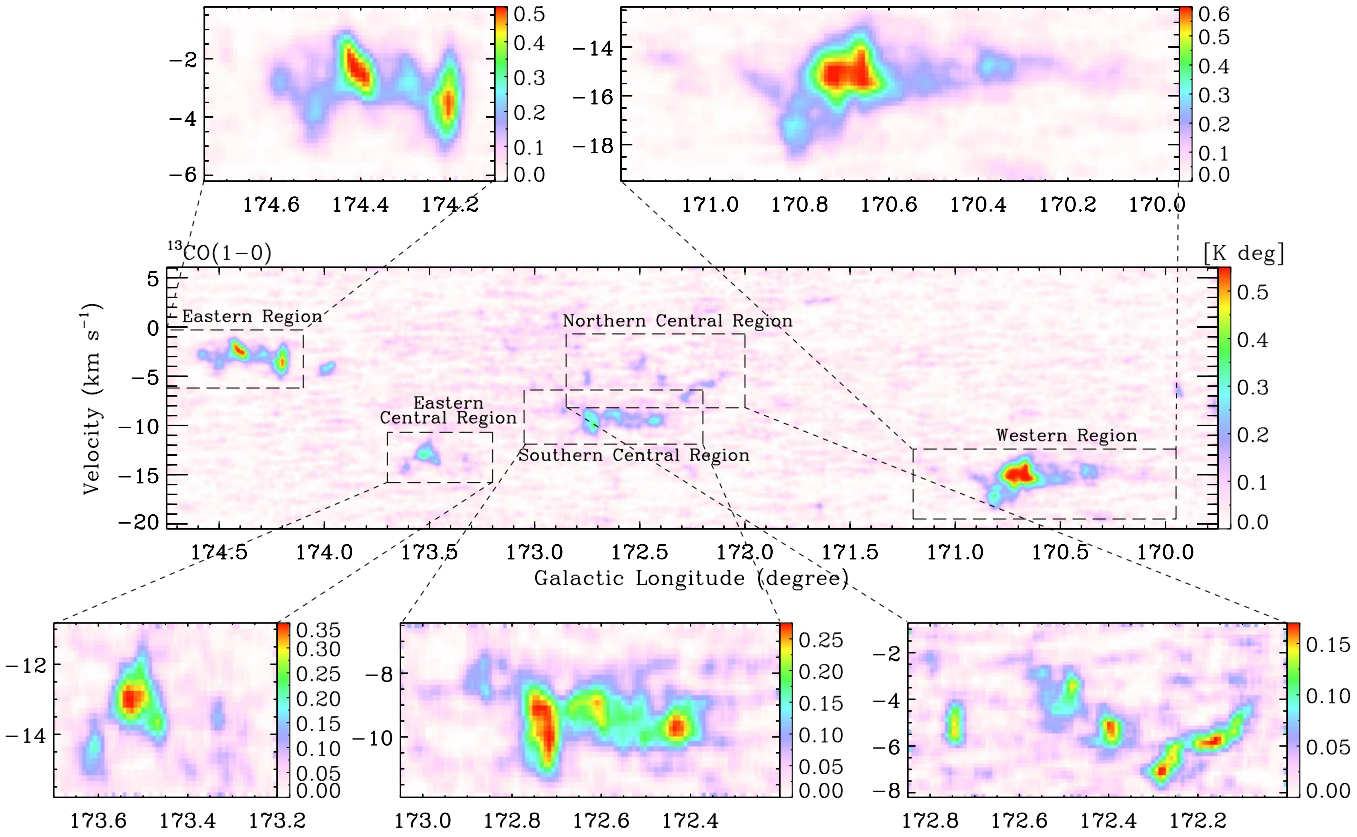

Figure 3. Top panels: longitude–velocity maps of the eastern and western regions with the integrated latitude ranges of −0.°5 to 0.°05 and −0.°5 to 0.°2, respectively. Middle panel: longitude–velocity map of the whole G172 region with the integrated latitude range of −0.°75 to 5°. Bottom panels: longitude–velocity maps of the eastern central, southern central, and northern central regions with the integrated latitude ranges of −0.°4 to 0.°25, −0.°75 to −0.°2, and −0.°2 to 0.°2, respectively.

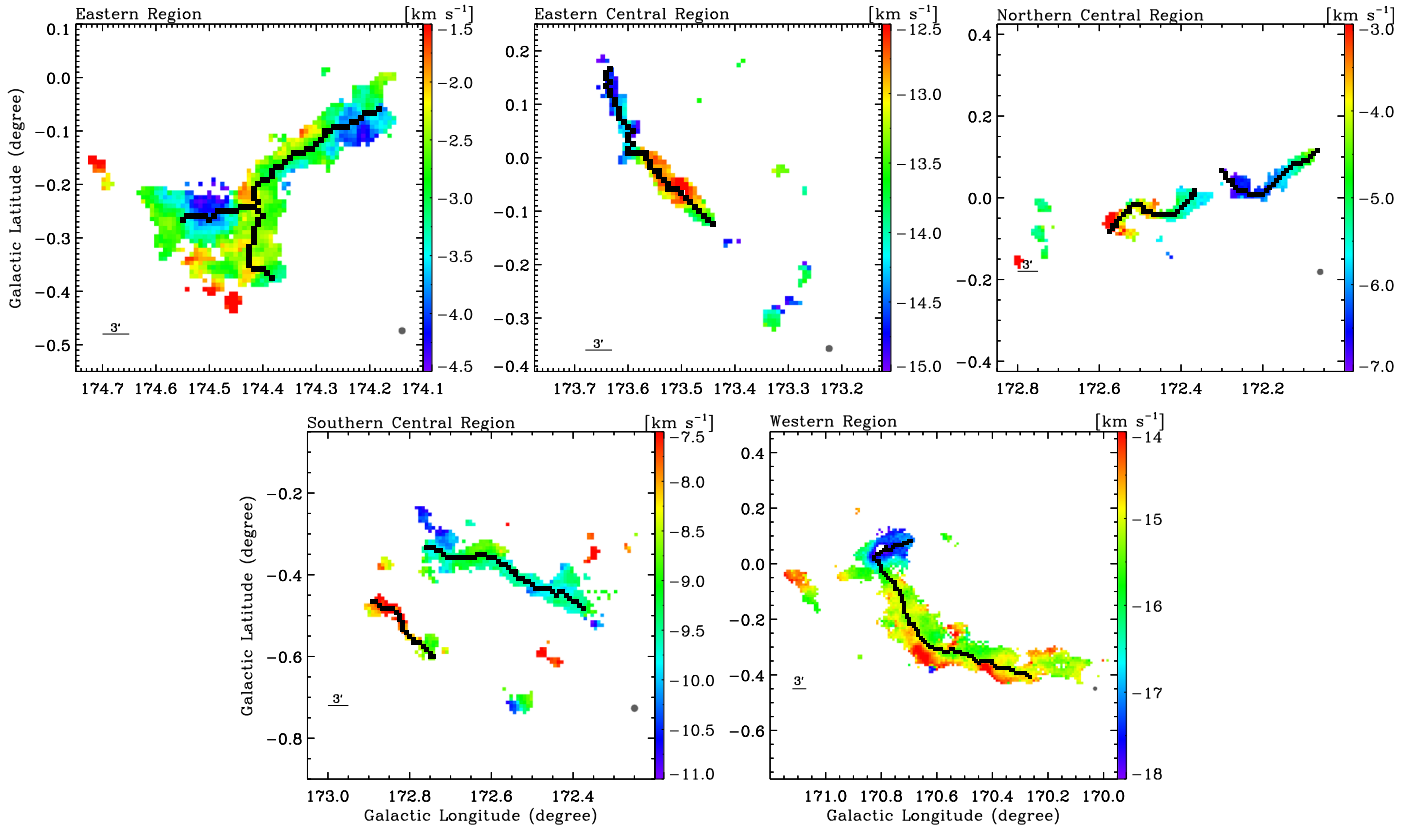

Figure 4. Filamentary structures identified in each region. The solid black lines indicate the positions of the filaments identified by FilFinder. The backgrounds are the ^{13}CO velocity distribution maps of each region.

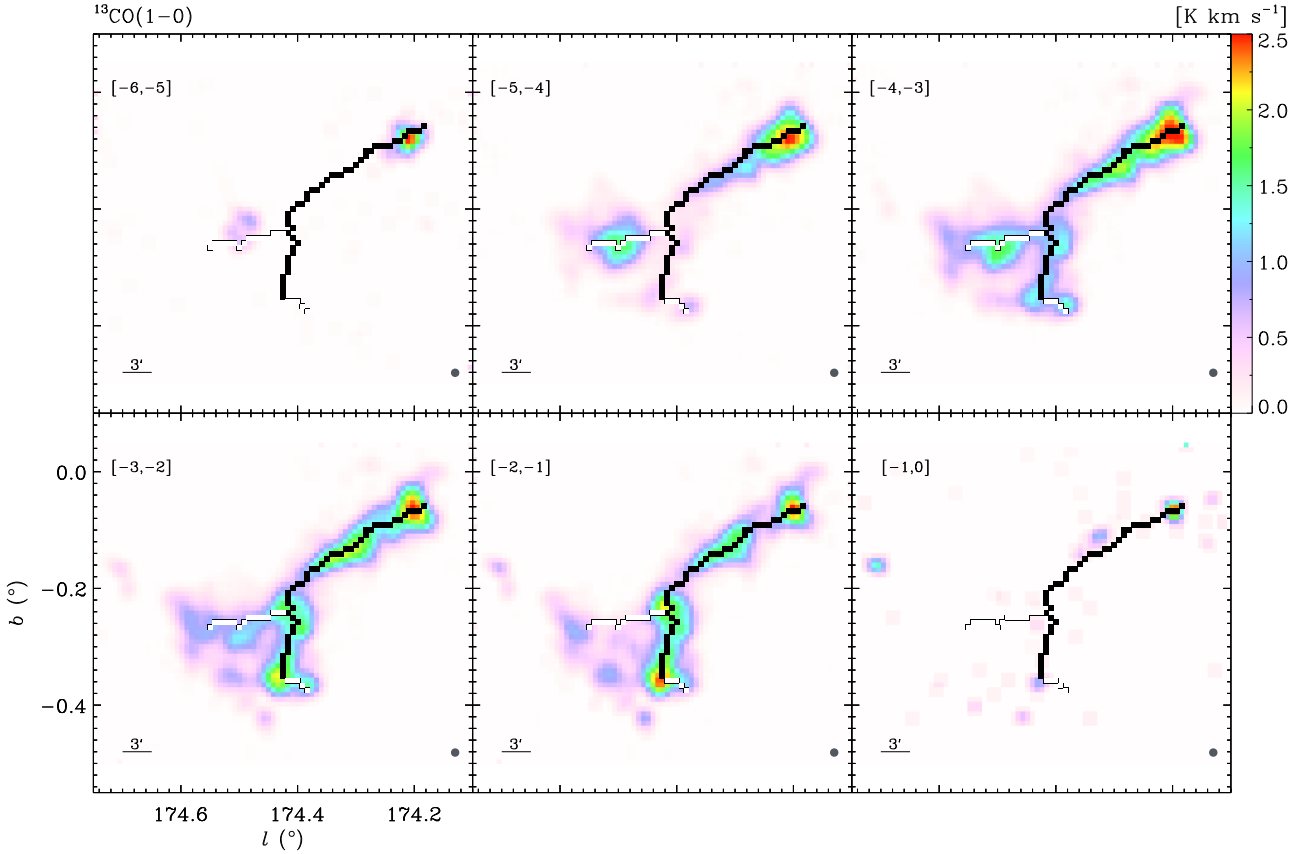

Figure 5. Velocity channel maps of molecular clouds in the eastern region traced by the ^{13}CO emission. The solid black lines indicate the qualified filament after the velocity-coherence check. The solid white lines indicate the rejected structures that are not velocity-coherent. The velocity range (in units of km s^{-1}) marked on each map is the integration range of each channel.

They also pointed out that filaments are generally linear over their length and appear to be colinear in the direction of the longer extents of their host clouds. Hacar et al. (2017, 2018) further confined the velocity coherence of the filaments by adopting the local measured line width as the velocity threshold to check the points along the filaments. According to these definitions, we adopt the "FilFinder" algorithm (Koch & Rosolowsky 2015) to identify filamentary structures within each subregion. FilFinder is a new approach to identifying filaments within molecular clouds based on the application of mathematical morphology. As illustrated in Koch & Rosolowsky (2015), FilFinder relies on an adaptive threshold, which will create a mask based on local changes in the brightness of the intensity image. The medial axis transform will then reduce the signal mask to a skeleton. This skeleton will further be pruned down to form a filamentary network.

In the practical identification process, we define the mask area as the emission area where the signal-to-noise ratio (S/N) is greater than 3 within the input intensity image. We set the "adapt_thresh" as 0.8 pc (two times the beam size of our observations for a distance of ∼1.7 kpc; see Section 3.7), which is the width of the element within the mask, and set the "size_thresh" as 3.92 pc^2 (assuming an aspect ratio of 5 according to the definition of André et al. 2014), which is the minimum area a region of the mask must have. When inputting a defined mask, the algorithm will use these two parameters to verify whether this mask has qualified width and area or not. After deriving the skeletons, the algorithm will further prune the small branches attached to the skeletons with lengths smaller than the "branch_thresh," which is set as 10 pixels (five times the beam size of our observations for a pixel size of 30″ × 30″). Based on these settings, FilFinder is applied to the ^{13}CO intensity image of each subregion. The final result is shown in Figure 4.

We realize that FilFinder can only identify filamentary structures in the 2D image at this point, which means it cannot take into account the velocity information. Therefore, the identified skeletons (including the attached branches) may not be velocity-coherent structures. We further inspect the ^{13}CO data cube of each subregion and ^{13}CO *PV* map of each structure to make sure these skeletons and branches are velocity-coherent. Specifically, we first calculate the thermal line width of the ^{13}CO emission area with an S/N greater than 3 within each subregion using the formula

$$\Delta v_{\rm thermal} = \sigma_{\rm thermal}\sqrt{8\ln 2} = \sqrt{\frac{k_{\rm B}T_{\rm kin}}{\mu_{\rm obs}m_{\rm H}}}\sqrt{8\ln 2}. \quad (1)$$

Here $k_{\rm B}$ is the Boltzmann constant, $\mu_{\rm obs}$ is the molecular weight of the observed molecule (29 for ^{13}CO), and $m_{\rm H}$ is the mass of the hydrogen atom. In this work, the kinetic temperature $T_{\rm kin}$ is assumed to be the excitation temperature under the local thermodynamic equilibrium (LTE) condition (see Section 3.2). We then check each two adjacent independent pixels with S/N > 3 along each skeleton or branch within the data cube of each subregion. If the velocity difference of every 2 pixels is smaller than the corresponding thermal line width, we will regard this skeleton or branch as a velocity-coherent structure.

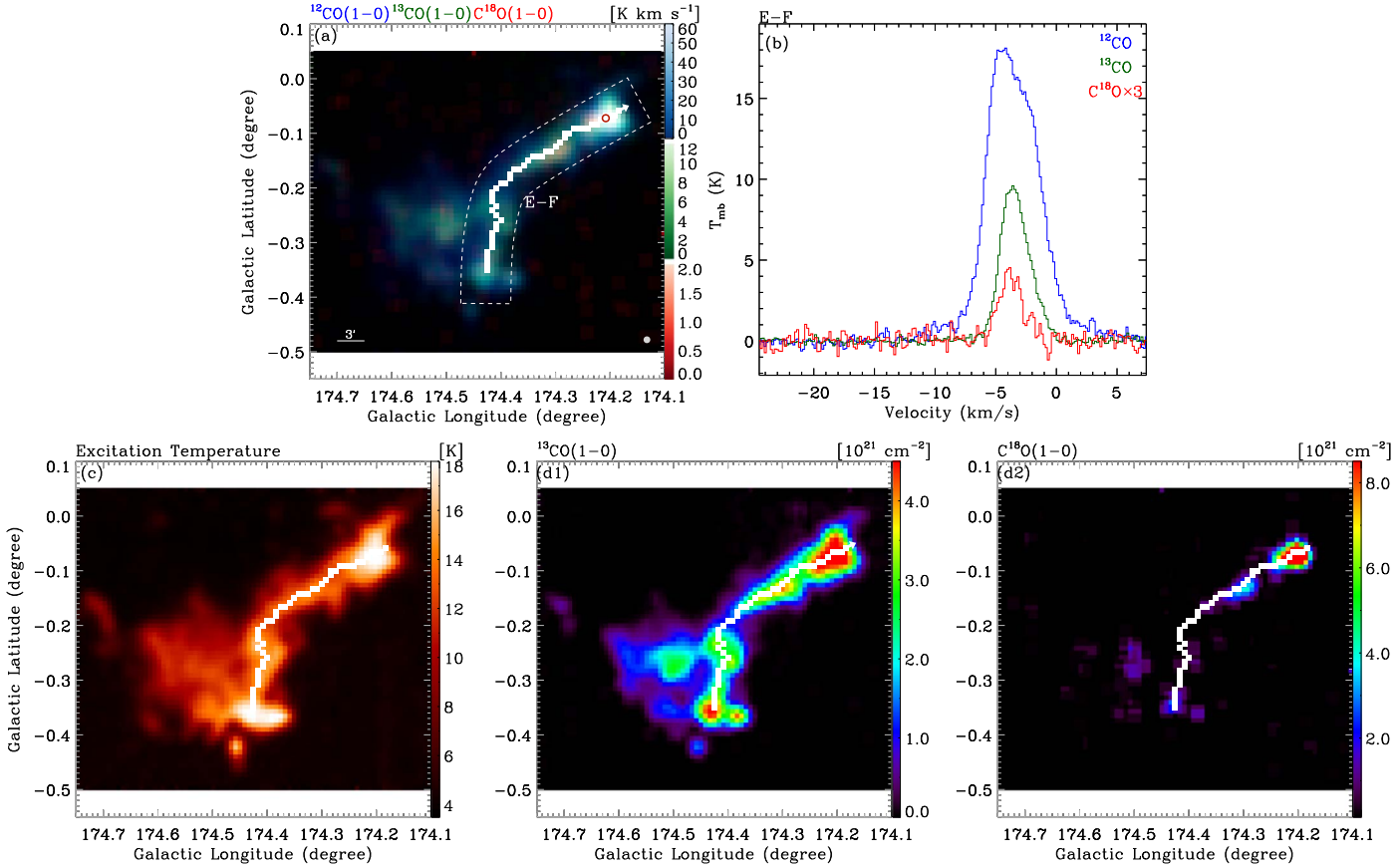

Figure 6. Properties of E-F in the eastern region. (a) Three-color image of the integrated intensity maps of ^{12}CO (blue, integrated from −8.0 to 1.0 km s^{-1}), ^{13}CO (green, integrated from −6.2 to −0.3 km s^{-1}), and C^{18}O (red, integrated from −5.5 to −1.5 km s^{-1}). The solid white line shows the position of E-F, and the arrow indicates the direction of the *PV* plot of E-F shown in Figures 15 and 16. The dashed box indicates the approximate emission area around the filament where the S/N is greater than 3. The red circle indicates the peak position of the ^{12}CO emission along the filament. (b) The CO spectra toward the red circle. (c) Excitation temperature map. (d1) and (d2) The H_2 column density maps traced by ^{13}CO and C^{18}O. The arrow in (d1) indicates the direction used to determine the left and right sides of E-F corresponding to the $R < 0$ and $R > 0$ parts of the radial density profile in Figure 17.

Otherwise, we will reject the branch or part of the skeleton that is not velocity-coherent.

In the following subsections, we show the results of the velocity-coherence check and present the properties of filamentary structures in each subregion separately.

3.2. Filamentary Structures in the Eastern Region

Figure 5 shows the ^{13}CO velocity channel maps of the filamentary molecular cloud in the eastern region. The solid lines (both black and white lines) are the skeleton and branch identified by FilFinder. During the velocity-coherence check, we find that the southern end ($l \sim 174.^{\circ}4$, $b \sim -0.^{\circ}38$) of the skeleton is not velocity-coherent relative to the rest of the skeleton. So we reject this small part and mark it white. FilFinder has also identified a branch across a small molecular cloud ($l \sim 174.^{\circ}50$, $b \sim -0.^{\circ}26$) to the east of the skeleton. This small cloud has a different velocity component (ranging from −5 to −3 km s^{-1}) from the emission area of the skeleton. Thus, we choose to reject this branch and mark it white. The black line is the qualified filamentary structure after the velocity-coherence check. We name this filamentary structure the "eastern region filament" (hereafter "E-F").

In panel (a) of Figure 6, we present the three-color image of the integrated intensity maps of the filamentary structure E-F. The dashed box indicates the approximate emission area of E-F where the S/N is greater than 3. The C^{18}O emission appears at the brightest parts (e.g., $l \sim 174.^{\circ}21$, $b \sim -0.^{\circ}08$; $l \sim 174.^{\circ}30$, $b \sim -0.^{\circ}13$; and $l \sim 174.^{\circ}43$, $b \sim -0.^{\circ}34$), where the ^{12}CO (blue), ^{13}CO (green), and C^{18}O (red) emissions overlap with each other. Panel (b) is the spectra of the CO isotopologues toward the red circle, which indicates the peak position of the ^{12}CO emission.

We further calculate the excitation temperature and column density of this filament based on the assumption that the molecular cloud is in the LTE condition, the ^{12}CO emission is optically thick, and the ^{13}CO emission is optically thin. To verify the CO optical depth, we adopt the correlation

$$\frac{T_{\rm mb}(^{12}{\rm CO})}{T_{\rm mb}(^{13}{\rm CO})} = \frac{1 - e^{-\tau_{12}}}{1 - e^{-\tau_{13}}} = \frac{1 - e^{-\tau_{13}X}}{1 - e^{-\tau_{13}}}, \quad (2)$$

assuming the same excitation temperature for ^{12}CO and ^{13}CO. Here $T_{\rm mb}$ is the main beam brightness temperature of the CO emission, τ is the optical depth of CO, and X is the abundance ratio [^{12}CO]/[^{13}CO] (e.g., Scoville et al. 1986; Garden et al. 1991), which is estimated to be 73.24 for the eastern region with a distance of 1.68 kpc (see Section 3.7) based on the work of Milam et al. (2005). The result is that the optical depth of ^{12}CO (τ_{12}) ranges from 3.22 to 46.87 within the velocity range of filament E-F, and the optical depth of ^{13}CO (τ_{13}) ranges from 0.04 to 0.64. We also verify the CO optical depth for the rest of the subregions and find that τ_{12} is much larger than 1

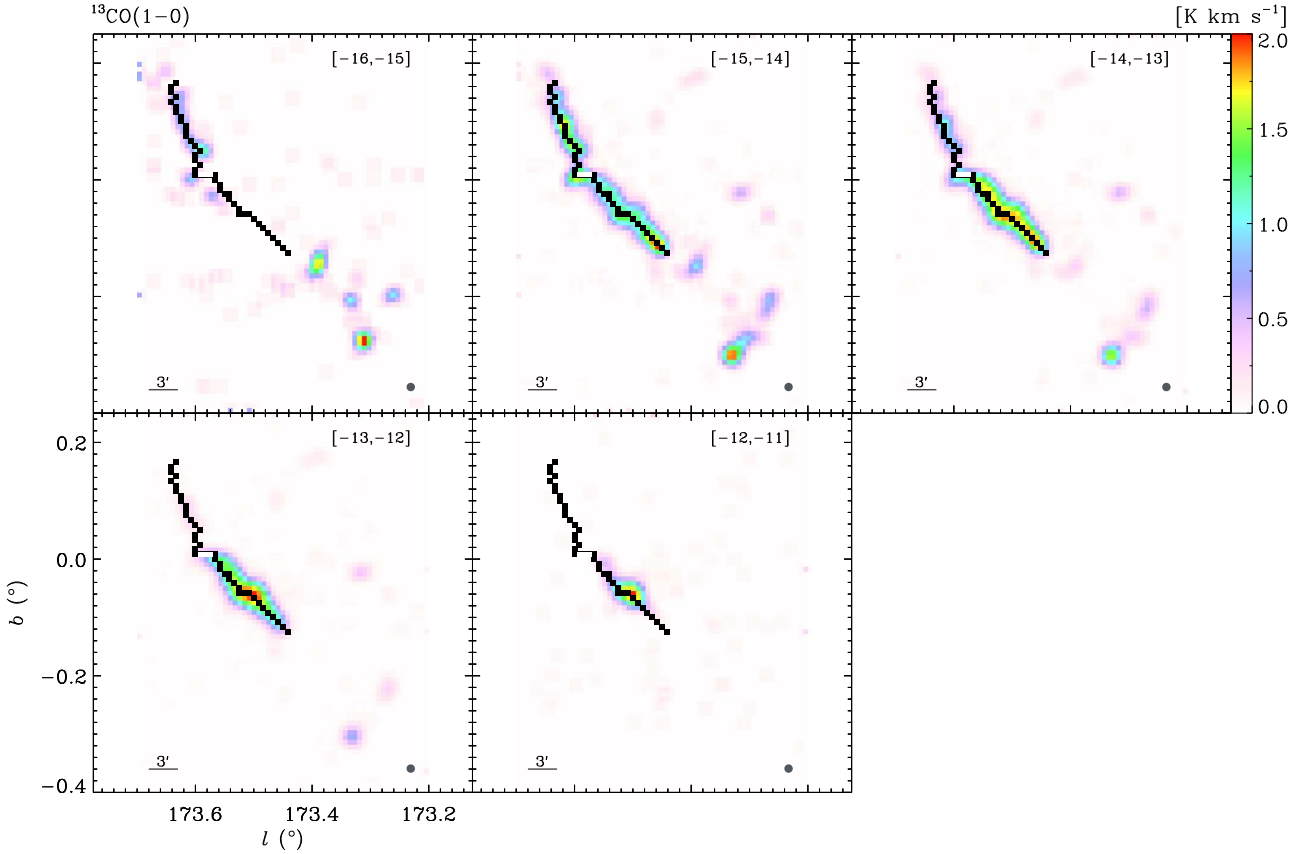

Figure 7. Velocity channel maps of molecular clouds in the eastern central region traced by the ^{13}CO emission. The solid black lines indicate the qualified filaments after the velocity-coherence check. The solid white lines indicate the rejected structure that is not velocity-coherent. The velocity range (in units of km s^{-1}) marked on each map is the integration range of each channel.

and τ_{13} is smaller than 1 within the velocity components of the filamentary molecular clouds.

After the verification of the CO optical depth, we can calculate the excitation temperature ($T_{\rm ex}$) from the brightness temperature of the ^{12}CO emission using

$$T_{\rm ex} = T_0 / \ln\left(1 + \left(\frac{T_{\rm mb}(^{12}{\rm CO})}{(1 - e^{-\tau_{12}})T_0} + \frac{1}{e^{T_0/T_{\rm bg}} - 1}\right)^{-1}\right). \quad (3)$$

Here $T_0 = h\nu/k_{\rm B}$ is the intrinsic temperature of ^{12}CO, where h is the Planck constant and $k_{\rm B}$ is the Boltzmann constant, and $T_{\rm bg}$ is the background temperature with a value of 2.7 K. The opacity depth τ_{12} is much larger than 1, which means $1 - e^{-\tau_{12}} \approx 1$. Under all of these conditions, we derive the excitation temperature map and present it in panel (c) of Figure 6. The temperature is much higher at the two ends of E-F (∼21 K in the northern end and ∼23 K in the southern end) compared to the middle part. The mean temperature of the whole filament is about 8.72 ± 0.97 K.

In this work, we choose to regard the excitation temperature ($T_{\rm ex}$) derived from the ^{12}CO emission as the kinetic temperature ($T_{\rm kin}$) of the molecular gas. The larger optical depth of ^{12}CO ($\tau_{12} \gg 1$) increase the interactions between the photons and the matter, which tends to lead to the LTE condition. We further check the dust temperature ($T_{\rm dust}$) map derived from *Herschel* for the eastern region (Marsh et al. 2017). Marsh et al. (2017) processed the Hi-GAL data with the point process mapping (PPMAP) method (Marsh et al. 2015), which is a Bayesian procedure that uses images of dust continuum emission at multiple wavelengths and the associated point-spread functions (PSFs) to produce resolution-enhanced image cubes of column density and dust temperature. The dust temperature has a similar distribution as the excitation temperature, increasing toward the denser parts of the filamentary structure. The mean ratio of $T_{\rm dust}$ to $T_{\rm ex}$ within the filamentary area is about 1.0239. Based on the LTE condition and the similar distribution as the dust temperature, it is reasonable to use $T_{\rm ex}$ as $T_{\rm kin}$ in this work, since the *Herschel* observations (Marsh et al. 2017) do not cover the entire area of the G172 region.

We also derive the H_2 column density maps of E-F traced by the ^{13}CO and C^{18}O emission, which are shown in the bottom panels of Figure 6. Since the ^{13}CO and C^{18}O emission is optically thin in the velocity component of E-F, we can first calculate the column density using the excitation temperature and their integrated intensity, then multiply the column density by the abundance of $N_{\rm H_2}/N_{^{13}{\rm CO}}$ (7×10^5; Frerking et al. 1982) and $N_{\rm H_2}/N_{{\rm C}^{18}{\rm O}}$ (7×10^6; Castets & Langer 1995) to derive the H_2 column density (see the details in Xiong et al. 2017). The mean values of H_2 column density are $4.77 \pm 0.49 \times 10^{21}$ cm^{-2} (within the ^{13}CO emission area with S/N > 3) and $8.37 \pm 0.11 \times 10^{21}$ cm^{-2} (within the C^{18}O emission area with S/N > 3).

We further compare the column density derived from the ^{13}CO data with that derived from the far-IR (FIR) data obtained with *Herschel* for the eastern and eastern central regions (Marsh et al. 2017). For the eastern region, the mean ratio of

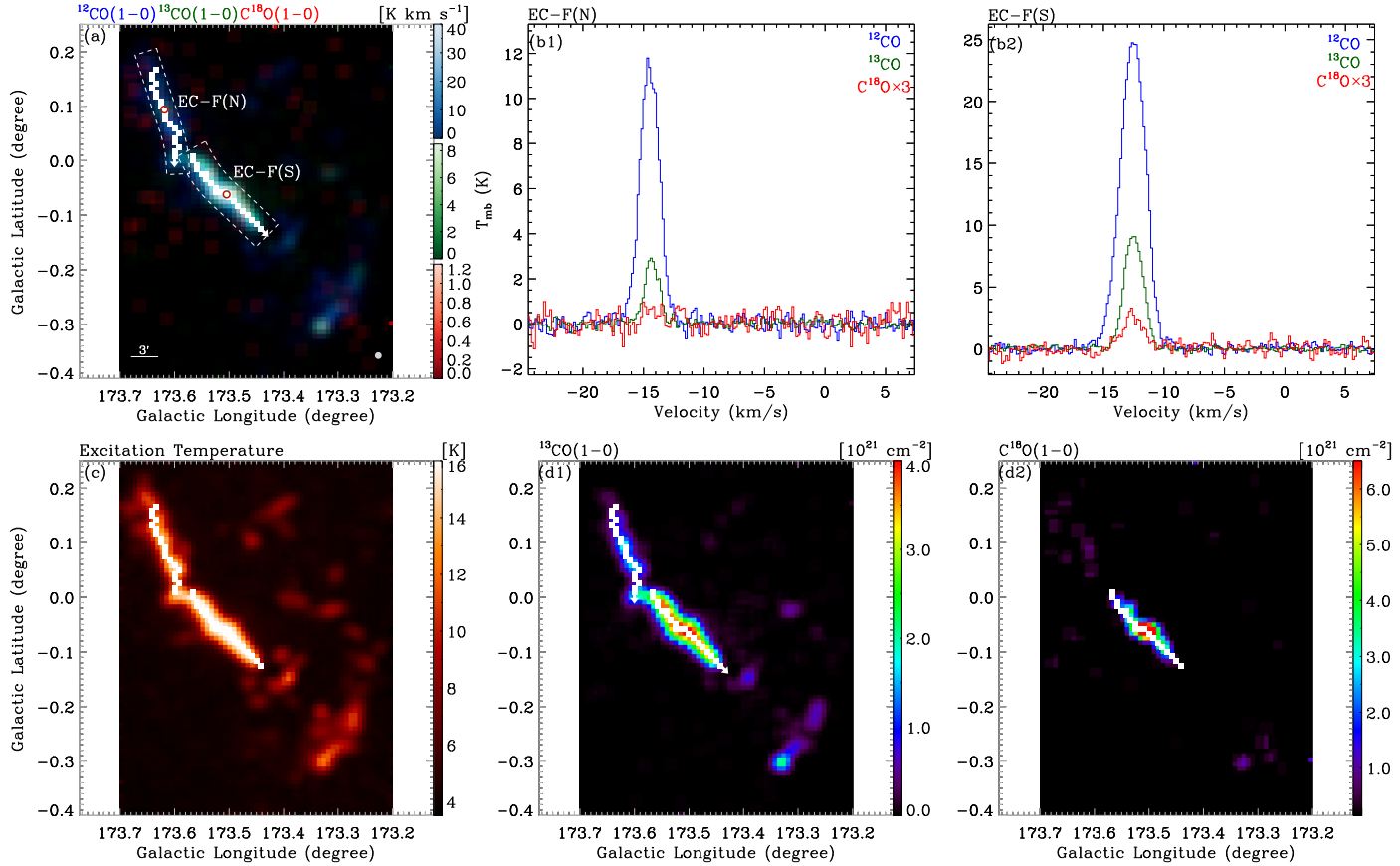

Figure 8. Properties of EC-F(N) and EC-F(S) in the eastern central region. (a) Three-color image of the integrated intensity maps of ^{12}CO (blue; integrated from −17.0 to −10.0 km s^{-1}), ^{13}CO (green; integrated from −15.8 to −10.7 km s^{-1}), and C^{18}O (red; integrated from −13.9 to −11.3 km s^{-1}). The solid white lines show the positions of EC-F(N) and EC-F(S), and the arrows indicate the directions of the *PV* plots of EC-F(N) and EC-F(S) shown in Figures 15 and 16. The dashed boxes indicate the approximate emission area around each filament where the S/N is greater than 3. The red circles indicate the peak positions of the ^{12}CO emission along each filament. (b1) and (b2) The CO spectra toward the red circles. (c) Excitation temperature map. (d1) and (d2) The H_2 column density maps traced by ^{13}CO and C^{18}O. The arrows in (d1) indicate the directions used to determine the left and right sides of EC-F(N) and EC-F(S) corresponding to the $R < 0$ and $R > 0$ parts of the radial density profiles in Figure 17.

N_{H_2} (^{13}CO) to N_{H_2} (FIR) is about 0.45, and for the eastern central region, the mean ratio is about 0.38. The H_2 column density from the FIR emission is typically about two to three times higher than the H_2 column density measured by the ^{13}CO emission. However, Sanhueza et al. (2017) pointed out that the mass estimation of molecular gas from dust emission could have an uncertainty higher than a factor of 2, resulting from the large uncertainties of the dust opacity and the dust-to-gas mass ratio. Indeed, as mentioned by Marsh et al. (2017), the reference dust opacity at 300 μm could have the largest uncertainty up to about 50%. The dust-to-gas mass ratio of 100 (adapted by Marsh et al. 2017) could also have an uncertainty of 23% (Sanhueza et al. 2017), assuming the uniform distribution of the range of the Galactic dust-to-gas mass ratio between 70 and 150 (e.g., Devereux & Young 1990; Vuong et al. 2003). The final uncertainties of the H_2 column density derived by Marsh et al. (2017) have typical values as high as a factor of 1.8. Given these similar factors of uncertainty values, the agreement between the column density estimations from the CO and FIR data is reasonable. Therefore, in this work, it is reasonable to use the CO emission to calculate the H_2 column density.

With the direction of the arrowed line and the width of the dashed box shown in panel (a) of Figure 6, we extract the ^{13}CO and C^{18}O position–velocity (*PV*) plots of E-F (see Figures 15 and 16, respectively). The ^{13}CO *PV* plot displays continuous structure without significant curvature along the position axis. The velocity gradient of E-F is weak, which is from −2.5 km s^{-1} (southern part) to −3.5 km s^{-1} (northwestern part; referring to the direction of E-F in Figure 6). Tracing the densest parts of E-F, the C^{18}O *PV* plot displays discontinuous features. A strong emission area is located in the northwest, while several weaker emission spots are in the south.

3.3. Filamentary Structures in the Eastern Central Region

In the eastern central region, FilFinder has identified only one skeleton (see both the black and white solid lines in Figure 7). However, during the velocity-coherence check, we find that the northern part of the skeleton and the southern part are not velocity-coherent relative to each other. Actually, the velocity component (ranging from −15.5 to −13.8 km s^{-1}) of the northern part is different from that of the southern part (ranging from −13.8 to −11.2 km s^{-1}). So we decide to split this long skeleton into two skeletons by rejecting a small middle part (marked as white in Figure 7) of the long skeleton. The black lines in Figure 7 show the qualified filamentary structures. We name the northern filament the "eastern central region filament (north)" (hereafter "EC-F(N)") and the southern filament the "eastern central region filament (south)" (hereafter

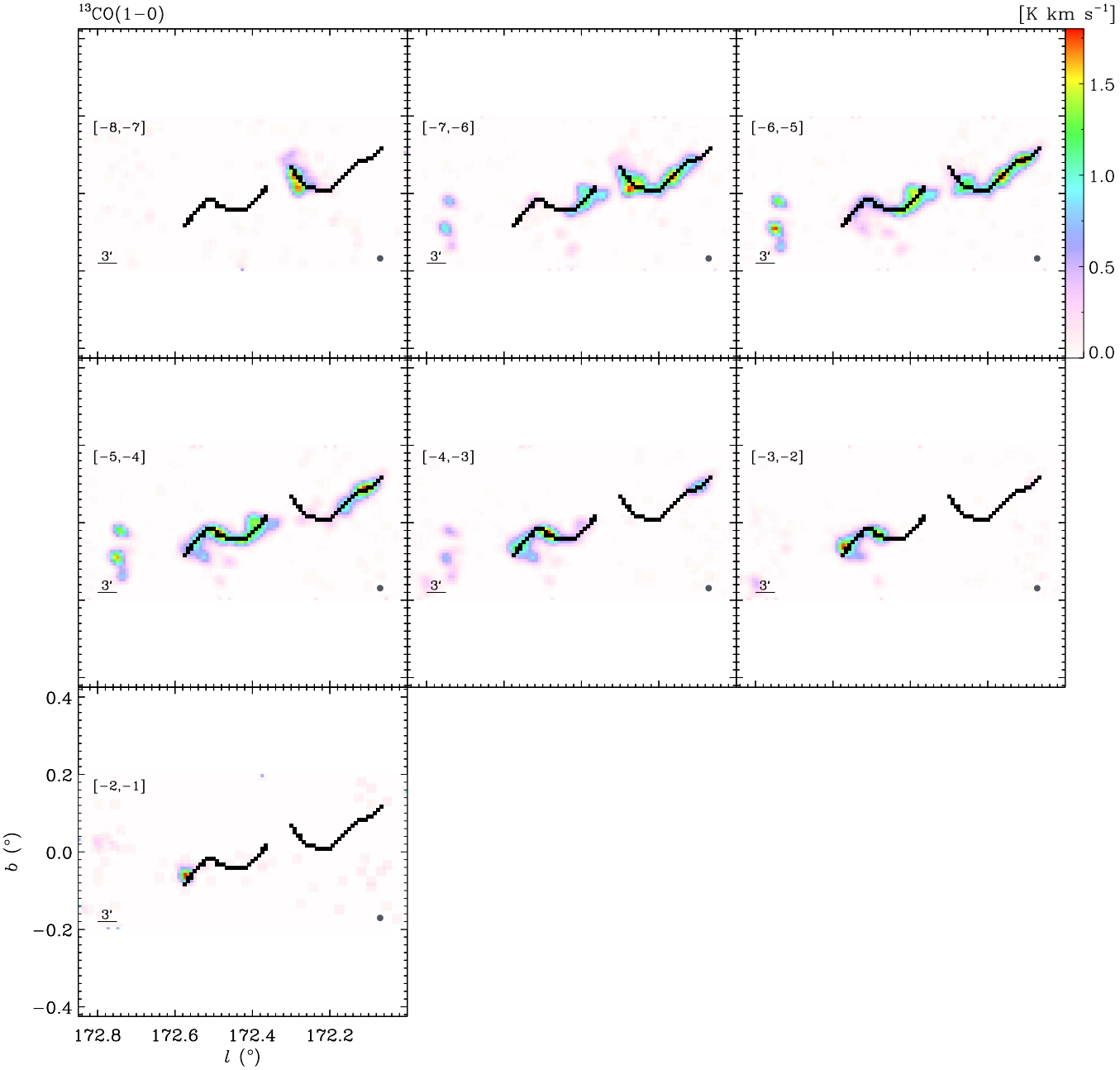

Figure 9. Velocity channel maps of molecular clouds in the northern central region traced by the ^{13}CO emission. The solid black lines indicate the qualified filaments after the velocity-coherence check. The velocity range (in units of km s^{-1}) marked on each map is the integration range of each channel.

"EC-F(S)"). Both of these two filaments extend from the northeast to the southwest.

The integrated intensity maps of the CO isotopologues are shown in panel (a) of Figure 8. The dashed boxes indicate the approximate emission areas of EC-F(S) and EC-F(N) where the S/N is greater than 3. We detect stronger ^{13}CO and C^{18}O emission in EC-F(S), while in EC-F(N), the ^{13}CO emission is much weaker, and no C^{18}O emission is detected (S/N < 3).

The CO spectra in panels (b1) and (b2) show the differences in emission intensities and velocity components between these two filaments as we discussed above. The excitation temperature and column density of EC-F(S) are higher than those of EC-F(N) (see panels (c), (d1), and (d2)). The mean $T_{\rm ex}$ values are 8.02 ± 0.82 K (EC-F(N)) and 9.60 ± 1.23 K (EC-F(S)), and the mean $N_{\rm H_2}$ values are $1.26 \pm 0.16 \times 10^{21}$ cm^{-2} (^{13}CO) for EC-F(N) and $6.53 \pm 0.69 \times 10^{21}$ cm^{-2} (^{13}CO) and $7.94 \pm 0.12 \times 10^{21}$ cm^{-2} (C^{18}O) for EC-F(S).

The ^{13}CO *PV* plots are presented in Figure 15. Both EC-F(N) and EC-F(S) have very weak velocity gradients. Here EC-F(N) has several strong emission spots along the position axis, while EC-F(S) has one strong emission spot located in the central part. The C^{18}O *PV* plot of EC-F(S) is shown in Figure 16; the C^{18}O emission is only detected in the central part.

3.4. Filamentary Structures in the Northern Central Region

Shown in Figure 9, FilFinder has identified two skeletons in the northern central region. During the velocity-coherence check, both of these skeletons showed velocity-coherent structures. So we regard them as qualified filaments. The filament in the east ("northern central region filament (east),"

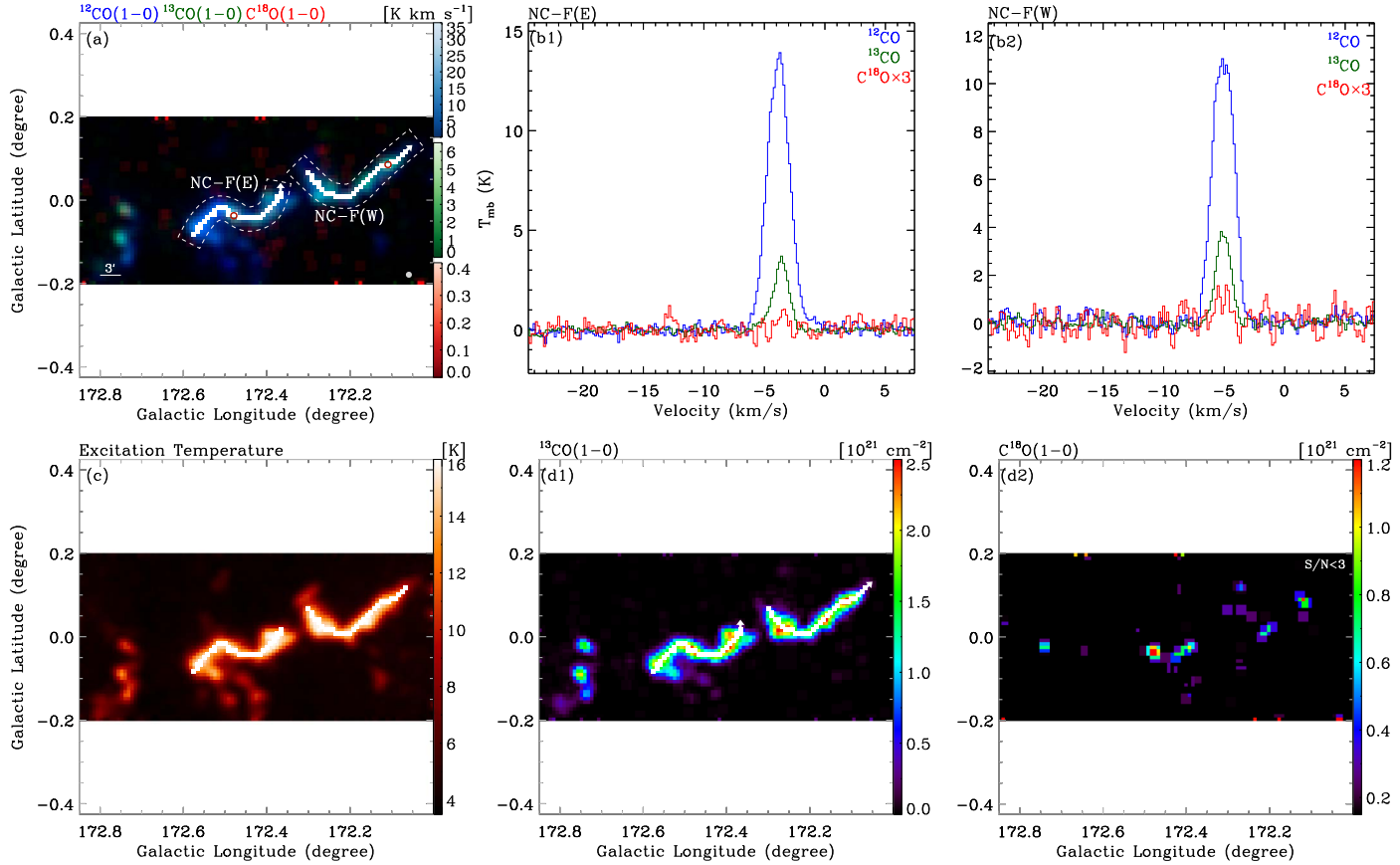

Figure 10. Properties of NC-F(E) and NC-F(W) in the northern central region. (a) Three-color image of the integrated intensity maps of ^{12}CO (blue; integrated from −9.0 to 0.5 km s^{-1}), ^{13}CO (green; integrated from −8.2 to −0.7 km s^{-1}), and C^{18}O (red; integrated from −5.9 to −3.1 km s^{-1}). The solid white lines show the positions of NC-F(E) and NC-F(W), and the arrows indicate the directions of the *PV* plots of NC-F(E) and NC-F(W) shown in Figure 15. The dashed boxes indicate the approximate emission area around each filament where the S/N is greater than 3. The red circles indicate the peak positions of the ^{12}CO emission along each filament. (b1) and (b2) The CO spectra toward the red circles. (c) Excitation temperature map. (d1) and (d2) The H_2 column density maps traced by ^{13}CO and C^{18}O. The arrows in (d1) indicate the directions used to determine the left and right sides of NC-F(E) and NC-F(W) corresponding to the $R < 0$ and $R > 0$ parts of the radial density profiles in Figure 17.

hereafter "NC-F(E)") has a velocity component ranging from −7 to −2 km s^{-1}, while the filament in the west ("northern central region filament (west)," hereafter "NC-F(W)") is distributed from −8 to −4 km s^{-1}. Both of these filaments exhibit curvy shapes extending in the east–west direction.

Figure 10 shows the basic properties of NC-F(E) and NC-F(W). The ^{13}CO emission of NC-F(W) is slightly stronger than that of NC-F(E), and no C^{18}O emission is detected (S/N < 3) in both filaments (see panels (a), (b1), and (b2)). The excitation temperatures are similar between these two filaments: 8.93 ± 0.96 K (NC-F(E)) and 9.41 ± 1.01 K (NC-F(W)). The mean H_2 column density is 1.53 ± 0.19 × 10^{21} cm^{-2} (^{13}CO) for NC-F(E), while for NC-F(W), the value is 1.72 ± 0.23 × 10^{21} cm^{-2} (^{13}CO).

Shown in Figure 15, the ^{13}CO *PV* plot of NC-F(E) displays a structure consisting of three different parts. The southeastern and middle parts appear to be split from each other but have the same velocity. The northwestern part is connected to the middle part but has a different velocity. The velocity gradient of NC-F(E) is from −3.0 km s^{-1} (southeastern part; referring to the direction of NC-F(E) in Figure 10) to −5.5 km s^{-1} (northwestern part), while the velocity gradient of NC-F(W) is from −7.0 km s^{-1} (northeastern part; referring to the direction of NC-F(W) in Figure 10) to −4.5 km s^{-1} (northwestern part).

3.5. Filamentary Structures in the Southern Central Region

Two individual skeletons are identified in this region (see Figure 11). These two skeletons are velocity-coherent and thus qualified filaments after the velocity-coherence check. We name the northern one "SC-F(N)," for which the velocity ranges from −11 to −8.5 km s^{-1}. The southern one is named "SC-F(S)" and is revealed from −9.5 to −7 km s^{-1}. These two filaments are parallel with each other, and SC-F(N) extends much farther than SC-F(S).

Shown in panels (a), (b1), and (b2) of Figure 12, SC-F(N) has much stronger ^{12}CO and ^{13}CO emission than SC-F(S), and the C^{18}O emission is only detected in SC-F(N). The mean excitation temperature is about 8.99 ± 0.99 K in SC-F(N) and lower in SC-F(S) (6.16 ± 0.49 K). The bottom panels present the H_2 column density maps of these two filaments. For SC-F(N), the mean column densities are 2.94 ± 0.32 × 10^{21} cm^{-2} (^{13}CO) and 5.05 ± 0.07 × 10^{21} cm^{-2} (C^{18}O). For SC-F(S), the mean value is 0.70 ± 0.09 × 10^{21} cm^{-2} (^{13}CO).

Both SC-F(N) and SC-F(S) have slightly twisted velocity structures (see Figure 15). The velocity component of SC-F(N) changes from −9.5 km s^{-1} (western part) to −9.0 km s^{-1} (middle part) and then to −10.0 km s^{-1} (eastern part). A similar velocity gradient is found in SC-F(S), which goes from −9.0 km s^{-1} (western part) to −7.5 km s^{-1} (middle part) and changes to −8.0 km s^{-1} (eastern part). The C^{18}O *PV* plot of

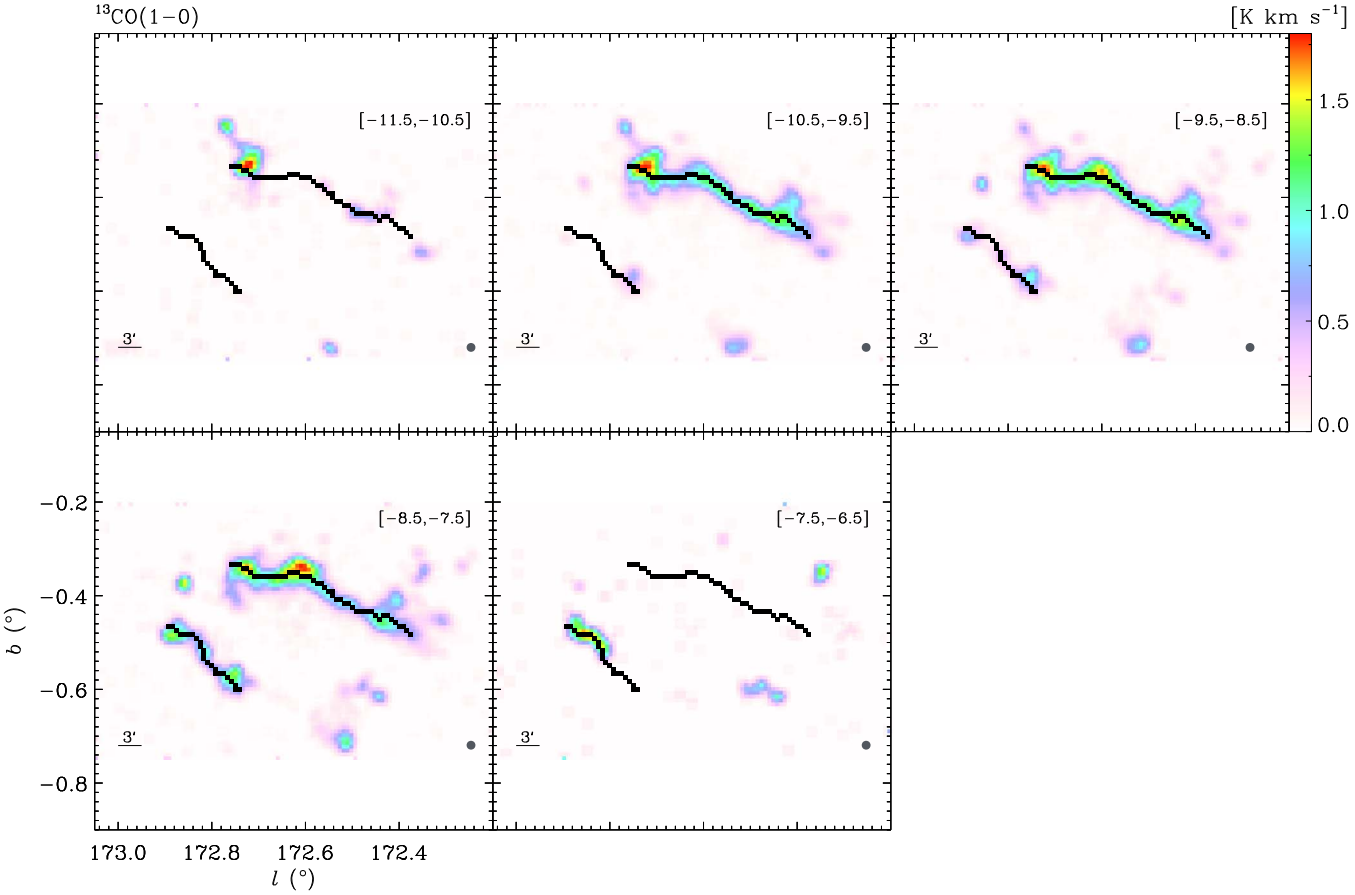

Figure 11. Velocity channel maps of molecular clouds in the southern central region traced by the ^{13}CO emission. The solid black lines indicate the qualified filaments after the velocity-coherence check. The velocity range (in units of km s^{-1}) marked on each map is the integration range of each channel.

SC-F(N) is shown in the last panel of Figure 16. The emission area is mainly located in the eastern part.

3.6. Filamentary Structures in the Western Region

The velocity channel maps of the western region are presented in Figure 13. Only one long skeleton is identified by FilFinder. During the velocity-coherence check, we find that the northeastern end ($l \sim 170.^{\circ}82$, $b \sim 0.^{\circ}02$) of the long skeleton has a different velocity component (ranging from -19.5 to -17.5 km s^{-1}) from the main body of the skeleton (ranging from -17 to -13.5 km s^{-1}) and choose to reject this part (see the white line in Figure 13). The qualified filament is marked by a black line in Figure 13. We name this filament the "western region filament" ("W-F"). The whole filament extends from northeast to southwest.

Shown in panel (a) of Figure 14 is the three-color image of W-F. The C^{18}O emission is mainly distributed in the middle part of W-F. The northern part of W-F has a higher excitation temperature than the southern part, according to the T_{ex} map shown in panel (c). The mean T_{ex} of the whole filament is about 8.13 ± 0.74 K. We further derive the H_2 column density maps of W-F traced by CO isotopologues (see panels (d1) and (d2)). The mean values are $2.12 \pm 0.25 \times 10^{21}$ cm^{-2} (^{13}CO) and $3.52 \pm 0.05 \times 10^{21}$ cm^{-2} (C^{18}O).

For the most part, from southwest to northeast of W-F, there is no evident velocity gradient revealed (see Figure 15). The velocity gradient occurs at the northernmost part of W-F, which is from -15.0 to -17.5 km s^{-1}. The C^{18}O *PV* plot is presented in Figure 16. There is a large area of C^{18}O emission located in the middle part, while several weaker emission spots are in the southwest and north.

3.7. Properties of Filaments

3.7.1. Distances to Filaments

In this work, we adopt the probability density function (PDF) generated by the Bayesian approach (Reid et al. 2016) to estimate the distance to each filament. For a source given with its Galactic longitude and latitude coordinate and local standard-of-rest velocity (l, b, v), the Bayesian distance estimation program[10] of Reid et al. (2016) will construct a PDF for each type of distance information (including spiral arm assignment, kinematic distance, Galactic latitude, and location within a giant molecular cloud with a measured parallax) and then multiply them together to arrive at a combined distance PDF. The distance to this source is determined from the component fitted to the combined PDF that has the greatest integrated probability.

In our case, we first choose three points located at the two ends and in the middle of each filament and then use their coordinates (l, b, v) to calculate the distances to these points. As a result, we derive three distance values in the eastern and western regions and six distance values in the eastern central, northern central, and southern central regions. Shown in Table 1, the distances to the points within the same region

[10] http://bessel.vlbi-astrometry.org/bayesian

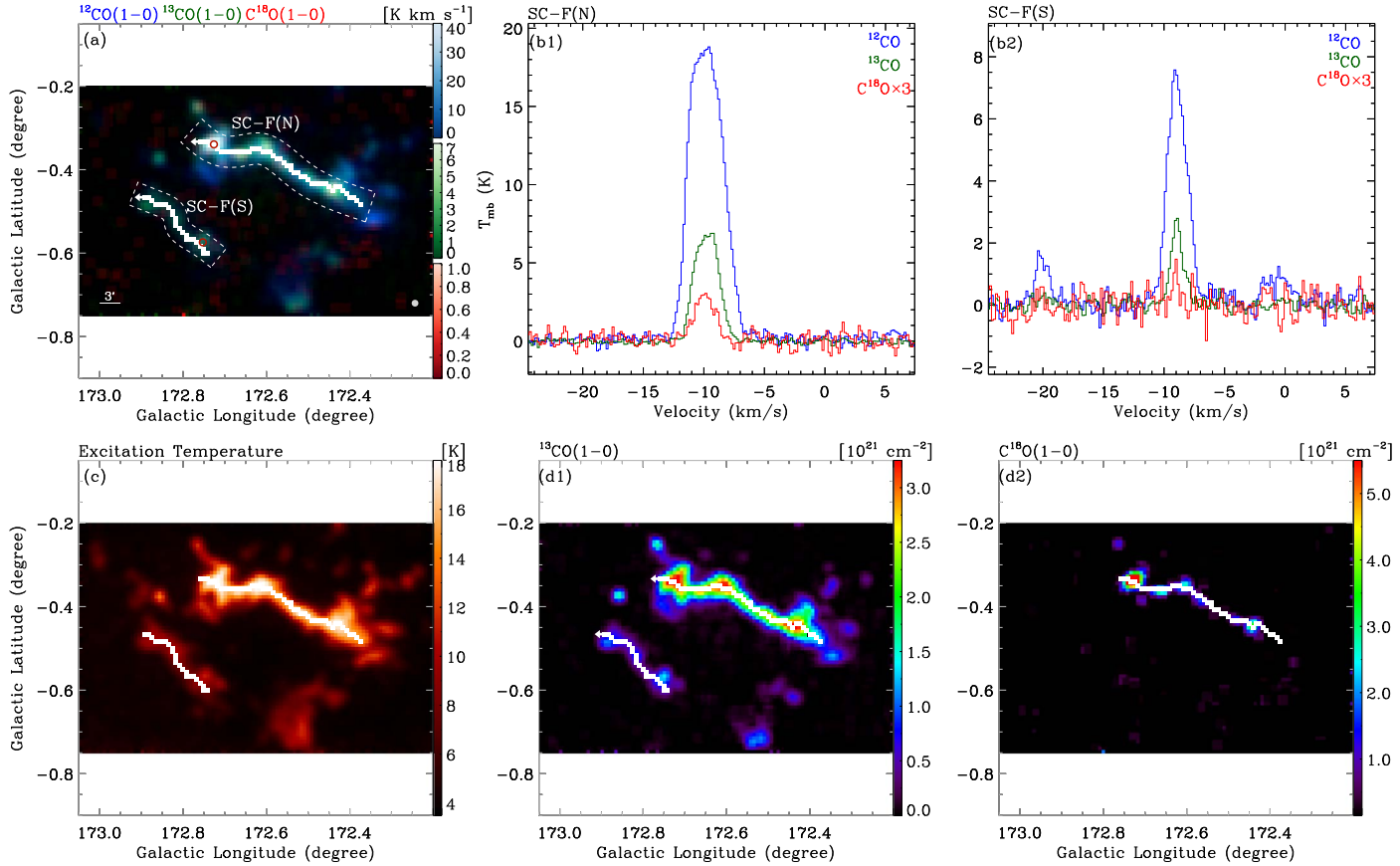

Figure 12. Properties of SC-F(N) and SC-F(S) in the southern central region. (a) Three-color image of the integrated intensity maps of ^{12}CO (blue; integrated from −13.0 to −6.0 km s^{-1}), ^{13}CO (green; integrated from −11.9 to −6.4 km s^{-1}), and C^{18}O (red; integrated from −11.1 to −8.8 km s^{-1}). The solid white lines show the positions of SC-F(N) and SC-F(S), and the arrows indicate the directions of the *PV* plots of SC-F(N) and SC-F(S) shown in Figures 15 and 16. The dashed boxes indicate the approximate emission area around each filament where the S/N is greater than 3. The red circles indicate the peak positions of the ^{12}CO emission along each filament. (b1) and (b2) The CO spectra toward the red circles. (c) Excitation temperature map. (d1) and (d2) The H_2 column density maps traced by ^{13}CO and C^{18}O. The arrows in (d1) indicate the directions used to determine the left and right sides of SC-F(N) and SC-F(S) corresponding to the $R < 0$ and $R > 0$ parts of the radial density profiles in Figure 17.

are basically the same. So we regard the average of the distances to the points in each region as the distance to filamentary structures in each region, which are 1.68 kpc for the eastern region, 1.72 kpc for the eastern central region, 1.70 kpc for the northern central region, 1.73 kpc for the southern central region, and 1.90 kpc for the western region.

3.7.2. LTE Mass of Filaments

With the distance to each filament and H_2 column density derived in the previous sections, we are able to calculate the LTE mass of the filaments by

$$M = \mu_{H_2} m_H \int N_{H_2} dS, \quad (4)$$

where μ_{H_2} is the mean molecular weight per hydrogen molecule with a value of 2.83 (Kauffmann et al. 2008) and S is the area of CO emission. Here we use the H_2 column density traced by ^{13}CO as N_{H_2}, since the ^{12}CO emission is too diffuse and not all of the filaments are detected with the C^{18}O emission. We also measure the length of each filament and derive the LTE line masses M_{LTE}, which are listed in Table 2.

3.7.3. Radial Profiles of Filaments

We further calculate the radial density profiles of filaments based on the H_2 column density (shown in panel (d2) of Figures 6, 8, 10, 12, and 14). Using the same method as Palmeirim et al. (2013) and Xiong et al. (2017), we first determine the tangential direction of each pixel along the position of each filament, shown as the solid white line in each (d2) panel. For each pixel, we then derive one column density profile perpendicular to the tangential direction. We average the profiles of all pixels along each filament and finally derive the mean radial density profile. The results are presented in Figure 17. Most profiles have Gaussian-like shapes in the inner parts, and the outer parts of the profiles reflect the distributions of the surrounding molecular gas. We note that EC-F(N) has two Gaussian components; the one at ∼−1.5 pc actually reflects the molecular gas belonging to EC-F(S) that is located at the same Galactic latitude of the southern end of EC-F(N) (see Figure 8). The inner profile of SC-F(S) is much weaker than the outer profile ($R > 3$ pc), which reflects the molecular gas from the "right" filament SC-F(N) (see Figure 12).

As pointed out by the works of the *Herschel* Gould Belt survey (e.g., Arzoumanian et al. 2011; Palmeirim et al. 2013; Cox et al. 2016), filamentary structures tend to have a narrow distribution in width with a median value of 0.10 ± 0.03 pc. However, some recent works (e.g., Hacar et al. 2018;

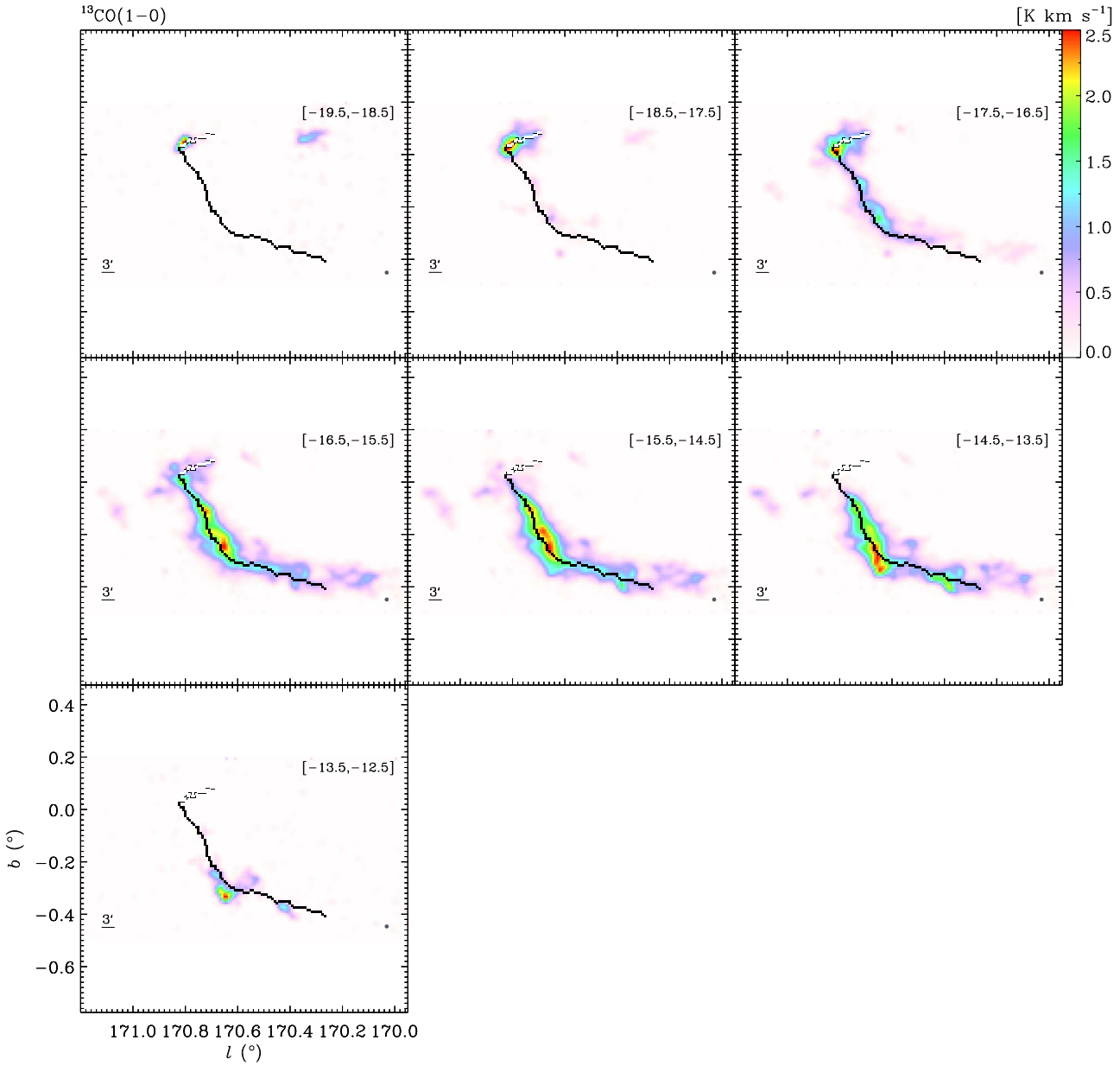

Figure 13. Velocity channel maps of molecular clouds in the western region traced by the ^{13}CO emission. The solid black lines indicate the qualified filament after the velocity-coherence check. The solid white lines indicate the rejected structure that is not velocity-coherent. The velocity range (in units of km s^{-1}) marked on each map is the integration range of each channel.

Ossenkopf-Okada & Stepanov 2019) show that the width of the filament may not be universal; it could be smaller or larger than 0.1 pc. In this work, we also calculate the FWHM width of each filament by applying Gaussian fits to the inner parts of the profiles (shown as the dashed red curves in Figure 17). The results are listed in Table 2. The mean width from these eight filaments is 1.13 ± 0.01 pc, which is much larger than 0.1 pc but similar to our previous work (0.79 pc; Xiong et al. 2017). We note that the resolution of our observations (50″, corresponding to ∼0.4 pc at a distance of ∼1.7 kpc) may not be sufficient to resolve the inner width of the filaments. Further high-resolution observations are needed to have a better understanding of the filament width in this region.

We also apply the Plummer fits (e.g., Arzoumanian et al. 2011; Palmeirim et al. 2013) to the radial density profiles; however, the Plummer-like function does not fit the profiles well, and the power index p turns out to be much larger than 2 (the value frequently seen in the *Herschel* Gould Belt survey). We note that the Plummer-like function tends to fit the profile in a broader range than the Gaussian function, while the outer parts of the profiles could be easily affected by the line emission from the surrounding molecular gas.

3.7.4. Other Properties of Filaments

In addition, we calculate the ^{13}CO line width of each filament. Following the method mentioned in Section 2, we first derive the line width of each pixel in the area around each filament where the integrated intensity of the ^{13}CO emission is greater than three times the rms noise. Then, we use the integrated intensity of these pixels as the weight to calculate the averaged line width of each area and thus the line width of each

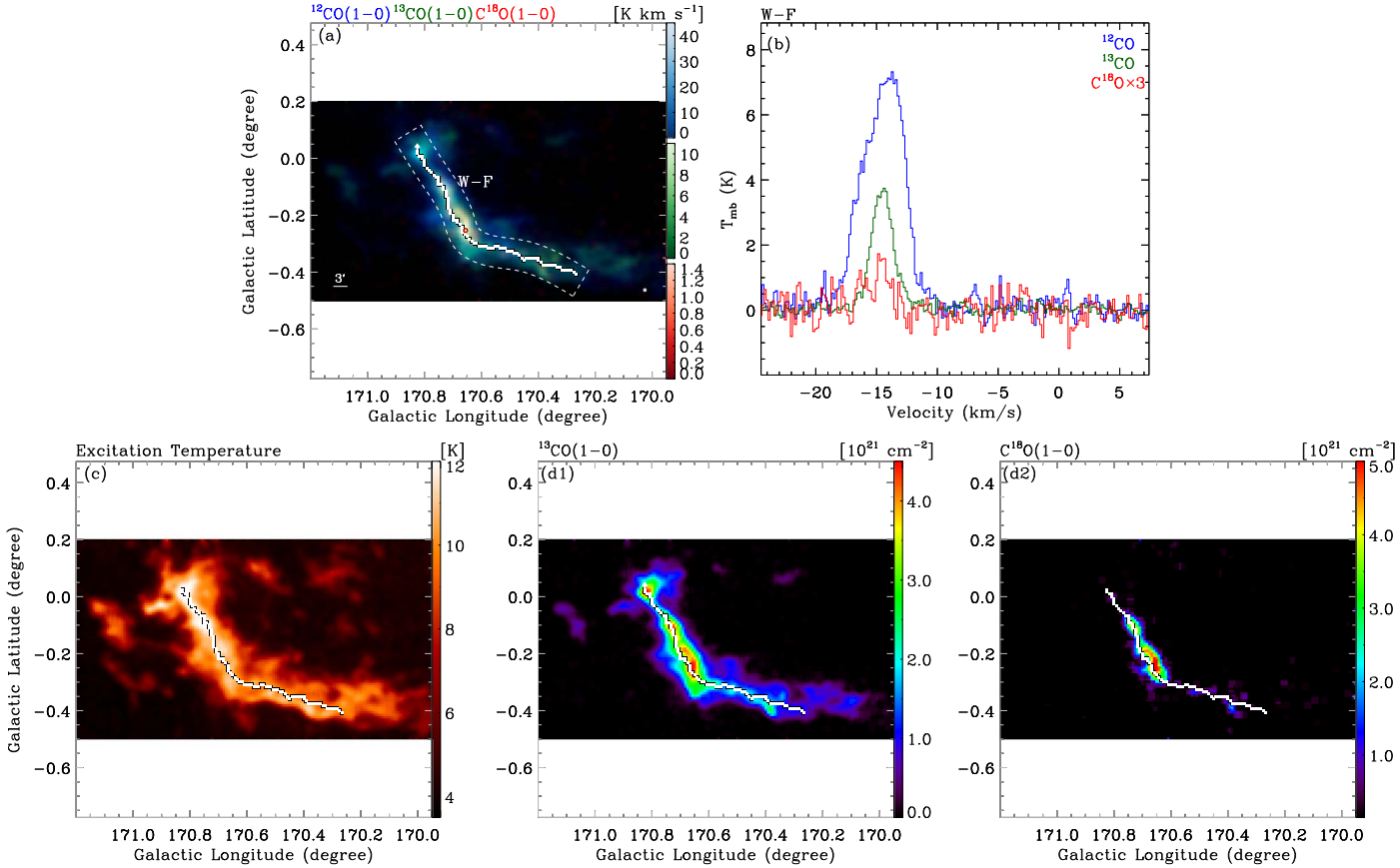

Figure 14. Properties of W-F in the western region. (a) Three-color image of integrated intensity maps of ^{12}CO (blue; integrated from −20.0 to −11.0 km s^{-1}), ^{13}CO (green; integrated from −19.5 to −12.4 km s^{-1}), and C^{18}O (red; integrated from −16.8 to −14.1 km s^{-1}). The solid white line shows the position of W-F, and the arrow indicates the direction of the *PV* plot of W-F shown in Figures 15 and 16. The dashed box indicates the approximate emission area around the filament where the S/N is greater than 3. The red circle indicates the peak position of the ^{12}CO emission along the filament. (b) The CO spectra toward the red circle. (c) Excitation temperature map. (d1) and (d2) The H_2 column density maps traced by ^{13}CO and C^{18}O. The arrow in (d1) indicates the direction used to determine the left and right sides of W-F corresponding to the $R < 0$ and $R > 0$ parts of the radial density profile in Figure 17.

filament. The results, along with the mean T_{ex} and N_{H_2} derived in previous sections, are listed in Table 2.

4. Discussion

4.1. Gravitational Stability of Filaments

According to the framework of Chandrasekhar & Fermi (1953) and the following studies (Ostriker 1964; Nagasawa 1987; Fiege & Pudritz 2000; Jackson et al. 2010; Fischera & Martin 2012), an isothermal gas cylinder would go through "sausage instability" and fragment along the radial direction once its mass per unit length (thus, line mass) exceeds a critical value of

$$M_{\rm crit} = 2\sigma^2/G, \tag{5}$$

where σ is the velocity dispersion representing the internal pressure (Wang et al. 2014), and G is the gravitational constant, which is given as $1/232$ km^2 s^{-2} $M_\odot^{-1}$ pc (Solomon et al. 1987). Therefore, the gravitational stability of a filament is determined by this critical mass. If the line mass of the filament is greater than the critical value, the filament is gravitationally unstable and will fragment into clumps along its length that may lead to star formation (e.g., Goldsmith et al. 2008; Bontemps et al. 2010; Xiong et al. 2017). On the contrary, with the line mass lower than the critical value, the filament is gravitationally unbound or in an expanding state and is even expected to disperse during the turbulent crossing time (Arzoumanian et al. 2013), unless confined by the external pressure (Fischera & Martin 2012).

The key parameter in the formula of critical mass is σ. When the internal support of the filament is mainly from thermal pressure, σ is substituted by the isothermal sound speed c_s, and the critical mass becomes $M_{\rm thermal} = 2c_s^2/G$ (Ostriker 1964). The isothermal sound speed can be derived from

$$c_s = \sqrt{\frac{k_B T_{\rm kin}}{\mu_p m_H}}, \tag{6}$$

where μ_p is the mean molecular weight per free particle with a value of 2.33 (Kauffmann et al. 2008). In this work, $T_{\rm kin}$ is regarded as T_{ex} under the LTE condition (see Section 3.2). In case of turbulence dominating the internal support, σ is replaced by the total velocity dispersion $\sigma_{\rm tot}$, which can be calculated as

$$\sigma_{\rm tot} = \sqrt{c_s^2 + \sigma_{\rm NT}^2} = \sqrt{c_s^2 + \sigma_{\rm obs}^2 - \sigma_{\rm T,obs}^2}. \tag{7}$$

Here $\sigma_{\rm NT}$ is the nonthermal velocity dispersion, which can be obtained by subtracting the thermal velocity dispersion ($\sigma_{\rm T,obs}$) from the observed velocity dispersion ($\sigma_{\rm obs}$). We have derived the ^{13}CO line width (Δv) of the filaments, so the observed

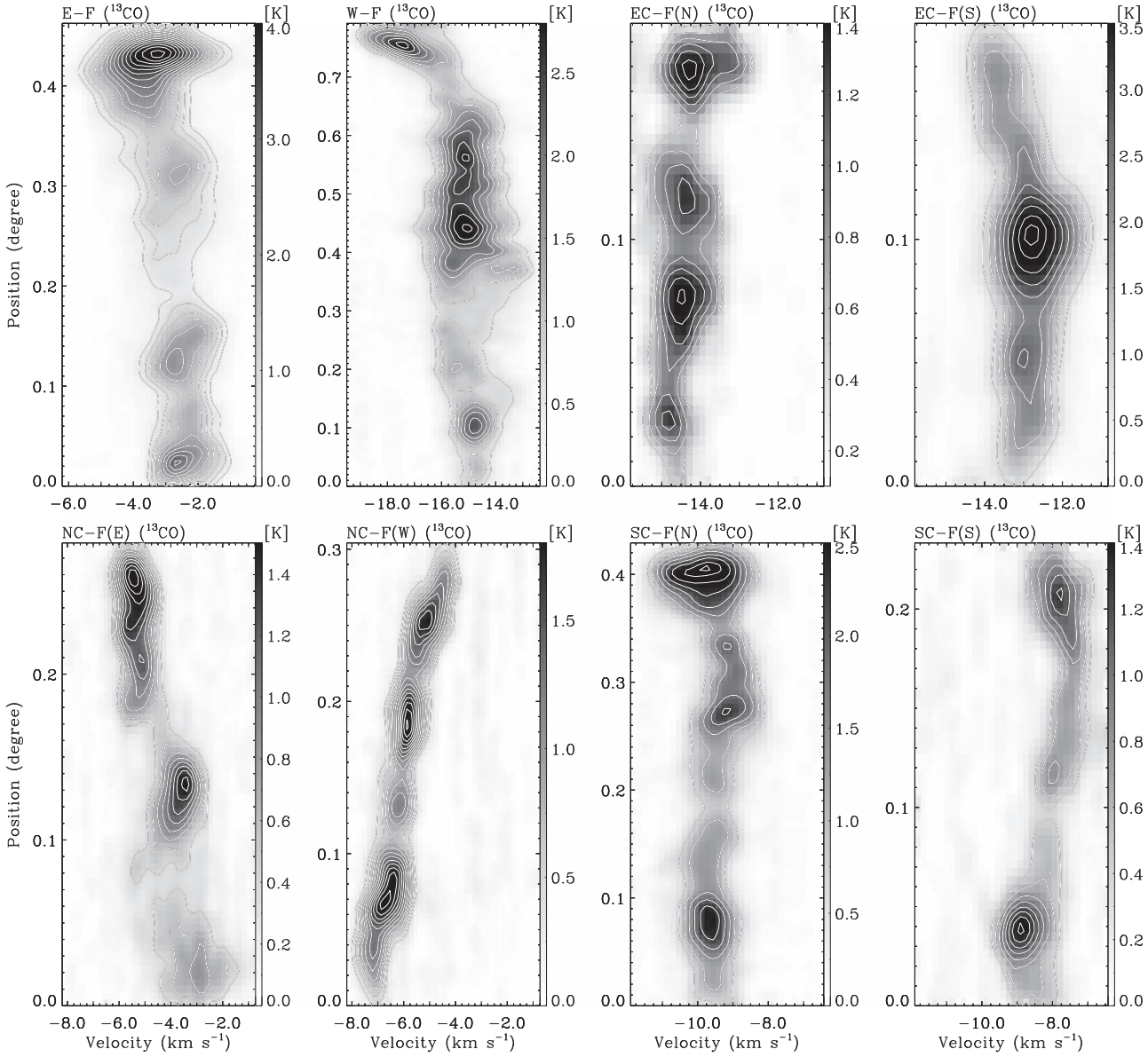

Figure 15. The ^{13}CO *PV* plots of the identified filaments extracted along the directions of the solid arrowed lines and with the widths of the dashed boxes shown in Figures 6, 8, 10, 12, and 14. The contours are overlaid from 10σ at intervals of 5σ for E-F, W-F, EC-F(S), and SC-F(N) and from 5σ at intervals of 2σ for the rest (σ is the rms noise level in each plot).

velocity dispersion ($\sigma_{\rm obs}$) is $\frac{\Delta v}{\sqrt{8\ln 2}}$. The thermal velocity dispersion ($\sigma_{\rm T,obs}$) is $\sqrt{\frac{k_{\rm B}T_{\rm kin}}{\mu_{\rm obs}m_{\rm H}}}$. Therefore, the critical line mass becomes the virial line mass per unit length $M_{\rm Vir} = 2\sigma_{\rm tot}^2/G$ (Fiege & Pudritz 2000).

By calculating these parameters, we compare our observations with scenarios of thermal or turbulent support in the filaments. The results are listed in Table 2. Figure 18 illustrates the relationship between the ratio of nonthermal velocity dispersion to isothermal sound speed and the mean H_2 column density traced by the ^{13}CO emission in the filaments. The ratio ($\sigma_{\rm NT}/c_{\rm s}$) ranges from 1.84 to 4.20. For most filaments, the nonthermal (turbulent) motions are supersonic ($\sigma_{\rm NT}/c_{\rm s} > 2$; see the dashed green line in Figure 18). Basically, the ratio ($\sigma_{\rm NT}/c_{\rm s}$) increases with the mean column density ($N_{\rm H_2}$), and the relationship can be fitted with a power law of $\sigma_{\rm NT}/c_{\rm s} \propto N_{\rm H_2}^{(0.36\pm0.09)}$. We further calculate the $M_{\rm thermal}$ of each filament; the results are 9.83 (E-F), 9.39 (EC-F(N)), 8.21 (EC-F(S)), 10.18 (NC-F(E)), 11.59 (NC-F(W)), 10.09 (SC-F(N)), 7.35 (SC-F(S)), and 11.58 (W-F) in units of $M_\odot$ pc^{-1}. Compared to the LTE line mass, we find that all of the filaments are thermally supercritical, with the LTE mass ($M_{\rm LTE}$) much larger than the critical mass ($M_{\rm thermal}$) by factors of 2.55–15.62. We also calculate the virial line mass ($M_{\rm Vir}$) of each filament (see the last column of Table 2), which is more consistent with the observed LTE line mass. Clearly, in our observations, thermal pressure is not enough to support the fragmentation of filaments. The turbulence should be the dominant support against the radial collapse. Therefore, instability along the filaments and subsequent fragmentation can develop (Jackson et al. 2010; Wang et al. 2014; Beuther et al. 2015; Lu et al. 2018).

In Figure 19, we present the relationship between virial and LTE line mass. Only EC-F(N) has a virial parameter ($\alpha_{\rm Vir} = M_{\rm Vir}/M_{\rm LTE}$) larger than 2, with a value of 2.04; thus,

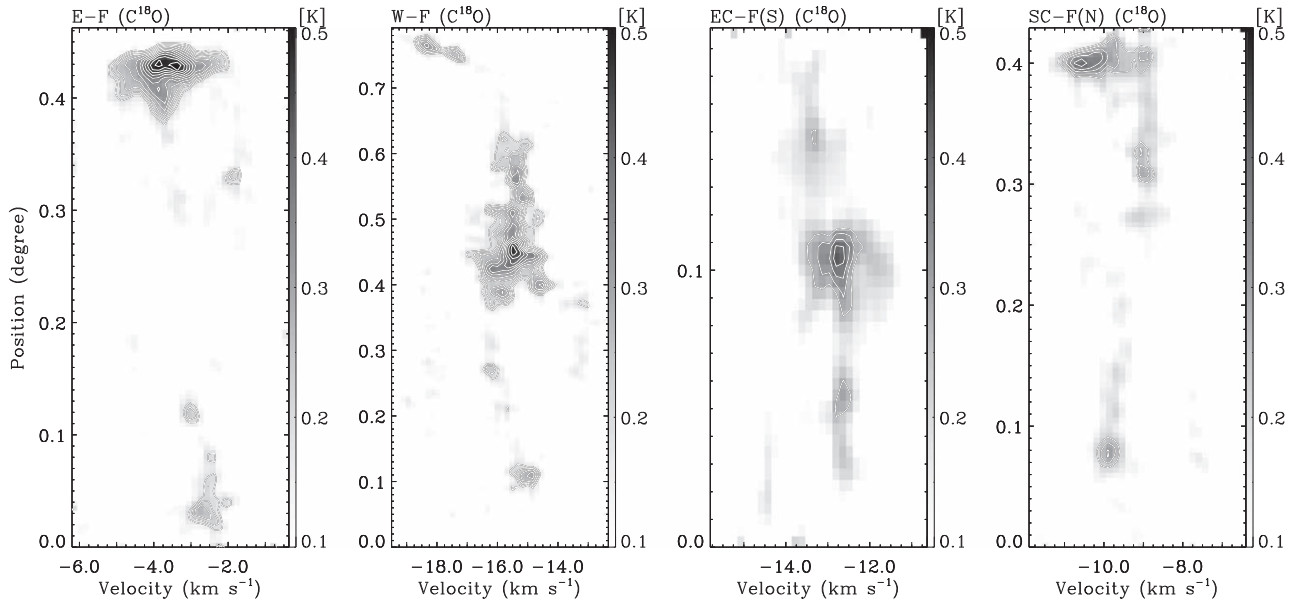

Figure 16. The $C^{18}O$ *PV* plots of the identified filaments extracted along the directions of the solid arrowed lines and with the widths of the dashed boxes shown in Figures 6, 8, 12, and 14. The contours are overlaid from 3σ at intervals of 0.5σ for E-F, W-F, EC-F(S), and SC-F(N) (σ is the rms noise level in each plot).

it tends to be gravitationally unbound and unvirialized. All of the rest of the filaments have virial parameters smaller than 2, and four of them have a virial line mass close to the LTE line mass: E-F ($\alpha_{\rm Vir} = 1.21$), EC-F(S) ($\alpha_{\rm Vir} = 0.92$), SC-F(N) ($\alpha_{\rm Vir} = 0.80$), and W-F ($\alpha_{\rm Vir} = 1.06$). These four filaments are the ones with detectable $C^{18}O$ emission (see Section 3), indicating that they are more condensed than the other filaments and more likely to be gravitationally bound. Arzoumanian et al. (2013) also found that the thermally supercritical filaments detected by the *Herschel* Gould Belt Survey are self-gravitating structures in a rough virial balance with $M_{\rm Vir} \sim M_{\rm LTE}$. Shown in Figure 19, the correlation can be fitted as a power law of $M_{\rm Vir} \propto M_{\rm LTE}^{0.66\pm0.10}$, which is also similar to the result ($M_{\rm Vir} \propto M_{\rm LTE}^{0.76}$) for the gravitationally bound filaments in Arzoumanian et al. (2013).

4.2. CO Clumps along Filaments

To further study fragmentation within the filaments, we adopt the *Clumpfind* algorithm (Williams et al. 1994) to extract the dense clumps. This algorithm searches for the local peaks of emission and follows them down to the lower intensity levels. The end result is a decomposition of the data cube into a set of structural units ("clumps") in which the emission is concentrated. We use the ^{13}CO data cube of each region as the input cube. We set "low" (the minimum value where the algorithm starts contouring the data) as 3.5 times the rms, "inc" (the minimum difference between the peak emission and the lowest emission of a clump) as 1 times the rms, and other parameters as the default values. The results are listed in Table 3.

Along with the clump identification, we also derive the radius, excitation temperature, H_2 volume density, line width, nonthermal velocity dispersion, and thermal velocity dispersion. Based on these parameters, we further calculate the clump LTE mass $M_{\rm LTE,c} = \mu m_{\rm H}(4\pi R^3/3)n$, clump virial mass $M_{\rm Vir,c} = \sigma_{\rm 3D}^2 R/G = 3(\sigma_{\rm NT}^2 + c_{\rm s}^2)R/G$ (MacLaren et al. 1988; Williams et al. 1994), and clump Jeans mass $M_{\rm Jeans,c} = \pi^{5/2} c_{\rm s}^3 / 6\sqrt{G^3 \mu m_{\rm H} n}$ (Gibson et al. 2009; Wang et al. 2014). We associate these clumps, whose positions and velocities are within the emission area and velocity component of the filament, with the filament. The results are shown in the last column of Table 3.

In Figure 20, we present correlations between different masses ($M_{\rm Jeans,c}$, $M_{\rm Vir,c}$, and $M_{\rm LTE,c}$) of clumps located on the filaments. For most of the clumps, both the Jeans mass and the virial mass are larger than the LTE mass, indicating that the thermal and nonthermal motions (e.g., turbulence) are working together to support the clumps against the gravity. We also find that the LTE mass is more correlated with the virial mass, as they present a robust power-law relationship. However, there is no clear correlation between the LTE mass and the Jeans mass.

Figure 21 shows the positions of clumps identified in each region. We mark the virialized clumps ($M_{\rm Vir,c}/M_{\rm LTE,c} < 2$) with red circles and unvirialized clumps ($M_{\rm Vir,c}/M_{\rm LTE,c} > 2$) with blue circles. Previous works (André et al. 2010; Men'shchikov et al. 2010) suggested that the spatial distribution of dense cores is closely related to the filamentary network. In IRDC G011.11−0.12 (Henning et al. 2010) and the Aquila cloud (Könyves et al. 2015), about 75% of the detected protostellar cores are found to be located within the filamentary structures. In our case, among the clumps identified in each region, ∼64% of them, on average, are located on the filamentary structures. The virialized clumps are located at the northern end of E-F, the middle part of EC-F(S), and the middle part of W-F.

We also find that the virialized clumps located on E-F and W-F are consistent with the locations of the velocity oscillations (see Figure 15) of the filaments. As pointed out by Hacar & Tafalla (2011), the velocity oscillations corresponding to the dense cores could indicate the core-forming motions during the fragmentation of the filaments. This is consistent with our result in the last section that E-F and W-F are gravitationally bound, and subsequent fragmentation could happen within the filaments.

Table 1
Distances to Filamentary Structures in Each Region

Region	Filament	$(l, b, v)_1$ (deg, deg, km s^{-1})	d_1 (kpc)	$(l, b, v)_2$ (deg, deg, km s^{-1})	d_2 (kpc)	$(l, b, v)_3$ (deg, deg, km s^{-1})	d_3 (kpc)	Distance (kpc)
(1)	(2)	(3)	(4)	(5)	(6)	(7)	(8)	(9)
Eastern region	E-F	(174.43, −0.36, −2.3)	1.68 ± 0.12	(174.34, −0.15, −3.0)	1.68 ± 0.12	(174.20, −0.07, −4.0)	1.68 ± 0.12	1.68
Eastern central region	EC-F(N)	(173.63, 0.14, −15.0)	1.72 ± 0.15	(173.61, 0.09, −14.3)	1.72 ± 0.15	(173.59, 0.01, −13.7)	1.72 ± 0.15	1.72
	EC-F(S)	(173.56, −0.01, −13.2)	1.72 ± 0.15	(173.51, −0.06, −12.5)	1.71 ± 0.15	(173.46, −0.11, −13.8)	1.73 ± 0.16	
Northern central region	NC-F(E)	(172.57, −0.07, −3.0)	1.69 ± 0.13	(172.48, −0.03, −3.8)	1.69 ± 0.13	(172.38, 0.01, −5.5)	1.70 ± 0.14	1.70
	NC-F(W)	(172.27, 0.02, −6.6)	1.72 ± 0.15	(172.16, 0.05, −5.5)	1.71 ± 0.15	(172.11, 0.09, −4.9)	1.71 ± 0.14	
Southern central region	SC-F(N)	(172.44, −0.44, −9.6)	1.76 ± 0.20	(172.59, −0.35, −9.2)	1.74 ± 0.18	(172.73, −0.33, −10.1)	1.74 ± 0.18	1.73
	SC-F(S)	(172.75, −0.57, −8.8)	1.73 ± 0.17	(172.82, −0.53, −8.0)	1.72 ± 0.16	(172.89, −0.48, −7.8)	1.72 ± 0.15	
Western region	W-F	(170.38, −0.39, −14.7)	1.90 ± 0.24	(170.65, −0.24, −15.0)	1.90 ± 0.24	(170.82, 0.02, −17.8)	1.91 ± 0.24	1.90

Note. Distances to the filamentary structures estimated by the Bayesian approach. Columns 3, 5, and 7 are the coordinates of the three chosen points located in each filament mentioned in Section 3.7. Columns 4, 6, and 8 are the distances to these three points derived by the Bayesian distance estimation program. Column 9 is the distance to the filament in each region.

Table 2
Properties of Filamentary Structures

Filament	Length	Width	T_{ex}	N_{H_2} (^{13}CO)	N_{H_2} (C^{18}O)	M_{LTE} (^{13}CO)	Δv (^{13}CO)	σ_{NT}	c_s	σ_{tot}	M_{Vir}
	(pc)	(pc)	(K)	(10^{21} cm^{-2})	(10^{21} cm^{-2})	($M_\odot$ pc^{-1})	(km s^{-1})	(km s^{-1})	(km s^{-1})	(km s^{-1})	($M_\odot$ pc^{-1})
(1)	(2)	(3)	(4)	(5)	(6)	(7)	(8)	(9)	(10)	(11)	(12)
E-F	15.15	1.33 ± 0.02	8.72 ± 0.97	4.77 ± 0.49	8.37 ± 0.11	151.43	1.44 ± 0.08	0.611	0.146	0.627	182.96
EC-F(N)	7.01	0.82 ± 0.01	8.02 ± 0.82	1.26 ± 0.16	···	23.91	0.68 ± 0.05	0.289	0.142	0.323	48.65
EC-F(S)	6.38	0.76 ± 0.01	9.60 ± 1.23	6.53 ± 0.69	7.94 ± 0.12	128.26	1.15 ± 0.06	0.488	0.133	0.505	118.54
NC-F(E)	9.52	0.83 ± 0.01	8.93 ± 0.96	1.53 ± 0.19	···	46.79	0.95 ± 0.06	0.407	0.148	0.431	86.29
NC-F(W)	11.01	0.84 ± 0.01	9.41 ± 1.01	1.72 ± 0.23	···	35.78	0.82 ± 0.05	0.345	0.158	0.380	67.07
SC-F(N)	14.59	1.13 ± 0.01	8.99 ± 0.99	2.94 ± 0.32	5.05 ± 0.07	105.88	0.94 ± 0.05	0.401	0.148	0.428	85.02
SC-F(S)	8.05	1.29 ± 0.01	6.16 ± 0.49	0.70 ± 0.09	···	20.24	0.54 ± 0.04	0.231	0.261	0.270	31.75
W-F	28.45	2.07 ± 0.03	8.13 ± 0.74	2.12 ± 0.25	3.52 ± 0.05	161.91	1.38 ± 0.08	0.585	0.158	0.606	170.93

Note. Properties of the identified filaments, including the length of each filament (column 2), width of each filament (column 3), excitation temperature (column 4), and line width in the ^{13}CO emission (column 8). Columns 5–6 are mean H_2 column density traced by ^{13}CO and C^{18}O. Columns 9–11 are the nonthermal, thermal, and total velocity dispersion. Columns 7 and 12 are the LTE and virial line mass, respectively.

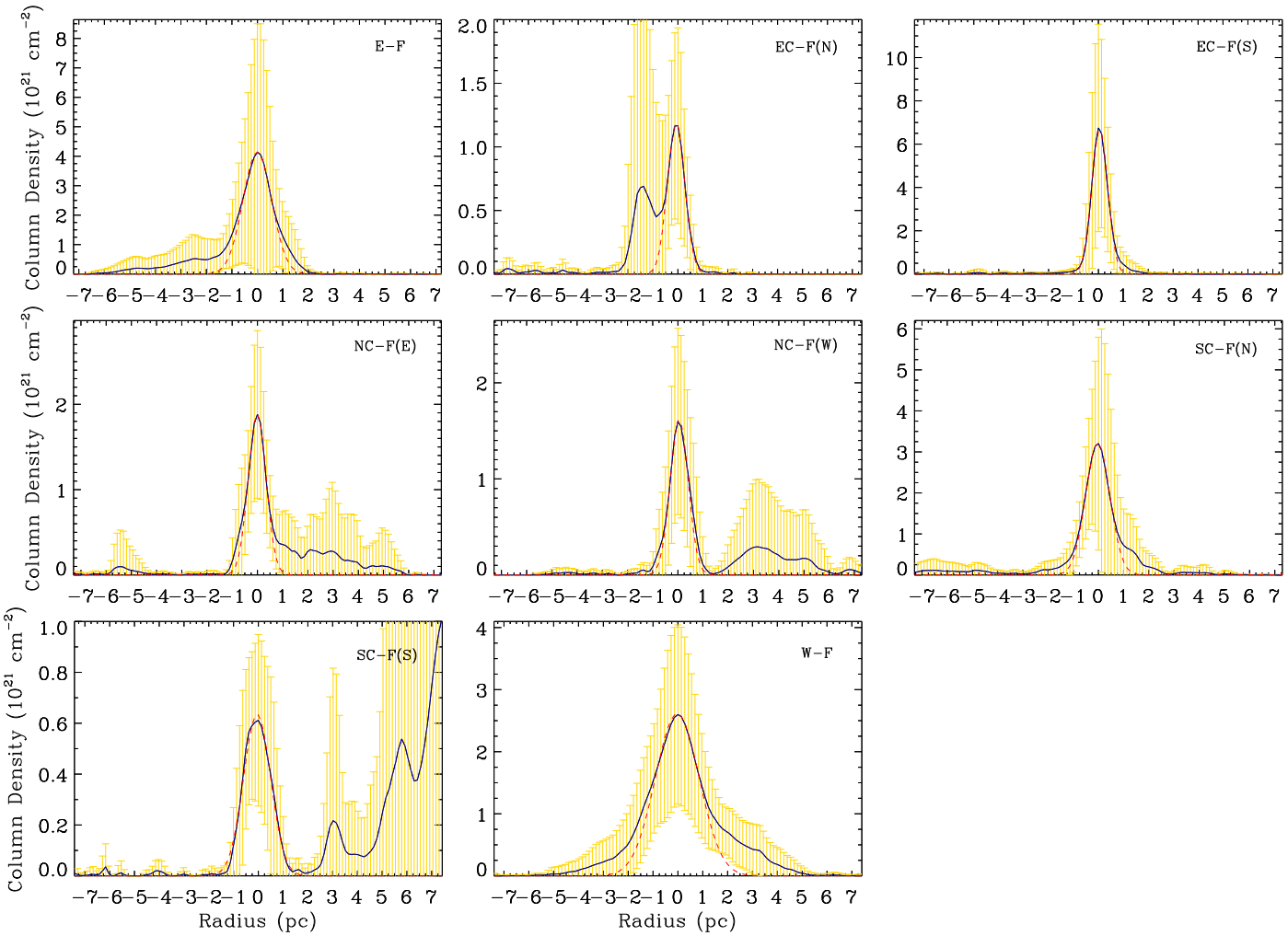

Figure 17. Mean radial column density profiles perpendicular to the filamentary structures (navy curves). The position of the peak density in each profile is regarded as the center of the profile and thus the position of $R = 0$. The $R < 0$ and $R > 0$ parts of each profile correspond to the left and right sides of each filament. The yellow areas show the $\pm 1\sigma$ dispersion of the distributions of radial profiles along the filaments. The dashed red curves show the Gaussian fittings to the inner parts of the profiles.

4.3. YSO Candidates along Filaments

With the IR data from the 2MASS, *WISE*, and GLIMPSE 360 surveys, we investigate YSO candidates in these five regions. The YSOs can be classified into disk-bearing YSOs and diskless YSOs according to the presence of circumstellar disks. The IR emission excess created by dusty circumstellar

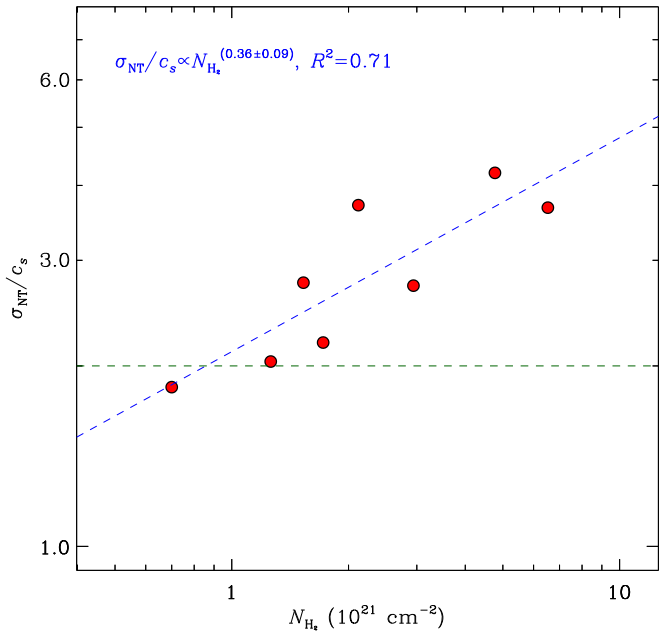

Figure 18. Relationship between the ratio of nonthermal velocity dispersion (σ_{NT}) to isothermal sound speed (c_s) and the mean H_2 column density (N_{H_2}) traced by the ^{13}CO emission of filaments. The dashed green line marks the position of $\sigma_{NT}/c_s = 2$. The dashed blue line is the power-law fitting of the correlation. Here R^2 is the correlation coefficient in the unit of percentage.

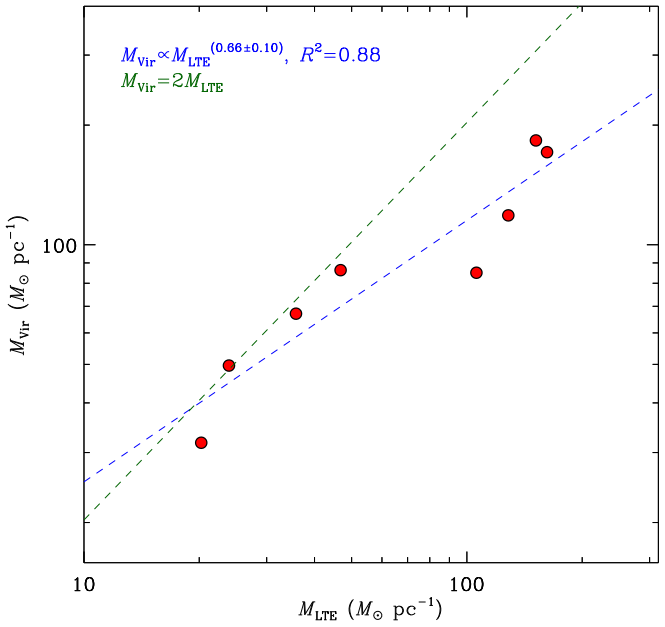

Figure 19. Relationship between the virial line mass (M_{Vir}) and the LTE line mass (M_{LTE}) of the filaments. The dashed blue line is the power-law fitting of the correlation. The dashed green line marks the position where the virial parameter equals 2. Here R^2 is the correlation coefficient in the unit of percentage.

disks makes the IR colors of disk-bearing YSOs different from those of diskless YSOs. The diskless YSOs are unable to be identified only based on their IR colors. So in this work, we only focus on the disk-bearing YSOs, namely Class I and Class II objects. Following the scheme provided by Koenig & Leisawitz (2014), we first remove the star-forming galaxies and broad-line active galactic nuclei (AGNs) as extragalactic contaminants according to their locations in the *WISE* $W1-W2$ versus $W2-W3$ and $W1$ versus $W1-W3$ color–color diagrams (top panels of Figure 22). Then we select the YSO candidates based on their locations in the *WISE* $W1-W2$ versus $W2-W3$ color–color diagram, which is shown in panel (c) of Figure 22. With the 2MASS H and K_s bands, we use the $H-K_s$ versus $W1-W2$ color–color diagram (panel (d) of Figure 22) to search for the YSO candidates among previously unclassified objects. *WISE* $W4$ photometry is also introduced to identify transition disks and retrieve protostars from the AGNs. Finally, we use a combination of the *WISE* $W1-W2$ versus $W3-W4$ and $W1$ versus $W1-W2$ diagrams to remove the asymptotic giant branch (AGB) stars.

Since the latitudes of our regions are within $-1°$ to $1°$, we further use the GLIMPSE 360 data to identify additional YSOs. Following the Phase II classification scheme of Gutermuth et al. (2009), we first select the additional Class I and Class II objects according to the $K_s-[3.6]$ versus $[3.6]-[4.5]$ color–color diagram (panel (e) of Figure 22). Then we adopt the criteria in Saral et al. (2015) to remove the extragalactic contaminants and AGB stars. We combine these additional YSOs with the YSOs identified from *WISE* data and list the IR photometric magnitudes and classifications of all of the YSOs in Table 4.

As shown in Figure 23, there are two groups of Class II objects located at the two ends of E-F. No Class I object is identified to be associated with E-F. In the eastern central region, one Class I object is found to be located on EC-F(N), and another one is located at the center of EC-F(S), where the virialized clump is also identified (see Figure 21). A number of Class II objects are also located along EC-F(S). In the northern central region, only a few Class II objects are found near the central parts of NC-F(E) and NC-F(W). For SC-F(N), about six Class I objects are located near the center and two ends. At one end of SC-F(S) are located one Class I and one Class II object, and at the other end is a group of Class II objects. For W-F, a number of Class I objects are identified near four locations ($l \sim 170.^\circ81$, $b \sim 0.^\circ01$), ($l \sim 170.^\circ74$, $b \sim -0.^\circ09$), ($l \sim 170.^\circ65$, $b \sim -0.^\circ28$), and ($l \sim 170.^\circ35$, $b \sim -0.^\circ38$). At each location, a group of Class II objects is located around the Class I objects.

We also note that the distributions of YSOs are related to the emission areas with higher temperatures ($T_{ex} > 15$ K) of the filaments (e.g., E-F and W-F). Moreover, the filaments associated with more YSOs tend to have higher temperatures than the ones with fewer YSOs (e.g., EC-F(S) and EC-F(N), SC-F(N) and SC-F(S)). As pointed out by Gong et al. (2016), the star-forming molecular gas tends to have a higher excitation temperature than the non-star-forming molecular gas. In our case, the existing YSOs could be the possible internal heating sources of the molecular gas with higher temperature.

4.4. Outflows within Filaments

Using the ^{12}CO *PV* maps, we further search for the protostellar outflows within each filament. As shown in Figure 24, only two filaments (E-F and W-F) are identified with evident spur structures in *PV* diagrams. We name these structures "E-F_Spur," "W-F_Spur1," "W-F_Spur2," and "W-F_Spur3" and the corresponding outflows "E-F_OF," "W-F_OF1," "W-F_OF2," and "W-F_OF3." The velocities of the ^{13}CO peak emission at the positions of these spur structures are regarded as the velocities of the line centers (v_{center}). The velocity ranges of the outflow wings are derived from ^{12}CO velocity components near the line centers where the ^{12}CO

Table 3
Properties of Clumps in Each Region

Clump	Velocity ($km\ s^{-1}$)	Radius (pc)	T_{ex} (K)	n_{H_2} ($10^2\ cm^{-3}$)	$M_{LTE,c}$ ($M_\odot$)	Δv ($km\ s^{-1}$)	σ_{NT} ($km\ s^{-1}$)	c_s ($km\ s^{-1}$)	σ_{3D} ($km\ s^{-1}$)	$M_{Vir,c}$ ($M_\odot$)	$M_{Jeans,c}$ ($M_\odot$)	Region	Filament
(1)	(2)	(3)	(4)	(5)	(6)	(7)	(8)	(9)	(10)	(11)	(12)	(13)	(14)
MWISP G174.200−00.075	−4.21	1.339	14.36	2.32	137.35	0.927	0.388	0.226	0.778	240.52	31.34	Eastern	E-F
MWISP G174.192−00.075	−3.71	1.499	12.82	2.03	198.21	1.287	0.543	0.213	1.011	519.12	28.28	Eastern	E-F
MWISP G174.383−00.367	−3.05	0.978	13.28	1.14	23.70	0.827	0.346	0.217	0.707	139.87	39.72	Eastern	E-F
MWISP G174.425−00.358	−2.05	1.069	15.62	1.68	42.01	0.885	0.370	0.235	0.759	175.11	41.80	Eastern	E-F
MWISP G174.425−00.225	−1.88	1.324	11.86	0.76	42.06	0.888	0.373	0.205	0.737	218.63	41.11	Eastern	E-F
MWISP G174.392−00.267	−3.05	1.234	12.09	0.95	38.52	0.837	0.350	0.207	0.705	180.84	37.78	Eastern	E-F
MWISP G174.308−00.142	−3.05	1.061	11.88	1.92	45.45	1.098	0.462	0.205	0.876	267.47	25.94	Eastern	E-F
MWISP G174.450−00.358	−3.05	0.884	15.51	1.57	20.72	0.712	0.295	0.235	0.653	93.80	42.75	Eastern	E-F
MWISP G174.458−00.425	−1.55	0.502	11.76	1.17	2.22	0.581	0.240	0.204	0.546	35.49	32.73	Eastern	…
MWISP G174.333−00.150	−3.38	1.129	11.56	1.27	33.50	0.917	0.385	0.202	0.753	198.43	30.59	Eastern	E-F
MWISP G174.408−00.317	−2.55	1.164	13.03	1.49	31.30	0.898	0.377	0.215	0.751	196.54	33.83	Eastern	E-F
MWISP G174.508−00.292	−3.88	0.985	10.81	1.22	23.01	0.804	0.337	0.196	0.675	133.14	28.27	Eastern	…
MWISP G174.292−00.117	−2.71	1.154	12.25	1.90	53.57	1.186	0.500	0.208	0.938	339.41	27.30	Eastern	E-F
MWISP G174.242−00.100	−4.71	1.374	13.34	1.69	138.07	1.274	0.537	0.218	1.004	466.28	32.85	Eastern	E-F
MWISP G174.483−00.267	−4.04	1.087	10.90	1.50	31.82	0.928	0.390	0.197	0.757	195.83	25.81	Eastern	…
MWISP G174.508−00.258	−4.37	1.172	11.00	1.37	32.01	0.943	0.397	0.198	0.767	218.07	27.34	Eastern	…
MWISP G174.292−00.083	−2.71	0.619	9.83	2.02	8.79	1.204	0.508	0.187	0.938	187.55	19.03	Eastern	E-F
MWISP G174.258−00.067	−2.71	1.179	11.48	1.32	56.81	1.343	0.568	0.202	1.043	445.14	29.65	Eastern	E-F
MWISP G174.367−00.150	−2.22	1.122	11.23	0.84	27.06	1.049	0.442	0.200	0.840	258.43	35.93	Eastern	E-F
MWISP G174.583−00.275	−2.71	0.917	10.84	0.96	7.06	0.689	0.287	0.196	0.602	91.07	31.97	Eastern	…
MWISP G174.183+00.000	−2.55	1.034	9.09	0.65	19.79	1.430	0.605	0.180	1.093	441.90	29.76	Eastern	E-F
MWISP G174.583−00.242	−3.38	1.061	10.58	0.71	13.11	0.840	0.353	0.194	0.697	156.73	35.96	Eastern	…
MWISP G174.508−00.342	−2.22	0.794	12.70	0.81	6.81	0.691	0.287	0.212	0.618	79.25	44.15	Eastern	…
MWISP G174.558−00.283	−3.05	0.907	11.43	1.00	8.72	0.697	0.291	0.201	0.612	92.26	33.88	Eastern	…
MWISP G174.583−00.300	−2.88	0.745	10.20	1.06	5.98	0.755	0.316	0.190	0.639	88.92	27.69	Eastern	…
MWISP G174.492−00.358	−3.38	0.394	11.13	1.16	1.08	0.455	0.185	0.199	0.470	17.05	30.26	Eastern	…
MWISP G174.475−00.375	−2.55	0.605	12.51	0.68	1.93	0.422	0.169	0.211	0.468	22.53	47.06	Eastern	E-F
MWISP G174.467−00.333	−2.55	0.706	13.77	1.36	10.95	0.709	0.294	0.221	0.638	74.21	38.46	Eastern	E-F
MWISP G174.700−00.167	−2.05	0.284	7.93	1.39	0.48	0.486	0.201	0.168	0.454	14.08	16.65	Eastern	…
MWISP G174.708−00.158	−1.05	0.342	7.85	1.14	0.58	0.477	0.197	0.167	0.447	16.27	18.04	Eastern	…
MWISP G174.533−00.358	−2.55	0.554	11.21	0.82	2.40	0.570	0.235	0.199	0.534	37.60	36.28	Eastern	…
MWISP G174.483−00.392	−2.22	0.483	10.66	0.72	1.41	0.684	0.285	0.194	0.598	47.25	35.90	Eastern	…
MWISP G174.208−00.025	−4.71	0.907	11.52	1.20	39.74	1.328	0.561	0.202	1.033	334.75	31.36	Eastern	E-F
MWISP G174.517−00.283	−2.38	0.745	11.18	0.61	13.86	0.691	0.288	0.199	0.606	74.33	42.15	Eastern	…
MWISP G174.517−00.358	−3.05	0.370	11.96	0.81	0.89	0.362	0.142	0.206	0.433	10.14	40.21	Eastern	…
MWISP G174.692−00.192	−2.22	0.284	8.08	0.98	0.23	0.410	0.167	0.169	0.412	10.01	20.38	Eastern	…
MWISP G174.442−00.292	−3.05	1.024	12.59	1.13	24.66	0.812	0.340	0.211	0.693	141.16	36.86	Eastern	E-F
MWISP G174.492−00.217	−5.20	0.807	9.12	0.66	8.28	0.784	0.329	0.180	0.649	103.68	29.64	Eastern	…
MWISP G174.475−00.308	−2.22	0.758	12.11	0.70	8.29	0.689	0.287	0.207	0.613	75.29	44.13	Eastern	…
MWISP G174.475−00.217	−5.20	0.394	9.41	1.68	1.56	0.775	0.325	0.183	0.646	49.53	19.53	Eastern	…
MWISP G174.250−00.100	−5.37	0.917	11.35	0.55	28.56	0.765	0.320	0.201	0.654	112.38	45.06	Eastern	E-F
MWISP G174.317−00.108	−1.22	0.874	8.35	0.32	11.68	0.568	0.236	0.172	0.506	58.94	37.32	Eastern	E-F
MWISP G174.467−00.308	−2.88	0.589	12.27	0.94	3.20	0.583	0.240	0.209	0.551	41.88	38.95	Eastern	E-F
MWISP G174.158+00.008	−2.88	0.394	9.80	0.98	0.65	0.575	0.238	0.186	0.524	27.19	27.11	Eastern	E-F
MWISP G174.558−00.325	−2.05	0.635	9.89	0.60	2.24	0.767	0.321	0.187	0.644	78.15	35.37	Eastern	…
MWISP G174.533−00.317	−3.21	0.394	9.29	0.62	0.49	0.422	0.172	0.182	0.433	14.65	31.62	Eastern	…

Table 3
(Continued)

Clump	Velocity ($km\ s^{-1}$)	Radius (pc)	T_{ex} (K)	n_{H_2} ($10^2\ cm^{-3}$)	$M_{LTE,c}$ ($M_\odot$)	Δv ($km\ s^{-1}$)	σ_{NT} ($km\ s^{-1}$)	c_s ($km\ s^{-1}$)	σ_{3D} ($km\ s^{-1}$)	$M_{Vir,c}$ ($M_\odot$)	$M_{Jeans,c}$ ($M_\odot$)	Region	Filament
(1)	(2)	(3)	(4)	(5)	(6)	(7)	(8)	(9)	(10)	(11)	(12)	(13)	(14)
MWISP G174.250−00.100	−2.22	0.927	13.81	2.04	57.87	1.551	0.656	0.221	1.198	466.46	31.53	Eastern	E-F
MWISP G174.417−00.192	−3.38	0.884	10.58	0.67	11.14	0.945	0.397	0.194	0.766	165.02	36.98	Eastern	E-F
MWISP G173.500−00.058	−12.65	1.123	15.19	2.64	96.06	0.950	0.398	0.232	0.798	211.85	31.97	Eastern central	EC-F(S)
MWISP G173.508−00.067	−13.14	1.094	15.98	2.56	87.19	0.839	0.350	0.238	0.733	160.94	35.06	Eastern central	EC-F(S)
MWISP G173.458−00.108	−13.81	0.826	11.52	1.98	31.58	1.088	0.458	0.202	0.868	204.41	24.39	Eastern central	EC-F(S)
MWISP G173.542−00.017	−13.14	1.019	12.71	1.77	58.89	1.053	0.443	0.212	0.851	236.33	29.89	Eastern central	EC-F(S)
MWISP G173.333−00.308	−13.97	0.567	9.28	1.81	5.84	0.807	0.339	0.181	0.666	77.29	18.42	Eastern central	⋯
MWISP G173.333−00.308	−13.64	0.474	9.17	1.35	3.88	0.536	0.222	0.180	0.495	28.52	20.96	Eastern central	⋯
MWISP G173.617+00.092	−14.47	0.736	10.82	1.00	10.17	0.895	0.376	0.196	0.734	123.33	31.24	Eastern central	EC-F(N)
MWISP G173.600+00.008	−14.31	0.620	12.15	1.27	5.65	0.689	0.287	0.208	0.613	61.57	32.95	Eastern central	EC-F(N)
MWISP G173.600+00.008	−14.80	0.474	11.04	1.09	3.76	0.458	0.186	0.198	0.471	20.82	30.80	Eastern central	EC-F(N)
MWISP G173.317−00.025	−13.48	0.379	8.49	1.53	0.75	0.558	0.232	0.174	0.502	24.67	17.53	Eastern central	⋯
MWISP G173.633+00.142	−14.97	0.650	11.02	0.81	2.30	0.593	0.245	0.198	0.546	47.77	35.75	Eastern central	EC-F(N)
MWISP G173.600+00.058	−14.14	0.551	13.48	1.30	5.83	0.752	0.313	0.219	0.662	65.19	38.11	Eastern central	EC-F(N)
MWISP G173.392−00.150	−15.30	0.351	11.76	2.09	1.45	0.702	0.293	0.204	0.618	36.18	24.48	Eastern central	⋯
MWISP G173.592+00.050	−15.14	0.620	12.08	0.91	4.20	0.667	0.277	0.207	0.599	57.78	38.51	Eastern central	EC-F(N)
MWISP G173.308−00.275	−15.47	0.474	8.39	0.80	2.47	0.653	0.273	0.172	0.559	42.22	23.85	Eastern central	⋯
MWISP G173.267−00.217	−14.14	0.291	10.47	1.57	0.72	0.432	0.175	0.193	0.451	11.35	23.74	Eastern central	⋯
MWISP G173.275−00.233	−14.14	0.291	10.16	0.95	0.40	0.337	0.133	0.190	0.401	6.92	29.20	Eastern central	⋯
MWISP G173.650+00.183	−14.97	0.252	11.01	1.62	0.41	0.584	0.242	0.198	0.541	18.02	25.21	Eastern central	⋯
MWISP G173.292−00.275	−14.97	0.531	8.03	0.51	1.41	0.491	0.203	0.169	0.457	26.83	28.08	Eastern central	⋯
MWISP G173.258−00.200	−15.30	0.252	7.03	1.74	0.64	0.460	0.190	0.158	0.428	11.16	12.37	Eastern central	⋯
MWISP G173.267−00.058	−14.14	0.068	6.48	2.97	0.12	0.347	0.141	0.152	0.359	1.70	8.39	Eastern central	⋯
MWISP G173.642+00.167	−14.64	0.351	10.78	0.92	0.40	0.470	0.192	0.196	0.474	16.20	32.44	Eastern central	⋯
MWISP G173.408−00.158	−14.97	0.322	9.45	0.84	0.30	0.420	0.171	0.183	0.434	11.87	27.79	Eastern central	⋯
MWISP G173.600+00.033	−14.80	0.291	10.84	0.71	0.42	0.262	0.097	0.196	0.379	4.19	37.14	Eastern central	EC-F(N)
MWISP G173.600+00.033	−14.31	0.252	11.94	1.12	0.55	0.347	0.135	0.206	0.427	6.35	34.12	Eastern central	EC-F(N)
MWISP G173.467+00.108	−13.81	0.155	7.43	1.17	0.10	0.315	0.126	0.162	0.356	3.23	16.42	Eastern central	⋯
MWISP G173.392+00.183	−13.64	0.155	6.96	0.88	0.03	0.355	0.144	0.157	0.369	4.09	17.13	Eastern central	⋯
MWISP G173.258−00.233	−13.64	0.291	8.00	0.45	0.21	0.254	0.097	0.168	0.336	3.93	29.44	Eastern central	⋯
MWISP G173.317−00.242	−15.30	0.155	7.28	1.14	0.14	0.372	0.151	0.161	0.382	4.48	16.15	Eastern central	⋯
MWISP G173.567−00.033	−15.47	0.068	7.19	2.15	0.69	0.370	0.151	0.160	0.380	1.94	11.54	Eastern central	EC-F(S)
MWISP G172.108+00.083	−5.54	1.036	10.70	0.87	25.95	1.219	0.515	0.195	0.953	321.84	32.94	Northern central	NC-F(W)
MWISP G172.158+00.050	−6.04	0.997	11.62	0.95	17.94	0.802	0.336	0.203	0.680	134.17	35.74	Northern central	NC-F(W)
MWISP G172.483−00.033	−3.72	0.850	12.67	1.36	20.66	1.074	0.452	0.212	0.865	205.30	33.87	Northern central	NC-F(E)
MWISP G172.275+00.008	−7.04	0.817	11.45	1.04	11.88	0.736	0.307	0.202	0.636	92.42	33.23	Northern central	NC-F(W)
MWISP G172.250+00.017	−6.37	0.850	12.88	1.12	13.17	0.681	0.283	0.214	0.614	82.44	38.26	Northern central	NC-F(W)
MWISP G172.742−00.017	−5.38	0.488	7.80	1.72	5.01	0.971	0.410	0.166	0.766	96.39	14.59	Northern central	⋯
MWISP G172.750−00.092	−5.05	0.525	9.76	1.65	6.06	0.792	0.332	0.186	0.659	68.87	20.82	Northern central	⋯
MWISP G172.292+00.050	−7.37	0.780	12.45	0.87	8.36	0.729	0.304	0.210	0.640	86.70	41.26	Northern central	NC-F(W)
MWISP G172.392−00.025	−5.88	0.767	13.97	1.13	12.76	0.671	0.278	0.223	0.617	72.20	43.10	Northern central	NC-F(E)
MWISP G172.208+00.008	−6.54	0.728	11.72	1.03	7.87	0.757	0.316	0.204	0.652	87.25	34.74	Northern central	NC-F(W)
MWISP G172.417−00.042	−5.21	0.827	11.31	1.07	13.34	0.935	0.393	0.200	0.764	151.17	32.22	Northern central	NC-F(E)
MWISP G172.400+00.008	−5.54	0.688	12.96	1.62	7.80	0.908	0.381	0.214	0.757	118.68	32.16	Northern central	NC-F(E)
MWISP G172.342−00.008	−5.71	0.626	11.03	0.94	3.39	0.699	0.292	0.198	0.610	63.99	33.09	Northern central	NC-F(E)
MWISP G172.758−00.092	−5.88	0.422	8.23	1.08	3.54	0.491	0.203	0.171	0.460	21.33	19.88	Northern central	⋯

Table 3
(Continued)

Clump	Velocity ($km\ s^{-1}$)	Radius (pc)	T_{ex} (K)	n_{H_2} ($10^2\ cm^{-3}$)	$M_{LTE,c}$ ($M_\odot$)	Δv ($km\ s^{-1}$)	σ_{NT} ($km\ s^{-1}$)	c_s ($km\ s^{-1}$)	σ_{3D} ($km\ s^{-1}$)	$M_{Vir,c}$ ($M_\odot$)	$M_{Jeans,c}$ ($M_\odot$)	Region	Filament
(1)	(2)	(3)	(4)	(5)	(6)	(7)	(8)	(9)	(10)	(11)	(12)	(13)	(14)
MWISP G172.575−00.067	−2.89	0.561	12.49	0.81	4.46	0.533	0.218	0.210	0.525	33.32	43.02	Northern central	NC-F(E)
MWISP G172.517−00.092	−4.22	0.347	12.75	0.95	0.69	0.317	0.120	0.213	0.423	7.29	40.91	Northern central	NC-F(E)
MWISP G172.192−00.008	−6.04	0.525	9.37	0.63	1.43	0.468	0.192	0.182	0.459	24.07	31.78	Northern central	NC-F(W)
MWISP G172.575−00.067	−1.89	0.398	13.29	1.71	3.01	0.651	0.269	0.217	0.599	35.31	32.51	Northern central	NC-F(E)
MWISP G172.517−00.092	−4.55	0.153	11.45	1.14	0.40	0.184	0.054	0.202	0.361	1.09	31.77	Northern central	NC-F(E)
MWISP G172.542−00.042	−4.05	0.508	12.71	0.67	3.81	0.443	0.178	0.212	0.480	20.90	48.43	Northern central	NC-F(E)
MWISP G172.542−00.050	−4.38	0.488	12.82	0.81	4.42	0.503	0.205	0.213	0.512	25.86	44.86	Northern central	NC-F(E)
MWISP G172.800−00.150	−2.55	0.318	7.02	1.07	0.50	0.689	0.289	0.158	0.571	31.56	15.73	Northern central	⋯
MWISP G172.525−00.092	−3.72	0.288	14.29	1.91	1.60	0.565	0.231	0.225	0.559	19.19	34.25	Northern central	NC-F(E)
MWISP G172.550−00.050	−3.38	0.488	13.90	1.00	5.37	0.548	0.224	0.222	0.546	30.67	45.36	Northern central	NC-F(E)
MWISP G172.742−00.142	−5.05	0.249	11.36	2.29	1.41	0.674	0.281	0.201	0.598	23.69	22.16	Northern central	⋯
MWISP G172.583−00.067	−3.88	0.153	11.58	2.63	1.92	0.586	0.242	0.203	0.547	11.00	21.29	Northern central	NC-F(E)
MWISP G172.542−00.067	−4.71	0.153	12.39	2.00	1.21	0.405	0.161	0.210	0.458	5.26	27.01	Northern central	NC-F(E)
MWISP G172.742−00.133	−5.54	0.067	9.01	2.47	0.53	0.264	0.100	0.179	0.355	0.97	15.10	Northern central	⋯
MWISP G172.575−00.067	−3.38	0.398	14.24	0.96	1.47	0.319	0.119	0.225	0.441	8.47	48.04	Northern central	NC-F(E)
MWISP G172.525−00.017	−5.54	0.422	10.97	0.81	5.37	0.739	0.309	0.197	0.635	48.22	35.41	Northern central	NC-F(E)
MWISP G172.542−00.058	−5.38	0.153	9.81	1.48	1.58	0.435	0.177	0.187	0.445	6.06	22.19	Northern central	NC-F(E)
MWISP G172.742−00.142	−5.88	0.067	8.11	2.17	0.57	0.272	0.105	0.170	0.346	1.04	13.75	Northern central	⋯
MWISP G172.192+00.033	−5.54	0.488	11.79	0.92	5.10	0.795	0.333	0.205	0.676	64.62	37.09	Northern central	NC-F(W)
MWISP G172.517−00.025	−2.89	0.508	11.65	0.60	6.26	0.682	0.284	0.203	0.605	49.52	45.20	Northern central	NC-F(E)
MWISP G172.542−00.067	−3.72	0.398	13.49	0.59	0.77	0.259	0.091	0.219	0.410	5.59	56.43	Northern central	NC-F(E)
MWISP G172.317+00.075	−7.20	0.318	8.97	0.68	0.27	0.399	0.161	0.178	0.417	10.56	28.64	Northern central	NC-F(W)
MWISP G172.550−00.083	−4.38	0.153	10.53	1.48	1.05	0.470	0.192	0.193	0.472	7.07	24.63	Northern central	NC-F(E)
MWISP G172.725−00.333	−10.07	1.294	13.52	1.72	137.18	1.526	0.645	0.219	1.180	630.49	33.24	Southern central	SC-F(N)
MWISP G172.450−00.442	−9.91	1.147	13.67	1.52	46.94	1.006	0.423	0.220	0.826	243.01	35.97	Southern central	SC-F(N)
MWISP G172.667−00.358	−9.24	1.207	13.06	1.13	34.68	0.946	0.397	0.215	0.783	226.14	38.95	Southern central	SC-F(N)
MWISP G172.642−00.350	−8.91	0.934	14.79	1.84	23.39	0.772	0.321	0.229	0.684	116.46	36.78	Southern central	SC-F(N)
MWISP G172.600−00.342	−9.24	1.101	13.22	1.62	54.69	1.254	0.529	0.217	0.990	361.82	33.14	Southern central	SC-F(N)
MWISP G172.500−00.417	−9.74	0.879	13.47	1.73	25.43	1.099	0.463	0.219	0.886	222.08	33.00	Southern central	SC-F(N)
MWISP G172.858−00.367	−8.58	0.590	9.07	1.34	4.79	0.953	0.402	0.179	0.762	112.17	20.70	Southern central	⋯
MWISP G172.767−00.250	−10.74	0.554	8.49	1.59	5.28	0.927	0.390	0.174	0.740	99.50	17.22	Southern central	⋯
MWISP G172.550−00.392	−9.58	0.934	12.39	1.30	19.99	1.010	0.425	0.210	0.820	199.11	33.53	Southern central	SC-F(N)
MWISP G172.750−00.567	−9.08	0.740	8.17	0.78	6.07	0.722	0.303	0.170	0.602	80.80	23.13	Southern central	SC-F(S)
MWISP G172.700−00.308	−9.74	0.842	12.48	2.00	42.60	1.307	0.552	0.210	1.023	300.59	27.32	Southern central	SC-F(N)
MWISP G172.408−00.417	−9.24	1.054	13.30	0.96	28.95	0.853	0.357	0.217	0.724	160.61	43.44	Southern central	SC-F(N)
MWISP G172.542−00.725	−10.57	0.554	8.07	0.86	2.71	0.528	0.219	0.169	0.479	32.31	21.72	Southern central	⋯
MWISP G172.383−00.458	−9.74	1.054	13.18	0.87	20.79	0.834	0.349	0.216	0.711	153.20	45.04	Southern central	SC-F(N)
MWISP G172.883−00.483	−7.92	0.781	8.19	0.86	6.23	0.800	0.336	0.170	0.653	104.58	22.15	Southern central	SC-F(S)
MWISP G172.525−00.733	−9.91	0.590	7.71	0.64	2.31	0.442	0.182	0.165	0.425	24.09	23.47	Southern central	⋯
MWISP G172.858−00.483	−7.75	0.624	9.15	1.05	2.81	0.628	0.262	0.180	0.550	51.38	23.69	Southern central	SC-F(S)
MWISP G172.542−00.733	−10.24	0.454	7.33	0.45	1.06	0.256	0.099	0.161	0.327	6.20	25.89	Southern central	⋯
MWISP G172.508−00.725	−9.41	0.684	8.96	0.96	3.74	0.863	0.363	0.178	0.701	106.60	24.00	Southern central	⋯
MWISP G172.342−00.342	−7.25	0.430	8.51	0.70	1.78	0.717	0.301	0.174	0.601	46.24	26.10	Southern central	⋯
MWISP G172.733−00.292	−10.90	0.923	9.35	0.64	9.05	0.825	0.347	0.182	0.678	131.54	31.38	Southern central	⋯
MWISP G172.442−00.617	−7.75	0.477	7.68	0.86	1.74	0.636	0.266	0.165	0.542	40.33	20.15	Southern central	⋯
MWISP G172.750−00.283	−10.74	0.254	9.80	1.81	0.83	0.578	0.240	0.186	0.526	17.71	20.03	Southern central	SC-F(N)

Table 3
(Continued)

Clump	Velocity ($km\ s^{-1}$)	Radius (pc)	T_{ex} (K)	n_{H_2} ($10^2\ cm^{-3}$)	$M_{LTE,c}$ ($M_\odot$)	Δv ($km\ s^{-1}$)	σ_{NT} ($km\ s^{-1}$)	c_s ($km\ s^{-1}$)	σ_{3D} ($km\ s^{-1}$)	$M_{Vir,c}$ ($M_\odot$)	$M_{Jeans,c}$ ($M_\odot$)	Region	Filament
(1)	(2)	(3)	(4)	(5)	(6)	(7)	(8)	(9)	(10)	(11)	(12)	(13)	(14)
MWISP G172.817−00.525	−8.25	0.654	8.47	0.76	2.48	0.606	0.253	0.173	0.531	50.23	24.86	Southern central	SC-F(S)
MWISP G172.792−00.558	−8.08	0.497	7.31	0.75	1.46	0.576	0.240	0.161	0.501	34.51	20.06	Southern central	SC-F(S)
MWISP G172.375−00.492	−9.24	0.831	11.15	0.47	6.03	0.525	0.216	0.199	0.508	47.85	47.42	Southern central	SC-F(N)
MWISP G172.875−00.467	−7.58	0.534	8.86	1.06	2.20	0.480	0.197	0.177	0.460	25.73	22.49	Southern central	SC-F(S)
MWISP G172.342−00.517	−10.24	0.477	10.04	0.79	3.72	0.639	0.266	0.189	0.565	40.76	31.36	Southern central	SC-F(N)
MWISP G172.750−00.608	−8.75	0.293	7.10	1.54	0.82	0.694	0.291	0.159	0.575	29.51	13.38	Southern central	SC-F(S)
MWISP G172.767−00.575	−8.41	0.670	8.83	0.85	3.45	0.566	0.235	0.177	0.510	44.93	25.02	Southern central	SC-F(S)
MWISP G172.358−00.300	−7.92	0.254	7.62	0.99	0.19	0.399	0.163	0.164	0.401	8.43	18.59	Southern central	⋯
MWISP G172.817−00.517	−7.42	0.534	8.96	0.85	2.72	0.634	0.265	0.178	0.553	44.95	25.49	Southern central	SC-F(S)
MWISP G172.875−00.450	−7.25	0.323	8.51	0.90	0.37	0.310	0.122	0.174	0.368	6.52	22.91	Southern central	SC-F(S)
MWISP G172.817−00.533	−7.58	0.323	8.12	0.89	0.63	0.374	0.151	0.170	0.394	9.44	21.57	Southern central	SC-F(S)
MWISP G172.750−00.592	−8.75	0.353	8.82	1.54	1.03	0.555	0.230	0.177	0.503	22.69	18.54	Southern central	SC-F(S)
MWISP G172.650−00.275	−9.58	0.156	6.54	1.92	0.37	0.546	0.228	0.152	0.475	9.73	10.59	Southern central	⋯
MWISP G172.717−00.583	−8.25	0.068	9.10	4.33	0.59	0.506	0.209	0.180	0.477	3.64	11.56	Southern central	SC-F(S)
MWISP G172.750−00.400	−9.24	0.571	10.00	0.55	2.15	0.475	0.194	0.188	0.469	26.92	37.46	Southern central	SC-F(N)
MWISP G172.417−00.383	−10.24	0.807	8.79	0.50	5.58	0.661	0.276	0.177	0.568	73.73	32.36	Southern central	SC-F(N)
MWISP G172.892−00.483	−7.25	0.156	7.24	0.50	0.50	0.181	0.062	0.160	0.298	1.07	24.16	Southern central	SC-F(S)
MWISP G172.350−00.517	−11.57	0.353	11.47	1.57	1.77	0.609	0.252	0.202	0.560	27.39	27.16	Southern central	SC-F(N)
MWISP G172.475−00.592	−7.75	0.454	6.93	0.57	0.85	0.462	0.191	0.157	0.428	20.21	21.25	Southern central	⋯
MWISP G172.750−00.383	−9.74	0.571	9.71	0.72	3.26	0.638	0.266	0.186	0.561	48.53	31.19	Southern central	SC-F(N)
MWISP G172.467−00.567	−8.25	0.068	5.31	2.20	0.08	0.271	0.108	0.137	0.303	1.04	7.22	Southern central	⋯
MWISP G172.258−00.333	−7.92	0.210	9.45	0.97	0.28	0.299	0.116	0.183	0.375	3.93	25.82	Southern central	⋯
MWISP G172.767−00.358	−8.25	0.624	8.32	0.35	5.68	0.757	0.318	0.172	0.626	74.77	35.44	Southern central	SC-F(N)
MWISP G172.550−00.700	−9.08	0.477	8.63	0.78	2.16	0.824	0.346	0.175	0.672	67.65	25.12	Southern central	⋯
MWISP G172.750−00.408	−8.58	0.454	9.64	0.36	1.23	0.299	0.116	0.185	0.378	8.47	43.79	Southern central	SC-F(N)
MWISP G172.717−00.392	−10.74	0.477	10.50	0.70	4.20	0.634	0.264	0.193	0.566	40.12	35.80	Southern central	SC-F(N)
MWISP G172.300−00.450	−9.08	0.497	9.16	0.39	1.20	0.394	0.159	0.180	0.416	16.10	38.95	Southern central	SC-F(N)
MWISP G172.750−00.367	−11.07	0.454	8.70	0.89	10.09	1.036	0.437	0.176	0.816	101.84	23.87	Southern central	SC-F(N)
MWISP G172.367−00.358	−8.08	0.068	8.15	1.98	0.22	0.254	0.097	0.170	0.339	0.92	14.50	Southern central	⋯
MWISP G170.658−00.242	−15.18	1.764	9.61	1.29	102.42	0.721	0.302	0.185	0.612	191.60	22.97	Western	W-F
MWISP G170.825+00.017	−17.67	1.363	10.95	0.95	60.33	0.734	0.307	0.197	0.631	153.61	32.66	Western	W-F
MWISP G170.658−00.250	−15.52	1.708	9.72	1.59	141.84	1.005	0.423	0.186	0.801	360.56	21.07	Western	W-F
MWISP G170.717−00.125	−15.52	1.694	10.44	1.50	130.23	1.151	0.486	0.192	0.905	469.25	24.17	Western	W-F
MWISP G170.733−00.108	−15.52	1.372	10.84	2.14	127.34	1.458	0.617	0.196	1.121	609.94	21.40	Western	W-F
MWISP G170.808+00.008	−16.84	1.355	11.91	1.08	71.54	0.873	0.366	0.206	0.727	216.23	34.71	Western	W-F
MWISP G170.625−00.292	−15.85	1.389	8.96	1.53	97.54	1.033	0.436	0.178	0.815	309.86	19.03	Western	W-F
MWISP G170.383−00.408	−14.52	0.945	9.32	1.32	15.89	0.842	0.354	0.182	0.689	140.15	21.67	Western	W-F
MWISP G170.667−00.250	−14.19	1.529	9.77	1.14	100.13	0.888	0.374	0.186	0.723	252.44	25.11	Western	W-F
MWISP G170.667−00.317	−14.19	1.100	9.85	1.77	53.64	1.069	0.451	0.187	0.846	263.13	20.39	Western	W-F
MWISP G170.683−00.192	−14.68	1.797	10.30	1.45	157.16	1.200	0.507	0.191	0.938	541.88	24.05	Western	W-F
MWISP G170.375−00.375	−15.02	0.867	9.78	1.96	17.94	0.777	0.326	0.186	0.650	109.55	19.13	Western	W-F
MWISP G170.650−00.350	−14.02	0.765	9.26	2.02	10.85	0.834	0.350	0.181	0.683	111.13	17.37	Western	W-F
MWISP G170.808+00.058	−18.50	1.077	9.99	1.26	44.86	0.907	0.381	0.188	0.737	185.23	24.68	Western	W-F
MWISP G170.333−00.350	−14.85	1.066	8.41	0.69	10.23	0.455	0.187	0.173	0.441	46.15	25.75	Western	W-F
MWISP G170.817+00.042	−18.67	1.055	11.03	1.36	32.28	0.709	0.296	0.198	0.616	110.89	27.52	Western	W-F
MWISP G170.650−00.342	−13.52	0.994	9.24	1.05	16.73	0.616	0.257	0.181	0.544	78.92	24.03	Western	W-F

Table 3
(Continued)

Clump	Velocity ($km\ s^{-1}$)	Radius (pc)	T_{ex} (K)	n_{H_2} ($10^2\ cm^{-3}$)	$M_{LTE,c}$ ($M_\odot$)	Δv ($km\ s^{-1}$)	σ_{NT} ($km\ s^{-1}$)	c_s ($km\ s^{-1}$)	σ_{3D} ($km\ s^{-1}$)	$M_{Vir,c}$ ($M_\odot$)	$M_{Jeans,c}$ ($M_\odot$)	Region	Filament
(1)	(2)	(3)	(4)	(5)	(6)	(7)	(8)	(9)	(10)	(11)	(12)	(13)	(14)
MWISP G170.725−00.250	−15.02	1.473	9.11	0.94	49.68	0.981	0.414	0.180	0.781	296.76	24.92	Western	W-F
MWISP G170.333−00.350	−15.35	1.120	8.56	0.80	13.70	0.609	0.254	0.174	0.534	87.02	24.59	Western	W-F
MWISP G170.783−00.042	−15.52	1.327	11.12	1.09	46.06	1.385	0.585	0.199	1.071	532.21	31.10	Western	W-F
MWISP G170.392−00.350	−15.02	1.100	9.15	0.96	18.45	0.583	0.242	0.180	0.523	78.17	24.79	Western	W-F
MWISP G170.583−00.308	−16.01	0.945	7.64	1.57	25.28	0.956	0.403	0.165	0.755	180.90	14.79	Western	W-F
MWISP G170.458−00.333	−15.68	1.174	9.21	0.93	23.73	0.780	0.327	0.181	0.648	149.57	25.43	Western	W-F
MWISP G170.475−00.375	−15.18	0.994	8.54	0.68	7.66	0.649	0.271	0.174	0.558	87.66	26.56	Western	W-F
MWISP G170.900−00.033	−15.68	0.971	9.94	0.62	5.33	0.614	0.255	0.188	0.549	76.70	35.02	Western	⋯
MWISP G170.100−00.367	−15.02	0.893	8.66	0.90	7.23	0.558	0.232	0.175	0.503	58.16	23.56	Western	⋯
MWISP G171.100−00.042	−14.52	0.960	7.89	0.49	2.74	0.550	0.229	0.167	0.491	60.65	27.85	Western	⋯
MWISP G170.508−00.333	−16.01	0.867	8.81	1.20	16.54	0.772	0.324	0.177	0.639	108.15	20.95	Western	W-F
MWISP G170.525−00.333	−16.01	0.584	8.47	2.12	10.04	0.799	0.336	0.173	0.654	77.86	14.87	Western	W-F
MWISP G170.708+00.083	−17.34	1.143	7.55	0.48	7.91	0.575	0.240	0.164	0.502	78.92	26.23	Western	W-F
MWISP G170.408−00.375	−14.02	1.152	9.25	1.01	32.50	0.935	0.394	0.181	0.751	210.51	24.49	Western	W-F
MWISP G170.408−00.342	−15.52	1.120	8.87	0.85	21.80	0.706	0.295	0.177	0.597	116.70	25.09	Western	W-F
MWISP G170.183−00.358	−15.52	0.543	9.29	1.21	3.02	0.553	0.229	0.182	0.506	34.72	22.59	Western	⋯
MWISP G170.517−00.233	−14.85	0.919	8.33	0.69	8.26	0.762	0.320	0.172	0.629	111.71	25.46	Western	W-F
MWISP G170.200−00.367	−15.52	0.794	9.42	0.78	6.00	0.558	0.231	0.183	0.510	51.70	28.72	Western	⋯
MWISP G170.783+00.125	−18.17	0.794	6.92	0.37	2.74	0.516	0.215	0.157	0.460	44.29	26.41	Western	W-F
MWISP G170.342−00.383	−15.18	0.794	9.37	1.40	11.74	0.714	0.299	0.182	0.606	84.67	21.26	Western	W-F
MWISP G170.292−00.400	−14.85	0.882	9.59	0.86	7.49	0.560	0.232	0.184	0.513	57.75	28.08	Western	W-F
MWISP G170.258−00.325	−14.68	0.809	8.68	0.65	5.80	0.714	0.299	0.176	0.601	86.25	27.80	Western	⋯
MWISP G170.550−00.325	−15.85	0.809	8.40	1.39	19.11	0.868	0.366	0.173	0.700	127.59	18.13	Western	W-F
MWISP G170.625−00.333	−14.19	0.994	9.70	1.57	28.33	0.943	0.397	0.185	0.759	184.99	21.10	Western	W-F
MWISP G170.617−00.383	−17.84	0.353	7.50	2.14	1.37	0.619	0.259	0.163	0.530	28.35	12.33	Western	W-F
MWISP G170.117−00.350	−15.35	0.645	8.50	1.18	3.25	0.694	0.291	0.174	0.586	64.98	19.98	Western	⋯
MWISP G170.308−00.392	−15.02	0.696	9.70	1.47	5.41	0.741	0.310	0.186	0.626	79.85	21.86	Western	W-F
MWISP G170.067−00.358	−15.68	0.945	7.35	0.43	4.48	0.553	0.230	0.161	0.487	60.46	26.52	Western	⋯
MWISP G170.192−00.325	−14.52	0.645	9.14	0.77	2.61	0.505	0.208	0.180	0.477	34.37	27.69	Western	⋯
MWISP G170.842+00.058	−16.35	0.732	10.04	1.08	7.16	0.662	0.276	0.189	0.579	67.21	26.83	Western	W-F
MWISP G170.942−00.050	−15.02	0.747	9.65	0.75	1.95	0.633	0.263	0.185	0.558	62.52	30.40	Western	⋯
MWISP G170.700+00.083	−16.68	0.893	6.99	0.44	3.81	0.463	0.192	0.157	0.430	40.10	24.52	Western	W-F
MWISP G170.167−00.342	−15.68	0.663	8.64	0.68	2.02	0.369	0.148	0.175	0.398	18.85	27.02	Western	⋯
MWISP G170.842+00.058	−16.68	0.853	9.98	0.64	10.83	0.523	0.216	0.188	0.496	48.80	34.53	Western	W-F
MWISP G170.158−00.342	−15.35	0.809	9.01	0.67	4.69	0.515	0.213	0.179	0.481	44.83	28.91	Western	⋯
MWISP G170.867+00.008	−16.35	0.584	9.18	1.11	3.96	0.641	0.267	0.180	0.559	50.14	23.13	Western	⋯
MWISP G170.117−00.375	−15.35	0.714	8.92	1.41	4.83	0.669	0.280	0.178	0.574	66.89	19.69	Western	⋯
MWISP G171.058−00.108	−15.52	0.823	8.80	0.52	3.70	0.563	0.234	0.177	0.507	54.57	31.64	Western	⋯
MWISP G170.525−00.350	−14.52	0.823	9.63	0.69	11.60	0.692	0.289	0.185	0.595	82.57	31.46	Western	W-F
MWISP G170.125−00.392	−15.02	0.696	9.09	0.90	2.89	0.448	0.183	0.180	0.445	29.26	25.36	Western	⋯
MWISP G170.208−00.325	−14.68	0.645	8.92	0.96	2.96	0.621	0.259	0.178	0.544	52.02	23.77	Western	⋯
MWISP G170.858−00.017	−15.85	0.584	9.77	0.84	2.91	0.530	0.219	0.186	0.497	34.25	29.20	Western	W-F
MWISP G170.783+00.100	−17.34	0.908	8.91	0.61	7.30	0.628	0.262	0.178	0.548	74.81	29.82	Western	W-F
MWISP G170.192−00.308	−14.35	0.565	8.19	0.76	1.64	0.457	0.188	0.170	0.439	24.65	23.64	Western	⋯
MWISP G170.850+00.008	−16.18	0.823	10.60	0.90	18.75	0.659	0.274	0.194	0.582	74.84	31.95	Western	W-F
MWISP G170.150−00.392	−15.52	0.747	8.71	0.88	2.72	0.485	0.200	0.176	0.461	36.72	24.08	Western	⋯

Table 3
(Continued)

Clump	Velocity ($km\ s^{-1}$)	Radius (pc)	T_{ex} (K)	n_{H_2} ($10^2\ cm^{-3}$)	$M_{LTE,c}$ ($M_\odot$)	Δv ($km\ s^{-1}$)	σ_{NT} ($km\ s^{-1}$)	c_s ($km\ s^{-1}$)	σ_{3D} ($km\ s^{-1}$)	$M_{Vir,c}$ ($M_\odot$)	$M_{Jeans,c}$ ($M_\odot$)	Region	Filament
(1)	(2)	(3)	(4)	(5)	(6)	(7)	(8)	(9)	(10)	(11)	(12)	(13)	(14)
MWISP G170.550−00.300	−14.52	0.823	9.41	0.80	16.90	0.853	0.359	0.183	0.697	125.45	28.33	Western	W-F
MWISP G170.800+00.083	−17.18	0.960	9.58	0.81	13.44	0.802	0.337	0.184	0.665	129.15	28.87	Western	W-F
MWISP G170.592−00.250	−15.85	1.282	7.78	0.85	23.26	0.907	0.382	0.166	0.722	220.39	20.67	Western	W-F
MWISP G170.750+00.067	−18.01	1.214	9.44	0.84	24.61	0.878	0.369	0.183	0.714	195.91	27.81	Western	W-F
MWISP G170.575+00.100	−15.85	0.443	9.03	1.18	0.61	0.573	0.238	0.179	0.516	30.41	21.92	Western	⋯
MWISP G170.842−00.025	−15.85	0.893	10.12	0.65	9.12	0.624	0.260	0.190	0.557	72.83	35.09	Western	W-F
MWISP G170.642−00.308	−13.52	1.163	10.06	1.11	54.71	0.852	0.358	0.189	0.701	176.48	26.50	Western	W-F
MWISP G170.342−00.417	−14.85	0.809	9.20	0.97	8.75	0.749	0.314	0.181	0.627	94.88	24.86	Western	W-F
MWISP G170.875+00.033	−16.18	0.732	10.35	1.00	3.55	0.653	0.272	0.192	0.576	65.20	29.16	Western	W-F
MWISP G170.283−00.417	−15.02	0.623	8.60	0.97	2.90	0.506	0.209	0.175	0.472	33.45	22.49	Western	W-F
MWISP G171.083−00.075	−14.52	0.565	8.29	0.64	1.11	0.403	0.164	0.171	0.411	19.24	26.11	Western	⋯
MWISP G170.258−00.417	−14.85	0.623	9.24	0.83	2.62	0.506	0.209	0.181	0.479	33.45	27.00	Western	W-F
MWISP G170.708−00.150	−16.35	1.764	9.90	0.49	79.54	0.638	0.266	0.187	0.563	150.00	39.14	Western	W-F
MWISP G170.175−00.392	−15.52	0.495	8.62	0.86	1.68	0.372	0.150	0.175	0.399	14.34	23.95	Western	⋯
MWISP G170.225−00.367	−14.85	0.919	9.73	0.59	6.29	0.533	0.220	0.186	0.499	54.63	34.60	Western	⋯
MWISP G170.592−00.367	−14.02	0.714	8.41	0.63	3.36	0.518	0.214	0.173	0.477	40.09	26.91	Western	W-F
MWISP G170.717+00.000	−16.35	0.696	9.07	0.76	3.31	0.716	0.300	0.179	0.605	74.57	27.45	Western	W-F
MWISP G170.167−00.400	−15.85	0.521	8.11	0.64	1.65	0.370	0.150	0.170	0.392	14.94	25.39	Western	⋯
MWISP G170.192−00.392	−15.02	0.645	8.75	0.56	1.48	0.394	0.159	0.176	0.412	20.89	30.24	Western	⋯
MWISP G170.158−00.392	−15.02	0.416	9.33	1.09	0.83	0.362	0.145	0.182	0.403	11.41	23.90	Western	⋯
MWISP G170.092−00.417	−15.18	0.696	8.66	0.74	2.03	0.571	0.237	0.175	0.511	47.50	26.07	Western	⋯
MWISP G170.242−00.417	−14.85	0.521	9.33	0.86	1.85	0.475	0.195	0.182	0.462	24.57	26.93	Western	W-F
MWISP G170.550−00.225	−14.35	0.747	7.79	0.68	3.77	0.785	0.330	0.166	0.640	96.36	23.15	Western	W-F
MWISP G170.500−00.275	−16.01	0.645	7.19	0.58	2.85	0.475	0.197	0.160	0.439	30.42	22.15	Western	W-F
MWISP G170.517−00.283	−15.52	0.908	7.83	0.53	8.11	0.558	0.232	0.167	0.495	59.11	26.38	Western	W-F
MWISP G170.325−00.425	−15.02	0.469	8.60	0.91	2.40	0.570	0.237	0.175	0.510	31.85	23.19	Western	W-F
MWISP G170.567−00.350	−14.68	0.696	9.43	0.83	4.50	0.619	0.258	0.183	0.548	55.85	27.85	Western	W-F
MWISP G170.767−00.258	−15.18	0.747	8.21	0.63	2.38	0.676	0.283	0.171	0.572	71.35	26.05	Western	⋯
MWISP G170.583−00.258	−16.18	0.714	7.20	0.58	2.42	0.375	0.153	0.160	0.383	21.04	22.29	Western	W-F
MWISP G170.750+00.033	−16.84	1.009	9.76	0.62	10.14	0.573	0.237	0.186	0.523	69.24	34.04	Western	W-F
MWISP G170.608−00.350	−14.52	0.794	8.94	1.05	14.24	0.726	0.304	0.178	0.610	87.45	22.89	Western	W-F
MWISP G170.608−00.258	−17.01	1.174	7.76	0.31	27.45	0.649	0.272	0.166	0.551	103.51	33.82	Western	W-F
MWISP G170.467−00.342	−14.68	0.971	9.42	0.55	10.33	0.482	0.198	0.183	0.466	47.12	34.11	Western	W-F
MWISP G170.750+00.008	−16.68	0.809	9.50	0.56	6.39	0.496	0.204	0.184	0.476	41.70	34.28	Western	W-F
MWISP G170.475−00.342	−14.35	0.732	9.50	0.66	5.84	0.506	0.209	0.184	0.481	39.27	31.59	Western	W-F
MWISP G170.108−00.400	−14.68	0.765	9.17	0.59	2.56	0.433	0.177	0.180	0.437	30.04	31.76	Western	⋯
MWISP G170.600−00.333	−14.68	0.994	9.45	0.99	18.98	0.750	0.314	0.183	0.630	117.15	25.65	Western	W-F
MWISP G170.717−00.108	−17.18	0.765	9.68	0.66	17.17	0.661	0.276	0.185	0.575	69.85	32.52	Western	W-F
MWISP G170.550−00.333	−14.85	0.853	9.69	0.69	10.60	0.515	0.212	0.185	0.488	47.26	31.93	Western	W-F
MWISP G170.250−00.383	−15.35	0.838	9.56	0.60	5.89	0.535	0.221	0.184	0.498	50.10	33.47	Western	W-F
MWISP G170.742−00.225	−13.52	0.945	8.24	0.29	14.18	0.717	0.301	0.171	0.599	101.75	38.40	Western	W-F
MWISP G171.067−00.092	−14.85	0.696	8.89	0.46	1.35	0.357	0.143	0.178	0.395	18.56	34.10	Western	⋯
MWISP G170.783−00.217	−14.85	1.163	8.95	0.49	13.21	0.807	0.339	0.178	0.663	158.40	33.58	Western	⋯
MWISP G171.033−00.158	−15.85	0.443	7.72	0.78	0.08	0.317	0.126	0.165	0.360	9.32	21.29	Western	⋯
MWISP G170.333+00.058	−19.17	0.765	6.83	0.61	1.39	0.648	0.271	0.156	0.542	67.07	20.08	Western	⋯
MWISP G170.550+00.092	−15.52	0.385	8.09	0.79	0.22	0.319	0.127	0.169	0.366	8.19	22.66	Western	⋯

Table 3
(Continued)

Clump	Velocity ($km\ s^{-1}$)	Radius (pc)	T_{ex} (K)	n_{H_2} ($10^2\ cm^{-3}$)	$M_{LTE,c}$ ($M_\odot$)	Δv ($km\ s^{-1}$)	σ_{NT} ($km\ s^{-1}$)	c_s ($km\ s^{-1}$)	σ_{3D} ($km\ s^{-1}$)	$M_{Vir,c}$ ($M_\odot$)	$M_{Jeans,c}$ ($M_\odot$)	Region	Filament
(1)	(2)	(3)	(4)	(5)	(6)	(7)	(8)	(9)	(10)	(11)	(12)	(13)	(14)
MWISP G170.517−00.267	−16.68	0.277	6.17	0.91	1.01	0.382	0.157	0.148	0.373	8.45	14.11	Western	W-F
MWISP G170.533−00.275	−13.36	0.495	9.03	0.62	3.55	0.508	0.210	0.179	0.478	26.76	30.14	Western	W-F
MWISP G170.775−00.217	−15.85	1.109	9.19	0.34	7.09	0.578	0.240	0.181	0.520	77.43	42.09	Western	⋯
MWISP G170.308+00.075	−19.33	0.681	6.84	0.51	1.03	0.422	0.174	0.156	0.404	25.34	22.03	Western	⋯
MWISP G171.067−00.067	−14.68	0.277	8.03	0.91	0.23	0.281	0.109	0.169	0.348	4.56	20.85	Western	⋯
MWISP G170.733+00.058	−16.35	0.779	8.12	0.37	4.50	0.475	0.196	0.170	0.449	36.77	33.37	Western	W-F
MWISP G170.558−00.300	−13.36	0.794	9.23	0.37	9.98	0.575	0.239	0.181	0.519	54.82	40.33	Western	W-F
MWISP G170.292−00.425	−15.35	0.521	6.88	0.51	2.25	0.395	0.162	0.156	0.390	17.02	22.07	Western	W-F
MWISP G170.725−00.033	−16.01	0.747	8.94	0.55	1.48	0.880	0.370	0.178	0.712	120.99	31.72	Western	W-F
MWISP G170.492−00.342	−13.69	0.443	9.42	0.68	3.53	0.480	0.197	0.183	0.466	21.34	30.84	Western	W-F
MWISP G169.983−00.342	−15.18	0.277	7.15	0.76	0.15	0.330	0.133	0.159	0.359	6.33	19.24	Western	⋯
MWISP G171.042−00.142	−15.68	0.443	8.34	0.63	0.27	0.374	0.151	0.172	0.396	12.93	26.63	Western	⋯
MWISP G170.767+00.008	−15.85	0.908	10.07	0.42	6.30	0.506	0.208	0.189	0.487	48.70	43.38	Western	W-F
MWISP G170.508−00.325	−13.52	0.277	9.66	0.79	2.49	0.297	0.115	0.185	0.377	5.12	29.60	Western	W-F
MWISP G170.683−00.192	−17.01	1.202	9.16	0.35	21.12	0.729	0.305	0.180	0.614	133.64	41.07	Western	W-F
MWISP G170.758+00.017	−17.34	0.765	9.41	0.82	5.51	0.646	0.269	0.183	0.564	66.73	27.96	Western	W-F
MWISP G170.542−00.275	−15.85	0.623	6.86	0.55	4.39	0.540	0.225	0.156	0.474	37.98	21.33	Western	W-F
MWISP G170.483−00.275	−16.35	0.443	6.74	0.80	0.86	0.445	0.184	0.155	0.416	18.35	17.12	Western	W-F
MWISP G170.800−00.225	−15.35	0.443	9.33	0.54	0.42	0.410	0.166	0.182	0.427	15.59	33.89	Western	⋯
MWISP G170.483−00.242	−17.18	0.074	6.43	2.24	0.46	0.269	0.106	0.151	0.320	1.12	9.55	Western	W-F
MWISP G170.492−00.225	−14.19	0.385	8.23	0.52	0.29	0.332	0.132	0.171	0.374	8.89	28.77	Western	W-F
MWISP G170.750−00.217	−14.02	1.055	8.53	0.35	6.35	0.591	0.246	0.174	0.522	77.08	37.12	Western	W-F
MWISP G170.492−00.258	−16.68	0.277	5.85	0.43	1.11	0.191	0.070	0.144	0.278	2.11	18.84	Western	W-F
MWISP G170.142−00.392	−14.52	0.416	7.53	0.32	0.47	0.262	0.101	0.163	0.333	5.99	31.93	Western	⋯
MWISP G170.492−00.267	−17.18	0.170	5.69	1.61	0.49	0.412	0.170	0.142	0.384	6.04	9.38	Western	W-F
MWISP G170.550−00.250	−13.19	0.230	8.43	1.02	0.76	0.422	0.172	0.173	0.423	8.55	21.21	Western	W-F
MWISP G170.267−00.400	−14.19	0.416	9.53	0.49	1.06	0.339	0.134	0.184	0.394	9.99	36.98	Western	W-F
MWISP G170.733+00.125	−17.84	0.565	7.77	0.46	0.81	0.486	0.201	0.166	0.452	27.98	27.93	Western	W-F
MWISP G170.450−00.275	−15.68	0.565	7.16	0.43	1.00	0.543	0.226	0.159	0.479	34.85	25.51	Western	W-F
MWISP G170.258−00.383	−15.68	0.416	9.13	0.65	1.23	0.359	0.144	0.180	0.399	11.20	30.05	Western	W-F
MWISP G170.767−00.250	−14.35	0.495	6.91	0.27	1.25	0.294	0.117	0.157	0.338	8.95	30.44	Western	⋯
MWISP G170.675+00.083	−17.84	0.320	6.27	0.54	0.11	0.516	0.215	0.149	0.453	17.85	18.73	Western	W-F
MWISP G170.417−00.283	−16.18	0.663	7.10	0.31	0.73	0.468	0.194	0.159	0.434	30.41	29.75	Western	W-F
MWISP G170.067−00.433	−14.85	0.277	7.80	0.86	0.14	0.515	0.213	0.166	0.469	15.36	20.64	Western	⋯
MWISP G170.742−00.008	−15.85	0.543	9.79	0.54	2.48	0.428	0.174	0.186	0.442	20.84	36.59	Western	W-F
MWISP G170.517−00.317	−14.19	0.565	10.00	0.73	5.07	0.648	0.270	0.188	0.570	49.57	32.34	Western	W-F
MWISP G170.725−00.075	−16.68	0.681	9.00	0.44	9.83	0.511	0.211	0.179	0.479	37.27	35.79	Western	W-F
MWISP G170.525−00.242	−13.52	0.277	8.46	0.73	1.45	0.457	0.188	0.173	0.442	12.09	25.31	Western	W-F
MWISP G170.450−00.317	−16.84	0.521	7.19	0.20	3.42	0.334	0.134	0.160	0.361	12.14	37.79	Western	W-F
MWISP G170.717−00.025	−14.68	0.882	7.74	0.29	2.01	1.122	0.474	0.166	0.870	232.38	34.84	Western	W-F

Note. Properties of identified clumps. Column 1 is the clump name, which contains the Galactic longitude and latitude. Columns 2–6 are the rest velocity, clump radius, excitation temperature, H_2 volume density, and LTE mass. Columns 7–12 are the line width, nonthermal velocity dispersion, isothermal sound speed, 3D velocity dispersion, virial mass, and Jeans mass. Columns 14 and 15 are the region and filament where the clump is located.

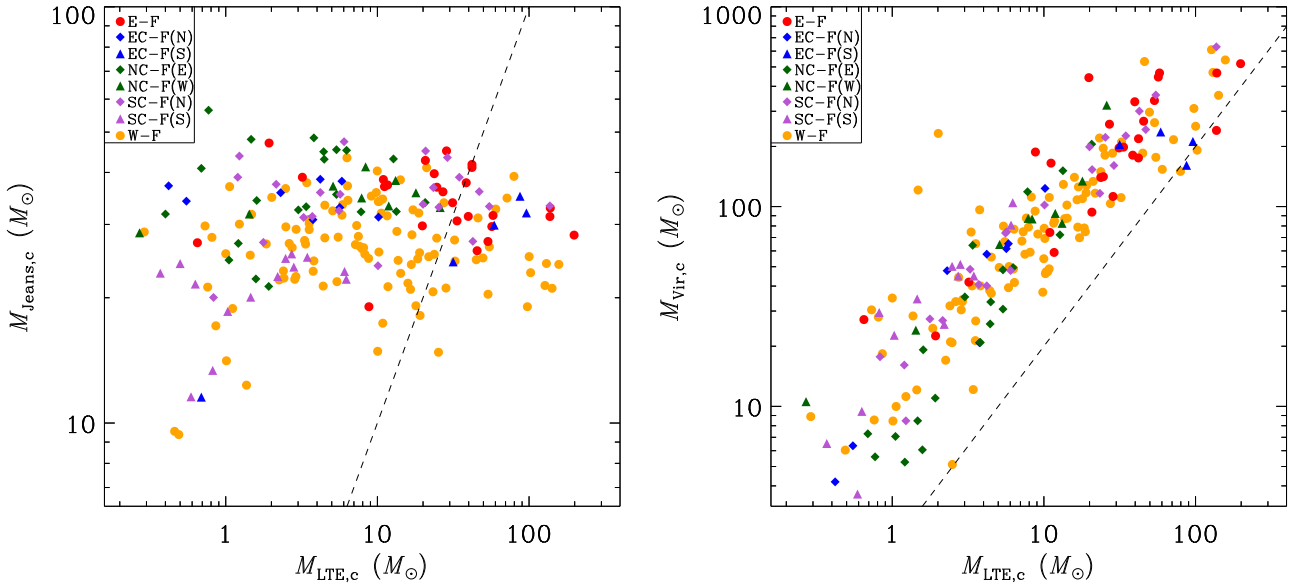

Figure 20. Left panel: relationship between the Jeans mass ($M_{\rm Jeans,c}$) and the LTE mass ($M_{\rm LTE,c}$) of the clumps located on the filaments. Different shapes and colors represent the clumps located on different filaments, which are marked in the top right corner of the plot. The dashed black line indicates the position where Jeans mass equals LTE mass. Right panel: relationship between the virial mass ($M_{\rm Vir,c}$) and the LTE mass ($M_{\rm LTE,c}$) of the clumps located on the filaments. The dashed black line indicates the position where the virial parameter equals 2.

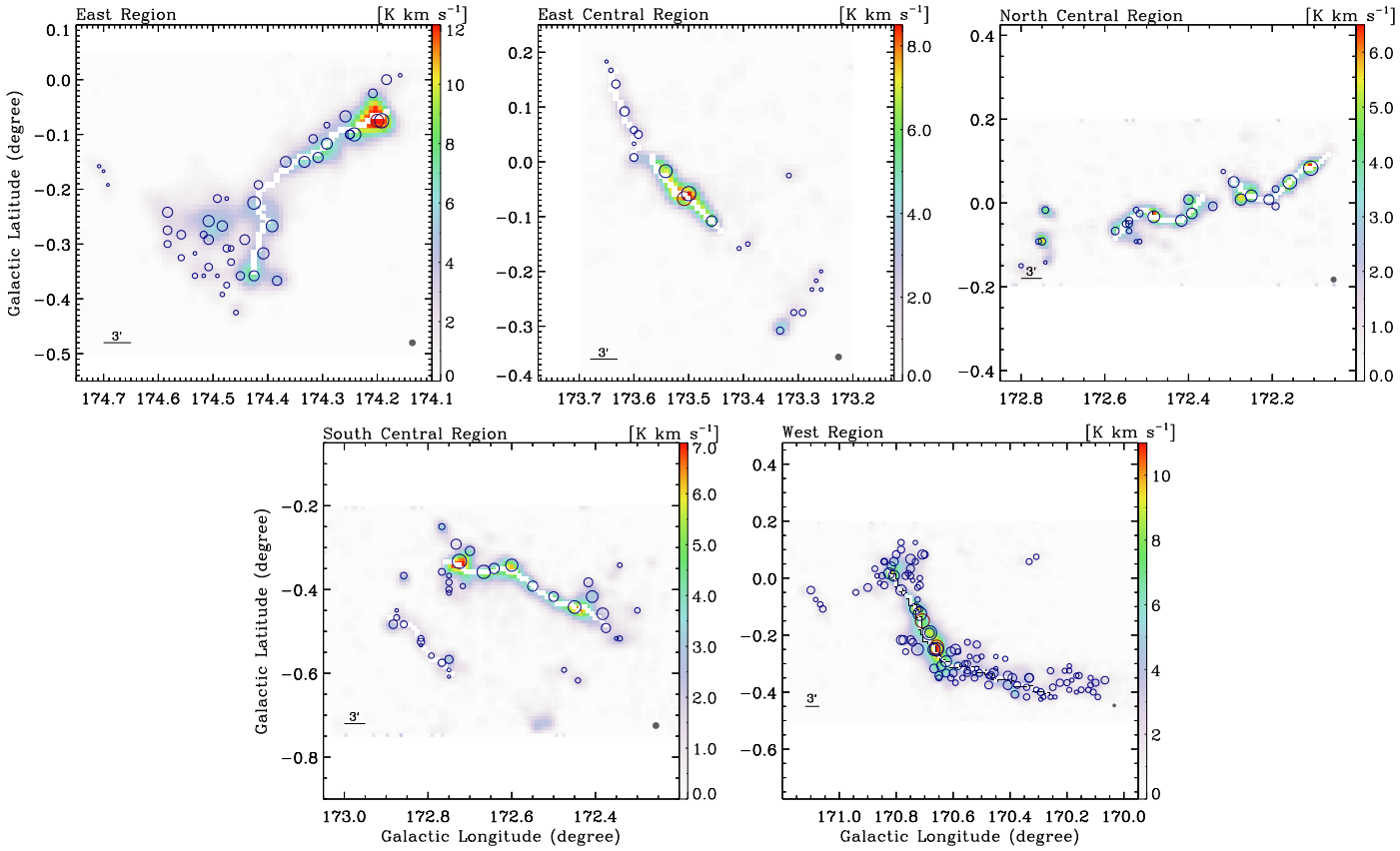

Figure 21. The CO clumps identified in each region. The circles indicate the positions of the clumps. The sizes of the circles are scaled according to the sizes of the clumps. The red circles indicate the virialized clumps, while the blue circles indicate the unvirialized clumps. The solid white lines show the positions of filaments. The backgrounds are the ^{13}CO integrated intensity maps of each region.

emission intensities are greater than three times the rms noise and the corresponding ^{13}CO emission intensities are smaller than three times the rms noise. Note that we also manually adjust the ranges of line wings based on the ^{12}CO *PV* maps.

In Figure 25, we present the CO outflows overlaid on the ^{13}CO integrated intensity maps. The outflow images are obtained by integrating the ^{12}CO emission over the velocity ranges of the line wings, and the contours are overlaid from 3σ at intervals of 1.5σ (σ is the rms noise level of the outflow

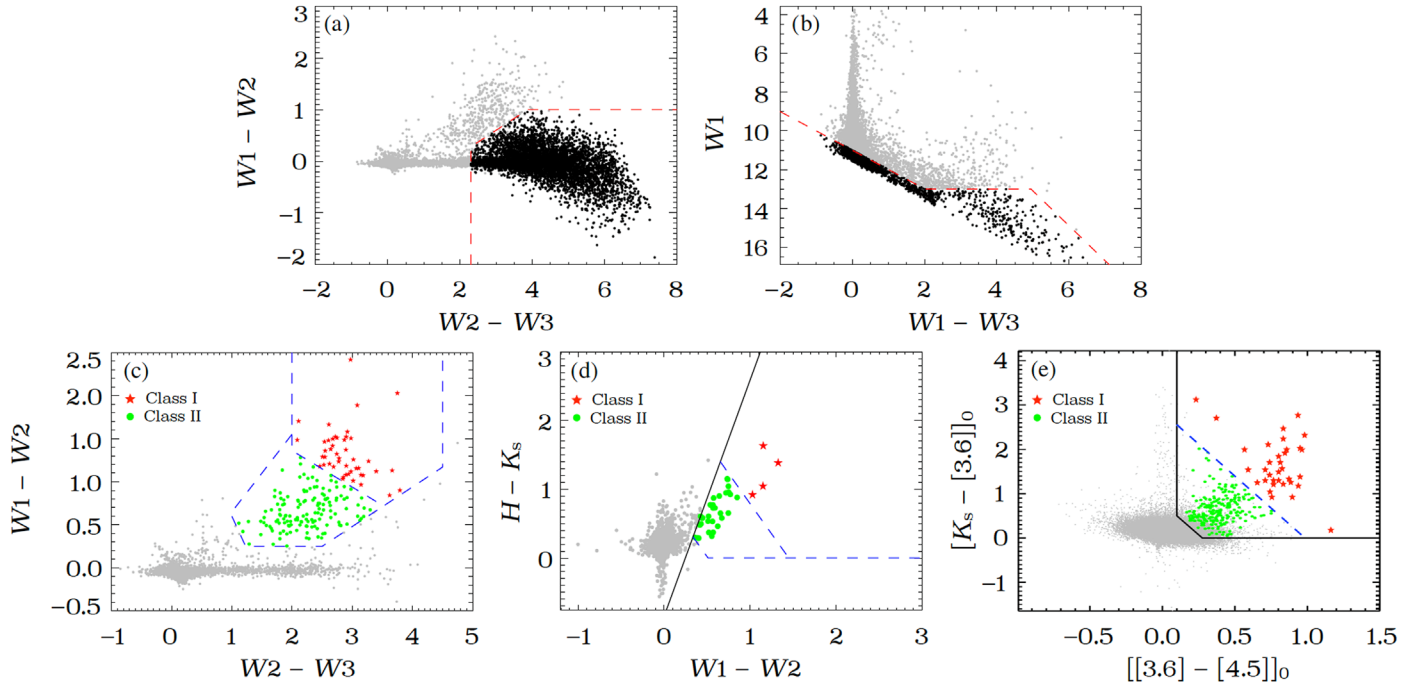

Figure 22. Top panels: color–color diagrams used to remove the star-forming galaxies and AGNs. The dashed red lines indicate the criteria used in Koenig & Leisawitz (2014). The black points represent the sources that have been excluded, and the gray points represent the sources that have been selected for further classification. Bottom panels: classification of YSO candidates in the $W1 - W2$ vs. $W2 - W3$ color–color diagram (panel (c)), $H - K_s$ vs. $W1 - W2$ color–color diagram (panel (d)), and $K_s - [3.6]$ vs. $[3.6] - [4.5]$ color–color diagram (panel (e)). The solid black and dashed blue lines represent the classification criteria used in Koenig & Leisawitz (2014; panels (c) and (d)) and Gutermuth et al. (2009; panel (e)). The gray points represent the sources that have been excluded.

images). Under LTE conditions and assuming optically thin ^{12}CO emission in the line wings, the ^{12}CO column density of the outflow lobe can be given by (Scoville et al. 1986; Garden et al. 1991)

$$N_{^{12}\mathrm{CO}} = 2.40 \times 10^{14} \cdot \frac{\int T_{\mathrm{MB},\,^{12}\mathrm{CO}}\, dv}{1 - e^{-5.53/T_{\mathrm{ex}}}}, \quad (8)$$

where $\int T_{\mathrm{MB},\,^{12}\mathrm{CO}}\, dv$ is the integrated intensity of the outflow lobe. To derive the H_2 column density ($N_{\mathrm{H_2,blue/red}}$), we multiply the column density by the abundance $[H_2]/[^{12}\mathrm{CO}]$ with a value of 10^4 (Blake et al. 1987). The mass of the outflow lobe can be calculated by Equation (4),

$$M_{\mathrm{bule/red}} = \mu m_{\mathrm{H}} \int N_{\mathrm{H_2,blue/red}}\, dS_{\mathrm{blue/red}}, \quad (9)$$

where $S_{\mathrm{blue/red}}$ is the emission area of the blue or red lobe. The momentum and energy of the outflow are then given by

$$P_{\mathrm{out}} = P_{\mathrm{blue}} + P_{\mathrm{red}} = M_{\mathrm{bule}}\, v_{\mathrm{bule}} + M_{\mathrm{red}}\, v_{\mathrm{red}}, \quad (10)$$

$$E_{\mathrm{out}} = E_{\mathrm{blue}} + E_{\mathrm{red}} = \frac{1}{2} M_{\mathrm{bule}}\, v_{\mathrm{bule}}^2 + \frac{1}{2} M_{\mathrm{red}}\, v_{\mathrm{red}}^2, \quad (11)$$

where $v_{\mathrm{blue/red}}$ is the maximum velocity of the blue or red line wing. The results of these parameters are listed in Table 5. The typical mass, momentum, and energy of the outflows are 1.42 $M_\odot$, 18.72 $M_\odot$ km s^{-1}, and 1.65 $\times$ 10^{45} erg, respectively. Compared to the work of Li et al. (2016), which also uses the CO data from the MWISP project to identify molecular outflows within the Galactic plane, our sample of outflows has lower mass and energy. However, as suggested by Richer et al. (2000) and Arce et al. (2007), low-mass outflows also play an important role in the dissipation of excess angular momentum and mass accretion toward the central star during the star-forming process.

In the bottom panels of Figure 25, we overlay YSOs identified in the last section on the maps of outflow contours. For E-F_OF, W-F_OF1, and W-F_OF3, there are several Class II objects located between the peaks of the red and blue lobes. We note that the IR data used in this work may not be able to reveal deeply embedded YSOs such as Class 0 objects, and Class II objects are typically too evolved to power the molecular outflows in CO (Bachiller & Tafalla 1999; Arce et al. 2007). Further high-resolution observations of the dust continuum are needed to identify the driving sources of these outflows. However, the detection of CO outflows indicates ongoing star-forming activity within E-F and W-F.

5. Summary

We present large-field mapping observations of the G172 region covering an area with $169.^\circ75 \leqslant l \leqslant 174.^\circ75$ and $-0.^\circ75 \leqslant b \leqslant 0.^\circ5$ in the $J = 1 - 0$ transition of the CO isotopologues (^{12}CO, ^{13}CO, and C^{18}O) using the PMO 13.7 m telescope. We identify five main subregions of molecular clouds in the velocity range between -25 and 8 km s^{-1} that are characterized by conspicuous filamentary structures. The main results are summarized below.

According to the ^{13}CO emission data of the five subregions, we have identified a total of eight filaments: E-F, EC-F(N), EC-F(S), NC-F(E), NC-F(W), SC-F(N), SC-F(S), and W-F. Four of these filaments (E-F, EC-F(S), SC-F(N), and W-F) are also revealed in the C^{18}O emission. We extract velocity structures along the length of each filament. In the ^{13}CO *PV* maps, most filaments present continuous velocity structures with slight velocity gradients. In the C^{18}O *PV* maps, the velocity structures

Table 4
IR Photometric Magnitudes of YSO Candidates

ID	J(1.25 μm) (mag)	H(1.65 μm) (mag)	K_s(2.17 μm) (mag)	$W1$(3.4 μm) (mag)	$W2$(4.6 μm) (mag)	$W3$(12 μm) (mag)	$W4$(22 μm) (mag)	[3.6] (mag)	[4.5] (mag)	Class	Region
(1)	(2)	(3)	(4)	(5)	(6)	(7)	(8)	(9)	(10)	(11)	(12)
J052946.87+333816.6	18.031 ± 0.040	17.557 ± 0.044	16.572 ± 0.038	14.629 ± 0.037	14.629 ± 0.036	14.629 ± 0.098	14.629 ± 0.213	14.540 ± 0.042	13.581 ± 0.041	I	Eastern
SSTGLMCG174.2086 −00.0741	18.090 ± 0.016	16.480 ± 0.018	15.560 ± 0.015	⋯	⋯	⋯	⋯	14.680 ± 0.057	14.259 ± 0.076	II	Eastern
J053035.04+334408.6	16.114 ± 0.009	15.184 ± 0.006	14.825 ± 0.008	14.314 ± 0.030	14.314 ± 0.044	14.314	14.314	14.234 ± 0.043	13.990 ± 0.043	II	Eastern
J053050.85+332735.1	17.645 ± 0.014	16.167 ± 0.013	15.373 ± 0.013	14.674 ± 0.034	14.674 ± 0.043	14.674 ± 0.233	14.674	14.368 ± 0.053	13.796 ± 0.035	II	Eastern
J053047.75+332740.1	14.858 ± 0.003	13.865 ± 0.002	13.361 ± 0.003	12.540 ± 0.031	12.540 ± 0.024	12.540 ± 0.035	12.540 ± 0.097	12.336 ± 0.037	11.570 ± 0.029	II	Eastern
SSTGLMCG174.2067 −00.0695	16.178 ± 0.008	15.231 ± 0.006	14.744 ± 0.007	⋯	⋯	⋯	⋯	14.282 ± 0.039	13.912 ± 0.042	II	Eastern
J053047.05+334842.9	17.324 ± 0.010	15.845 ± 0.010	14.983 ± 0.009	13.948 ± 0.030	13.948 ± 0.033	13.948 ± 0.109	13.948 ± 0.032	14.171 ± 0.038	13.772 ± 0.037	II	Eastern
J053047.97+334709.8	15.189 ± 0.004	14.227 ± 0.003	13.744 ± 0.003	13.155 ± 0.024	13.155 ± 0.026	13.155 ± 0.064	13.155 ± 0.032	13.089 ± 0.048	12.870 ± 0.038	II	Eastern
J053051.64+334842.5	17.626 ± 0.017	16.319 ± 0.015	15.639 ± 0.016	15.038 ± 0.040	15.038 ± 0.055	15.038	15.038 ± 0.061	14.779 ± 0.052	14.361 ± 0.049	II	Eastern
J053011.77+332558.8	⋯	15.067 ± 0.005	14.565 ± 0.010	13.372 ± 0.032	13.372 ± 0.036	13.372 ± 0.097	13.372 ± 0.084	13.293 ± 0.037	12.999 ± 0.032	II	Eastern
J052952.49+333433.2	⋯	15.016 ± 0.005	14.222 ± 0.007	13.293 ± 0.026	13.293 ± 0.028	13.293 ± 0.078	13.293 ± 0.262	13.034 ± 0.036	12.549 ± 0.031	II	Eastern
J053009.55+332520.0	12.947 ± 0.024	12.268 ± 0.023	11.631 ± 0.021	10.742 ± 0.025	10.145 ± 0.022	6.955 ± 0.022	5.099 ± 0.047	10.593 ± 0.047	10.134 ± 0.029	II	Eastern
J053057.48+332535.9	15.314 ± 0.003	14.223 ± 0.003	13.336 ± 0.003	11.242 ± 0.022	10.415 ± 0.021	8.486 ± 0.027	6.412 ± 0.081	⋯	⋯	II	Eastern
J053059.07+332642.9	15.294 ± 0.003	14.183 ± 0.002	13.585 ± 0.003	12.872 ± 0.025	12.196 ± 0.024	10.400 ± 0.104	7.738 ± 0.170	12.769 ± 0.044	12.201 ± 0.023	II	Eastern
J053042.94+332813.6	15.739 ± 0.069	14.208 ± 0.046	13.135 ± 0.033	11.937 ± 0.023	10.998 ± 0.022	8.627 ± 0.032	5.073 ± 0.033	11.796 ± 0.029	11.119 ± 0.027	II	Eastern
J052947.45+332915.5	13.157 ± 0.023	12.130 ± 0.017	11.175 ± 0.018	10.094 ± 0.024	9.569 ± 0.020	8.036 ± 0.031	5.609 ± 0.043	9.857 ± 0.037	9.490 ± 0.038	II	Eastern
J053038.00+334901.9	15.621 ± 0.004	14.557 ± 0.003	13.858 ± 0.004	11.691 ± 0.030	11.210 ± 0.028	9.577 ± 0.094	6.823 ± 0.203	⋯	⋯	II	Eastern
J053042.36+334815.1	12.523 ± 0.023	11.502 ± 0.022	10.905 ± 0.019	10.332 ± 0.024	9.645 ± 0.021	7.193 ± 0.022	3.594 ± 0.023	10.195 ± 0.043	9.541 ± 0.049	II	Eastern
J053054.63+334730.9	15.971 ± 0.003	14.621 ± 0.004	13.579 ± 0.003	12.330 ± 0.023	11.430 ± 0.022	9.714 ± 0.064	6.739 ± 0.093	12.075 ± 0.038	11.434 ± 0.025	II	Eastern
J053007.63+332851.6	12.430 ± 0.023	12.110 ± 0.026	11.792 ± 0.023	11.068 ± 0.023	10.513 ± 0.021	7.530 ± 0.023	5.178 ± 0.049	⋯	⋯	II	Eastern
J052859.31+342327.1	15.585 ± 0.068	13.356 ± 0.038	11.729 ± 0.027	10.089 ± 0.028	10.089 ± 0.022	10.089 ± 0.028	10.089 ± 0.060	9.732 ± 0.026	9.053 ± 0.018	I	Eastern central
J052758.35+342552.1	16.982 ± 0.004	15.238 ± 0.006	13.787 ± 0.004	11.813 ± 0.024	11.813 ± 0.023	11.813 ± 0.032	11.813	11.606 ± 0.033	10.992 ± 0.027	I	Eastern central
J052836.88+341825.4	11.837 ± 0.019	11.700 ± 0.018	11.542 ± 0.020	11.214 ± 0.024	11.214 ± 0.022	11.214	11.214	11.145 ± 0.023	10.944 ± 0.021	II	Eastern central
J052835.78+342431.9	12.401 ± 0.019	11.450 ± 0.018	10.706 ± 0.018	10.044 ± 0.023	10.044 ± 0.022	10.044	10.044	9.831 ± 0.029	9.504 ± 0.043	II	Eastern central
SSTGLMCG173.4700 −00.0919	14.577 ± 0.042	12.901 ± 0.031	11.815 ± 0.023	⋯	⋯	⋯	⋯	10.656 ± 0.028	9.872 ± 0.016	II	Eastern central
J052804.58+342150.5	13.470 ± 0.001	12.811 ± 0.001	12.215 ± 0.001	11.230 ± 0.022	11.230 ± 0.022	11.230 ± 0.042	11.230 ± 0.133	11.012 ± 0.056	10.575 ± 0.034	II	Eastern central
SSTGLMCG173.3697 −00.2155	16.386 ± 0.003	14.698 ± 0.004	13.420 ± 0.003	⋯	⋯	⋯	⋯	11.249 ± 0.052	10.884 ± 0.025	II	Eastern central
SSTGLMCG173.3924 −00.1819	16.417 ± 0.010	15.346 ± 0.006	14.821 ± 0.009	⋯	⋯	⋯	⋯	14.081 ± 0.043	13.760 ± 0.034	II	Eastern central
SSTGLMCG173.4037 −00.1635	14.291 ± 0.001	12.944 ± 0.001	12.070 ± 0.001	⋯	⋯	⋯	⋯	10.791 ± 0.060	10.316 ± 0.023	II	Eastern central
SSTGLMCG173.4460 −00.1014	15.714 ± 0.006	14.678 ± 0.004	14.155 ± 0.006	⋯	⋯	⋯	⋯	13.325 ± 0.036	12.883 ± 0.021	II	Eastern central
J052810.83+342056.4	16.501 ± 0.006	15.074 ± 0.005	14.180 ± 0.005	13.485 ± 0.032	13.485 ± 0.034	13.485 ± 0.196	13.485 ± 0.260	13.108 ± 0.039	12.826 ± 0.038	II	Eastern central
SSTGLMCG173.3640 −00.1775	14.613 ± 0.003	13.721 ± 0.002	13.315 ± 0.003	⋯	⋯	⋯	⋯	12.530 ± 0.038	12.176 ± 0.022	II	Eastern central

Table 4
(Continued)

ID	J(1.25 μm) (mag)	H(1.65 μm) (mag)	K_s(2.17 μm) (mag)	$W1$(3.4 μm) (mag)	$W2$(4.6 μm) (mag)	$W3$(12 μm) (mag)	$W4$(22 μm) (mag)	[3.6] (mag)	[4.5] (mag)	Class	Region
(1)	(2)	(3)	(4)	(5)	(6)	(7)	(8)	(9)	(10)	(11)	(12)
J052802.20+342812.3	15.176 ± 0.003	14.119 ± 0.002	13.512 ± 0.003	12.791 ± 0.027	12.791 ± 0.032	12.791 ± 0.140	12.791 ± 0.508	12.721 ± 0.043	12.207 ± 0.020	II	Eastern central
J052805.34+342617.3	15.949 ± 0.006	14.840 ± 0.004	14.202 ± 0.005	13.323 ± 0.035	13.323 ± 0.031	13.323 ± 0.054	13.323 ± 0.029	13.128 ± 0.044	12.554 ± 0.024	II	Eastern central
J052724.68+342049.2	16.271 ± 0.008	15.213 ± 0.006	14.618 ± 0.008	13.995 ± 0.034	13.995 ± 0.041	13.995 ± 0.414	13.995	13.688 ± 0.047	13.298 ± 0.034	II	Eastern central
J052816.11+342811.9	15.532 ± 0.004	14.337 ± 0.003	13.684 ± 0.004	12.716 ± 0.026	12.716 ± 0.027	12.716 ± 0.062	12.716 ± 0.139	12.733 ± 0.039	12.220 ± 0.020	II	Eastern central
J052853.23+342335.3	14.759 ± 0.002	13.350 ± 0.001	12.447 ± 0.002	11.549 ± 0.027	11.549 ± 0.025	11.549 ± 0.080	11.549 ± 0.074	11.361 ± 0.023	10.897 ± 0.017	II	Eastern central
SSTGLMCG173.4531 −00.1209	19.201 ± 0.011	16.457 ± 0.018	14.895 ± 0.010	…	…	…	…	13.047 ± 0.031	12.363 ± 0.025	II	Eastern central
SSTGLMCG173.5025 −00.0846	20.147 ± 0.020	17.304 ± 0.039	15.562 ± 0.019	…	…	…	…	13.634 ± 0.045	12.832 ± 0.029	II	Eastern central
J052844.62+342313.6	16.681 ± 0.012	15.553 ± 0.007	14.985 ± 0.011	14.479 ± 0.138	14.479 ± 0.119	14.479	14.479	14.229 ± 0.032	13.930 ± 0.033	II	Eastern central
J052818.16+341651.9	14.090 ± 0.002	13.388 ± 0.001	12.945 ± 0.002	12.410 ± 0.025	12.410 ± 0.024	12.410 ± 0.038	12.410 ± 0.122	12.456 ± 0.036	11.956 ± 0.030	II	Eastern central
SSTGLMCG173.4557 −00.1047	16.014 ± 0.008	14.954 ± 0.004	14.505 ± 0.007	…	…	…	…	13.616 ± 0.084	13.256 ± 0.038	II	Eastern central
J052714.69+343004.0	15.571 ± 0.006	15.071 ± 0.007	14.206 ± 0.006	13.525 ± 0.028	13.525 ± 0.031	13.525	13.525	13.250 ± 0.047	12.811 ± 0.039	II	Eastern central
J052819.63+343535.3	15.168 ± 0.004	14.166 ± 0.002	13.646 ± 0.004	13.066 ± 0.027	13.066 ± 0.026	13.066	13.066	12.942 ± 0.027	12.620 ± 0.021	II	Eastern central
SSTGLMCG173.3691 −00.1820	15.948 ± 0.008	15.023 ± 0.005	14.577 ± 0.007	…	…	…	…	13.827 ± 0.045	13.447 ± 0.031	II	Eastern central
J052803.88+342432.3	16.780 ± 0.007	15.284 ± 0.006	14.491 ± 0.007	13.431 ± 0.027	13.431 ± 0.042	13.431	13.431 ± 0.272	13.374 ± 0.061	12.960 ± 0.034	II	Eastern central
J052809.35+342724.7	16.671 ± 0.012	15.666 ± 0.008	15.044 ± 0.011	14.707 ± 0.052	14.707 ± 0.117	14.707	14.707 ± 0.399	14.522 ± 0.058	13.869 ± 0.039	II	Eastern central
SSTGLMCG173.3932 −00.2073	16.081 ± 0.010	15.242 ± 0.005	14.854 ± 0.009	…	…	…	…	14.282 ± 0.045	14.054 ± 0.033	II	Eastern central
SSTGLMCG173.3309 −00.1961	16.402 ± 0.010	15.344 ± 0.006	14.887 ± 0.010	…	…	…	…	14.199 ± 0.123	13.872 ± 0.063	II	Eastern central
SSTGLMCG173.4651 −00.0886	16.034 ± 0.006	14.940 ± 0.004	14.265 ± 0.006	…	…	…	…	13.672 ± 0.030	13.031 ± 0.024	II	Eastern central
SSTGLMCG173.4119 −00.1651	16.580 ± 0.005	14.794 ± 0.004	13.847 ± 0.004	…	…	…	…	12.855 ± 0.075	12.467 ± 0.030	II	Eastern central
SSTGLMCG173.5089 −00.0661	18.702 ± 0.014	16.474 ± 0.018	15.161 ± 0.013	…	…	…	…	13.804 ± 0.035	13.227 ± 0.025	II	Eastern central
J052804.78+343618.0	15.716 ± 0.007	14.910 ± 0.006	14.420 ± 0.007	13.851 ± 0.034	13.851 ± 0.037	13.851 ± 0.101	13.851 ± 0.272	13.869 ± 0.031	13.482 ± 0.027	II	Eastern central
SSTGLMCG173.3752 −00.1770	16.457 ± 0.013	15.584 ± 0.007	15.134 ± 0.012	…	…	…	…	14.235 ± 0.053	13.795 ± 0.037	II	Eastern central
SSTGLMCG173.3929 −00.1989	15.753 ± 0.006	14.712 ± 0.004	14.197 ± 0.005	…	…	…	…	13.417 ± 0.037	13.193 ± 0.029	II	Eastern central

Table 4
(Continued)

ID	J(1.25 μm) (mag)	H(1.65 μm) (mag)	K_s(2.17 μm) (mag)	$W1$(3.4 μm) (mag)	$W2$(4.6 μm) (mag)	$W3$(12 μm) (mag)	$W4$(22 μm) (mag)	[3.6] (mag)	[4.5] (mag)	Class	Region
(1)	(2)	(3)	(4)	(5)	(6)	(7)	(8)	(9)	(10)	(11)	(12)
J052810.14+342544.2	13.755 ± 0.002	12.949 ± 0.001	12.577 ± 0.002	12.025 ± 0.028	12.025 ± 0.028	12.025 ± 0.028	12.025 ± 0.033	12.262 ± 0.037	11.707 ± 0.022	II	Eastern central
SSTGLMCG173.3528 −00.1873	14.926 ± 0.004	13.991 ± 0.002	13.581 ± 0.003	…	…	…	…	13.038 ± 0.043	12.638 ± 0.023	II	Eastern central
J052816.02+342728.0	14.355 ± 0.002	13.268 ± 0.001	12.521 ± 0.002	11.948 ± 0.025	11.948 ± 0.023	11.948 ± 0.098	11.948 ± 0.260	11.825 ± 0.035	11.420 ± 0.025	II	Eastern central
J052757.82+342920.4	17.616 ± 0.015	16.098 ± 0.017	15.299 ± 0.014	14.006 ± 0.033	14.006 ± 0.039	14.006 ± 0.252	14.006	14.181 ± 0.034	13.675 ± 0.030	II	Eastern central
SSTGLMCG173.4883 −00.1186	16.570 ± 0.015	15.651 ± 0.008	15.270 ± 0.014	…	…	…	…	14.571 ± 0.035	14.332 ± 0.044	II	Eastern central
J052812.27+342341.7	16.211 ± 0.005	14.827 ± 0.004	14.004 ± 0.005	13.031 ± 0.033	13.031 ± 0.036	13.031	13.031	12.830 ± 0.041	12.290 ± 0.024	II	Eastern central
SSTGLMCG173.2719 −00.2071	15.471 ± 0.004	14.339 ± 0.004	13.790 ± 0.004	…	…	…	…	13.256 ± 0.034	12.787 ± 0.031	II	Eastern central
J052737.66+343320.7	15.753 ± 0.005	14.630 ± 0.005	14.015 ± 0.005	13.350 ± 0.029	13.350 ± 0.030	13.350 ± 0.410	13.350	13.175 ± 0.036	12.574 ± 0.033	II	Eastern central
SSTGLMCG173.4520 −00.1156	18.201 ± 0.007	15.709 ± 0.009	14.251 ± 0.006	…	…	…	…	12.716 ± 0.071	11.981 ± 0.033	II	Eastern central
SSTGLMCG173.2431 −00.1355	17.071 ± 0.012	15.828 ± 0.013	15.015 ± 0.011	…	…	…	…	13.888 ± 0.026	13.283 ± 0.027	II	Eastern central
J052855.86+344328.7	15.985 ± 0.008	15.041 ± 0.005	14.577 ± 0.008	14.184 ± 0.032	14.184 ± 0.045	14.184	14.184	14.127 ± 0.053	13.753 ± 0.029	II	Eastern central
J052907.72+344608.0	14.980 ± 0.003	14.031 ± 0.002	13.425 ± 0.003	12.631 ± 0.025	12.631 ± 0.026	12.631	12.631	12.523 ± 0.050	12.248 ± 0.024	II	Eastern central
J052807.88+341841.7	16.803	15.498	14.754 ± 0.098	12.749 ± 0.024	11.594 ± 0.023	8.528 ± 0.042	6.153 ± 0.099	12.456 ± 0.038	11.646 ± 0.029	I	Eastern central
J052813.97+343428.5	14.593 ± 0.002	13.794 ± 0.002	12.989 ± 0.002	12.386 ± 0.024	11.485 ± 0.022	7.694 ± 0.028	6.063 ± 0.057	12.145 ± 0.027	11.486 ± 0.021	I	Eastern central
J052919.51+344246.5	18.897 ± 0.015	17.119 ± 0.035	15.340 ± 0.014	12.883 ± 0.025	11.398 ± 0.022	8.529 ± 0.028	6.413 ± 0.067	12.451 ± 0.045	11.425 ± 0.018	I	Eastern central
J052901.61+340931.2	14.232 ± 0.002	13.266 ± 0.001	12.485 ± 0.002	11.562 ± 0.022	11.065 ± 0.021	8.485 ± 0.028	6.394 ± 0.082	11.371 ± 0.016	11.053 ± 0.025	II	Eastern central
J052751.87+341509.4	13.859 ± 0.002	13.234 ± 0.001	12.790 ± 0.002	12.156 ± 0.024	11.664 ± 0.022	8.852 ± 0.049	6.972 ± 0.122	11.995 ± 0.044	11.684 ± 0.036	II	Eastern central
J052800.15+341645.0	15.111 ± 0.003	14.156 ± 0.002	13.464 ± 0.003	12.444 ± 0.025	11.823 ± 0.024	10.026 ± 0.078	7.385 ± 0.149	12.368 ± 0.053	11.751 ± 0.027	II	Eastern central
J052751.71+342121.8	15.796 ± 0.005	14.627 ± 0.003	13.887 ± 0.004	12.842 ± 0.024	12.356 ± 0.026	10.119 ± 0.082	7.225	12.740 ± 0.036	12.360 ± 0.032	II	Eastern central
J052807.70+342624.6	11.679 ± 0.030	11.388 ± 0.019	11.174 ± 0.018	10.720 ± 0.024	10.382 ± 0.021	8.583 ± 0.030	4.271 ± 0.043	…	…	II	Eastern central
J052803.43+342521.7	13.843 ± 0.001	12.820 ± 0.001	12.167 ± 0.001	11.333 ± 0.027	10.877 ± 0.025	8.458 ± 0.036	7.360 ± 0.457	11.119 ± 0.043	10.794 ± 0.022	II	Eastern central
J052745.79+343054.2	14.137 ± 0.032	12.605 ± 0.022	11.550 ± 0.019	10.413 ± 0.024	9.398 ± 0.021	6.748 ± 0.021	4.513 ± 0.040	…	…	II	Eastern central
J052737.13+343243.3	13.791 ± 0.001	13.021 ± 0.001	11.960 ± 0.001	10.647 ± 0.023	9.915 ± 0.021	8.071 ± 0.024	5.239 ± 0.038	10.415 ± 0.036	9.907 ± 0.021	II	Eastern central

Table 4
(Continued)

ID	J(1.25 μm) (mag)	H(1.65 μm) (mag)	K_s(2.17 μm) (mag)	$W1$(3.4 μm) (mag)	$W2$(4.6 μm) (mag)	$W3$(12 μm) (mag)	$W4$(22 μm) (mag)	[3.6] (mag)	[4.5] (mag)	Class	Region
(1)	(2)	(3)	(4)	(5)	(6)	(7)	(8)	(9)	(10)	(11)	(12)
J052730.22+343240.8	13.142 ± 0.001	12.568 ± 0.001	11.989 ± 0.001	11.174 ± 0.026	10.479 ± 0.026	7.282 ± 0.021	5.174 ± 0.037	10.934 ± 0.034	10.425 ± 0.028	II	Eastern central
J052918.63+342247.6	14.430 ± 0.032	13.089 ± 0.023	12.268 ± 0.023	11.053 ± 0.024	10.242 ± 0.021	7.868 ± 0.071	5.539 ± 0.135	⋯	⋯	II	Eastern central
J052912.60+342230.6	17.247 ± 0.004	14.953 ± 0.005	13.460 ± 0.003	12.014 ± 0.037	10.961 ± 0.028	8.622 ± 0.112	5.681 ± 0.221	12.028 ± 0.027	11.270 ± 0.015	II	Eastern central
J052849.55+342326.7	13.719 ± 0.023	12.478 ± 0.022	11.476 ± 0.021	10.444 ± 0.023	9.371 ± 0.021	6.723 ± 0.018	3.964 ± 0.031	9.791 ± 0.032	9.233 ± 0.021	II	Eastern central
J052817.07+342803.3	12.755 ± 0.019	11.930 ± 0.019	11.433 ± 0.018	10.678 ± 0.022	10.330 ± 0.020	7.839 ± 0.032	5.442 ± 0.062	10.526 ± 0.035	10.283 ± 0.019	II	Eastern central
J052833.01+343458.1	14.598 ± 0.002	13.469 ± 0.002	12.804 ± 0.002	12.011 ± 0.024	11.452 ± 0.021	9.361 ± 0.093	7.087 ± 0.132	11.809 ± 0.032	11.347 ± 0.020	II	Eastern central
J052811.98+343341.8	14.550 ± 0.002	13.411 ± 0.001	12.723 ± 0.002	11.874 ± 0.027	11.388 ± 0.022	9.434 ± 0.103	7.865 ± 0.328	11.720 ± 0.028	11.339 ± 0.020	II	Eastern central
J052937.37+342217.5	16.031 ± 0.003	14.263 ± 0.003	13.341 ± 0.003	11.812 ± 0.031	10.784 ± 0.021	9.232 ± 0.052	6.338 ± 0.146	11.480 ± 0.026	10.732 ± 0.018	I	Eastern central
J052744.99+341752.7	14.794 ± 0.003	13.991 ± 0.002	13.494 ± 0.003	12.553 ± 0.026	12.124 ± 0.027	9.041 ± 0.054	6.611 ± 0.133	12.602 ± 0.040	12.238 ± 0.030	II	Eastern central
J052804.41+342457.3	14.340 ± 0.002	13.431 ± 0.001	12.846 ± 0.002	11.936 ± 0.024	11.489 ± 0.025	9.476 ± 0.116	6.628 ± 0.299	11.934 ± 0.034	11.449 ± 0.020	II	Eastern central
J052810.42+342440.6	13.453 ± 0.001	12.471 ± 0.001	11.892 ± 0.001	11.229 ± 0.027	10.785 ± 0.032	8.139 ± 0.147	4.210 ± 0.223	11.072 ± 0.035	10.839 ± 0.020	II	Eastern central
J052812.75+342553.3	17.243 ± 0.025	16.359 ± 0.015	15.879 ± 0.024	12.168 ± 0.027	11.753 ± 0.031	11.550	6.910 ± 0.208	12.227 ± 0.044	11.871 ± 0.025	II	Eastern central
J052730.30+342342.6	15.095 ± 0.054	13.590 ± 0.055	12.663 ± 0.039	11.445 ± 0.025	10.675 ± 0.022	8.933 ± 0.372	5.408 ± 0.164	11.523 ± 0.044	10.925 ± 0.027	II	Eastern central
J052912.22+342218.3	15.008 ± 0.043	13.463 ± 0.026	12.733 ± 0.024	12.005 ± 0.037	11.414 ± 0.032	8.135 ± 0.078	4.870 ± 0.099	11.936 ± 0.019	11.511 ± 0.015	II	Eastern central
J052916.53+342226.6	13.791 ± 0.028	12.272 ± 0.020	11.314 ± 0.021	10.528 ± 0.024	9.777 ± 0.021	7.738 ± 0.033	4.947 ± 0.052	⋯	⋯	II	Eastern central
J052649.24+350918.0	14.392 ± 0.002	13.271 ± 0.002	12.755 ± 0.002	11.922 ± 0.023	11.922 ± 0.022	11.922 ± 0.025	11.922 ± 0.040	12.195 ± 0.052	11.803 ± 0.034	II	Northern central
J052705.72+350205.6	16.561 ± 0.012	15.543 ± 0.008	14.977 ± 0.012	14.574 ± 0.036	14.574 ± 0.043	14.574 ± 0.252	14.574 ± 0.208	14.476 ± 0.053	14.017 ± 0.050	II	Northern central
J052513.89+352422.1	17.065 ± 0.021	16.005 ± 0.017	15.487 ± 0.020	14.635 ± 0.037	14.635 ± 0.052	14.635 ± 0.389	14.635	14.583 ± 0.071	14.280 ± 0.036	II	Northern central
SSTGLMCG172.6114 −00.0196	17.955 ± 0.024	16.439 ± 0.027	15.649 ± 0.023	⋯	⋯	⋯	⋯	14.763 ± 0.050	14.002 ± 0.029	II	Northern central
J052513.43+352454.5	15.587 ± 0.005	14.518 ± 0.005	13.883 ± 0.005	13.176 ± 0.025	13.176 ± 0.027	13.176 ± 0.061	13.176 ± 0.160	13.049 ± 0.049	12.657 ± 0.025	II	Northern central
J052707.65+345725.3	15.808 ± 0.004	14.458 ± 0.004	13.755 ± 0.004	12.279 ± 0.023	12.279 ± 0.023	12.279 ± 0.043	12.279 ± 0.117	12.503 ± 0.037	12.082 ± 0.023	II	Northern central
J052638.68+350908.6	17.782 ± 0.043	16.773 ± 0.035	16.279 ± 0.040	14.180 ± 0.045	14.180 ± 0.052	14.180	14.180	14.106 ± 0.059	13.819 ± 0.035	II	Northern central
J052547.46+353318.2	16.174 ± 0.009	15.106 ± 0.008	14.534 ± 0.009	13.709 ± 0.031	13.709 ± 0.035	13.709 ± 0.193	13.709 ± 0.410	13.887 ± 0.041	13.652 ± 0.038	II	Northern central

Table 4
(Continued)

ID	J(1.25 μm) (mag)	H(1.65 μm) (mag)	K_s(2.17 μm) (mag)	$W1$(3.4 μm) (mag)	$W2$(4.6 μm) (mag)	$W3$(12 μm) (mag)	$W4$(22 μm) (mag)	[3.6] (mag)	[4.5] (mag)	Class	Region
(1)	(2)	(3)	(4)	(5)	(6)	(7)	(8)	(9)	(10)	(11)	(12)
J052726.33+351352.0	16.147 ± 0.006	14.931 ± 0.006	14.205 ± 0.006	13.268 ± 0.028	13.268 ± 0.028	13.268 ± 0.171	13.268	13.268 ± 0.047	12.687 ± 0.040	II	Northern central
SSTGLMCG172.8280 +00.1166	16.929 ± 0.022	16.087 ± 0.016	15.652 ± 0.021	…	…	…	…	14.224 ± 0.041	13.687 ± 0.035	II	Northern central
J052707.65+350200.8	14.977 ± 0.002	13.611 ± 0.002	12.954 ± 0.002	12.055 ± 0.027	11.306 ± 0.023	8.847 ± 0.035	6.515 ± 0.102	11.847 ± 0.043	11.337 ± 0.033	II	Northern central
J052708.38+350210.7	15.621 ± 0.004	14.400 ± 0.004	13.693 ± 0.004	12.838 ± 0.034	12.001 ± 0.025	9.185 ± 0.044	6.473 ± 0.074	12.824 ± 0.051	12.216 ± 0.042	II	Northern central
J052641.67+350857.0	18.369 ± 0.007	16.081 ± 0.020	14.101 ± 0.006	11.858 ± 0.022	11.060 ± 0.021	8.511 ± 0.049	6.135 ± 0.062	11.653 ± 0.040	11.049 ± 0.021	II	Northern central
J052647.06+350843.2	14.195 ± 0.052	12.387 ± 0.039	11.258 ± 0.023	9.834 ± 0.022	8.943 ± 0.020	6.700 ± 0.023	4.478 ± 0.033	9.670 ± 0.064	9.217 ± 0.044	II	Northern central
J052726.03+345959.7	14.300 ± 0.002	13.944 ± 0.003	12.987 ± 0.002	12.479 ± 0.024	12.225 ± 0.023	10.310 ± 0.086	8.020 ± 0.269	12.560 ± 0.062	12.309 ± 0.043	II	Northern central
J052732.45+350240.8	14.560 ± 0.002	13.531 ± 0.002	12.812 ± 0.002	12.118 ± 0.023	11.716 ± 0.023	9.911 ± 0.057	8.267	12.157 ± 0.048	11.822 ± 0.027	II	Northern central
J052543.82+353238.4	13.719 ± 0.001	12.580 ± 0.001	12.089 ± 0.001	11.528 ± 0.023	11.142 ± 0.022	9.660 ± 0.057	8.660 ± 0.506	11.497 ± 0.053	11.212 ± 0.053	II	Northern central
J052541.55+353323.4	16.234 ± 0.005	14.646 ± 0.005	13.736 ± 0.004	12.844 ± 0.025	12.223 ± 0.025	9.734 ± 0.066	8.128 ± 0.262	12.632 ± 0.034	12.237 ± 0.029	II	Northern central
J052609.02+351538.2	14.421 ± 0.002	13.345 ± 0.002	12.763 ± 0.002	12.046 ± 0.024	11.375 ± 0.021	10.435 ± 0.156	8.499	…	…	II	Northern central
J052441.02+343459.3	18.176 ± 0.016	16.389 ± 0.017	15.280 ± 0.015	13.995 ± 0.031	13.995 ± 0.030	13.995 ± 0.076	13.995 ± 0.207	13.381 ± 0.023	12.599 ± 0.021	I	Southern central
J052418.51+350507.3	17.722 ± 0.045	16.865 ± 0.023	16.552 ± 0.043	13.890 ± 0.028	13.890 ± 0.032	13.890	13.890	13.708 ± 0.061	13.308 ± 0.039	I	Southern central
J052504.62+345915.9	18.255 ± 0.010	16.517 ± 0.017	14.831 ± 0.009	12.165 ± 0.023	12.165 ± 0.021	12.165 ± 0.027	12.165 ± 0.043	11.943 ± 0.036	10.979 ± 0.025	I	Southern central
SSTGLMCG172.7272 −00.3329	…	17.020 ± 0.024	14.555 ± 0.008	…	…	…	…	12.425 ± 0.048	11.374 ± 0.040	I	Southern central
J052603.56+344350.7	13.529 ± 0.027	12.516 ± 0.029	12.006 ± 0.024	11.351 ± 0.024	11.351 ± 0.021	11.351 ± 0.028	11.351 ± 0.082	11.210 ± 0.045	10.773 ± 0.036	II	Southern central
J052445.14+343118.6	18.210 ± 0.016	16.547 ± 0.020	15.299 ± 0.015	13.995 ± 0.030	13.995 ± 0.033	13.995 ± 0.290	13.995	14.011 ± 0.037	13.531 ± 0.026	II	Southern central
SSTGLMCG172.7681 −00.3029	16.458 ± 0.011	15.437 ± 0.007	14.877 ± 0.010	…	…	…	…	14.229 ± 0.057	13.905 ± 0.047	II	Southern central
J052614.66+345005.0	15.879 ± 0.007	14.824 ± 0.004	14.307 ± 0.007	13.277 ± 0.026	13.277 ± 0.032	13.277 ± 0.300	13.277	13.208 ± 0.044	12.882 ± 0.028	II	Southern central
J052620.88+345117.8	16.322 ± 0.011	15.293 ± 0.006	14.832 ± 0.010	13.523 ± 0.027	13.523 ± 0.033	13.523	13.523	14.271 ± 0.074	13.829 ± 0.086	II	Southern central
J052616.81+345421.9	15.577 ± 0.005	14.618 ± 0.004	14.014 ± 0.005	13.384 ± 0.026	13.384 ± 0.028	13.384 ± 0.069	13.384 ± 0.110	13.247 ± 0.045	12.784 ± 0.030	II	Southern central
SSTGLMCG172.8359 −00.2715	16.341 ± 0.012	15.365 ± 0.007	14.946 ± 0.011	…	…	…	…	14.465 ± 0.065	14.035 ± 0.041	II	Southern central
J052619.46+344943.6	15.486 ± 0.006	14.457 ± 0.003	14.034 ± 0.005	13.452 ± 0.029	13.452 ± 0.033	13.452 ± 0.086	13.452 ± 0.248	13.392 ± 0.048	13.079 ± 0.038	II	Southern central

Table 4
(Continued)

ID	J(1.25 μm) (mag)	H(1.65 μm) (mag)	K_s(2.17 μm) (mag)	$W1$(3.4 μm) (mag)	$W2$(4.6 μm) (mag)	$W3$(12 μm) (mag)	$W4$(22 μm) (mag)	[3.6] (mag)	[4.5] (mag)	Class	Region
(1)	(2)	(3)	(4)	(5)	(6)	(7)	(8)	(9)	(10)	(11)	(12)
J052340.04+344838.8	16.792 ± 0.014	15.744 ± 0.010	15.107 ± 0.013	14.496 ± 0.034	14.496 ± 0.043	14.496	14.496	14.415 ± 0.049	13.932 ± 0.026	II	Southern central
J052433.88+350603.4	16.440 ± 0.005	14.906 ± 0.004	13.957 ± 0.005	12.935 ± 0.028	12.935 ± 0.026	12.935 ± 0.247	12.935 ± 0.428	12.595 ± 0.037	11.970 ± 0.031	II	Southern central
J052445.42+343133.3	15.923 ± 0.007	14.816 ± 0.004	14.301 ± 0.006	13.363 ± 0.028	13.363 ± 0.026	13.363 ± 0.073	13.363 ± 0.338	13.188 ± 0.028	12.618 ± 0.026	II	Southern central
SSTGLMCG172.5585 −00.3926	18.867 ± 0.025	16.964 ± 0.026	15.899 ± 0.024	…	…	…	…	14.782 ± 0.054	14.270 ± 0.037	II	Southern central
J052447.04+344221.3	15.422 ± 0.004	14.388 ± 0.003	13.809 ± 0.004	13.085 ± 0.026	13.085 ± 0.027	13.085 ± 0.178	13.085	12.727 ± 0.024	12.123 ± 0.018	II	Southern central
J052535.51+345813.2	16.461 ± 0.013	15.688 ± 0.008	15.139 ± 0.012	14.800 ± 0.042	14.800 ± 0.057	14.800	14.800	14.443 ± 0.053	13.771 ± 0.059	II	Southern central
SSTGLMCG172.6582 −00.3205	16.217 ± 0.010	15.364 ± 0.006	14.810 ± 0.009	…	…	…	…	14.108 ± 0.042	13.808 ± 0.045	II	Southern central
J052507.66+345902.2	16.969 ± 0.016	15.975 ± 0.010	15.383 ± 0.015	15.141 ± 0.046	15.141 ± 0.065	15.141	15.141	14.653 ± 0.059	14.264 ± 0.045	II	Southern central
J052644.62+344355.6	16.893 ± 0.014	15.744 ± 0.009	15.119 ± 0.013	15.103 ± 0.043	15.103 ± 0.060	15.103	15.103	14.721 ± 0.058	14.206 ± 0.037	II	Southern central
J052606.06+344442.2	16.321 ± 0.011	15.410 ± 0.007	14.850 ± 0.010	13.976 ± 0.031	13.976 ± 0.035	13.976	13.976	13.584 ± 0.038	13.168 ± 0.039	II	Southern central
SSTGLMCG172.6308 −00.3190	16.183 ± 0.011	15.344 ± 0.006	14.916 ± 0.010	…	…	…	…	14.328 ± 0.057	14.036 ± 0.049	II	Southern central
J052538.35+345636.1	17.358 ± 0.018	16.286 ± 0.014	15.515 ± 0.017	14.491 ± 0.055	14.491 ± 0.061	14.491	14.491	14.469 ± 0.050	13.861 ± 0.050	II	Southern central
J052541.77+350022.1	15.632 ± 0.006	14.746 ± 0.004	14.284 ± 0.006	14.035 ± 0.030	14.035 ± 0.034	14.035 ± 0.231	14.035 ± 0.407	13.751 ± 0.041	13.358 ± 0.028	II	Southern central
SSTGLMCG172.7503 −00.5578	17.512 ± 0.011	15.758 ± 0.009	14.879 ± 0.010	…	…	…	…	13.617 ± 0.050	13.016 ± 0.025	II	Southern central
SSTGLMCG172.8703 −00.2731	15.426 ± 0.005	14.421 ± 0.003	13.916 ± 0.005	…	…	…	…	13.348 ± 0.039	13.090 ± 0.035	II	Southern central
J052355.40+344510.4	18.641 ± 0.038	17.100 ± 0.029	16.398 ± 0.036	14.828 ± 0.041	14.828 ± 0.049	14.828 ± 0.223	14.828	14.835 ± 0.052	14.252 ± 0.035	II	Southern central
J052509.15+345848.7	16.515 ± 0.005	15.154 ± 0.005	14.009 ± 0.005	13.482 ± 0.027	13.482 ± 0.031	13.482	13.482	13.347 ± 0.065	12.819 ± 0.036	II	Southern central
J052534.05+345747.2	15.139 ± 0.004	14.077 ± 0.002	13.545 ± 0.003	12.941 ± 0.024	12.941 ± 0.025	12.941 ± 0.059	12.941 ± 0.083	12.894 ± 0.036	12.405 ± 0.039	II	Southern central
J052534.56+345812.2	16.245 ± 0.009	15.229 ± 0.006	14.656 ± 0.008	14.006 ± 0.029	14.006 ± 0.034	14.006 ± 0.101	14.006 ± 0.296	13.934 ± 0.047	13.509 ± 0.040	II	Southern central
SSTGLMCG172.6111 −00.3175	16.678 ± 0.005	15.041 ± 0.005	13.908 ± 0.004	…	…	…	…	12.322 ± 0.028	11.708 ± 0.026	II	Southern central
J052618.28+344716.9	15.547 ± 0.006	14.630 ± 0.004	14.191 ± 0.006	13.733 ± 0.033	13.733 ± 0.034	13.733 ± 0.218	13.733	13.557 ± 0.038	13.130 ± 0.033	II	Southern central
J052510.02+344507.4	14.492 ± 0.002	13.557 ± 0.002	12.713 ± 0.002	12.029 ± 0.023	12.029 ± 0.022	12.029 ± 0.040	12.029 ± 0.099	11.820 ± 0.028	11.371 ± 0.023	II	Southern central
J052459.26+350300.0	16.432 ± 0.012	15.536 ± 0.007	15.070 ± 0.011	14.661 ± 0.038	14.661 ± 0.045	14.661 ± 0.485	14.661	14.373 ± 0.043	13.954 ± 0.046	II	Southern central

Table 4
(Continued)

ID	J(1.25 μm) (mag)	H(1.65 μm) (mag)	K_s(2.17 μm) (mag)	$W1$(3.4 μm) (mag)	$W2$(4.6 μm) (mag)	$W3$(12 μm) (mag)	$W4$(22 μm) (mag)	[3.6] (mag)	[4.5] (mag)	Class	Region
(1)	(2)	(3)	(4)	(5)	(6)	(7)	(8)	(9)	(10)	(11)	(12)
J052648.19+344127.3	16.793 ± 0.010	15.597 ± 0.008	14.855 ± 0.009	14.059 ± 0.030	14.059 ± 0.038	14.059	14.059	14.258 ± 0.049	13.690 ± 0.034	II	Southern central
J052444.55+343211.2	16.755	15.857 ± 0.155	14.223 ± 0.086	12.726 ± 0.037	11.530 ± 0.032	9.001 ± 0.045	6.518 ± 0.139	⋯	⋯	I	Southern central
J052438.60+343526.6	18.405 ± 0.045	17.065 ± 0.031	16.459 ± 0.042	11.477 ± 0.024	10.155 ± 0.021	7.412 ± 0.018	4.852 ± 0.033	10.991 ± 0.030	10.013 ± 0.019	I	Southern central
J052533.38+343959.2	16.095 ± 0.005	14.662 ± 0.004	13.858 ± 0.004	12.765 ± 0.026	11.685 ± 0.024	8.540 ± 0.029	5.971 ± 0.067	12.720 ± 0.026	11.815 ± 0.019	I	Southern central
J052643.59+344750.7	16.194 ± 0.003	14.517 ± 0.003	13.362 ± 0.003	12.148 ± 0.024	11.181 ± 0.022	8.035 ± 0.027	5.891 ± 0.060	11.938 ± 0.029	11.278 ± 0.024	I	Southern central
J052515.41+345806.4	16.335 ± 0.003	14.485 ± 0.003	13.348 ± 0.003	12.374 ± 0.023	11.340 ± 0.021	8.497 ± 0.051	5.751 ± 0.063	11.971 ± 0.041	11.255 ± 0.032	I	Southern central
J052525.23+345842.1	18.110	16.246 ± 0.206	14.372 ± 0.091	10.962 ± 0.026	9.498 ± 0.025	6.959 ± 0.033	4.512 ± 0.053	10.124 ± 0.040	9.223 ± 0.030	I	Southern central
J052454.48+343023.7	13.465 ± 0.001	12.378 ± 0.001	11.720 ± 0.001	11.002 ± 0.023	10.216 ± 0.019	8.118 ± 0.024	6.146 ± 0.055	10.808 ± 0.027	10.237 ± 0.018	II	Southern central
J052452.63+343039.0	18.047 ± 0.035	16.664 ± 0.022	16.176 ± 0.033	12.037 ± 0.024	10.866 ± 0.020	8.513 ± 0.030	6.094 ± 0.062	12.006 ± 0.031	11.084 ± 0.019	II	Southern central
J052444.15+343212.6	15.789 ± 0.070	14.458 ± 0.060	13.547 ± 0.056	12.591 ± 0.034	11.720 ± 0.036	9.915 ± 0.091	7.775	⋯	⋯	II	Southern central
J052340.89+344824.3	15.971 ± 0.005	14.653 ± 0.004	13.761 ± 0.004	12.937 ± 0.041	12.201 ± 0.037	9.681 ± 0.058	7.055 ± 0.155	12.630 ± 0.037	12.206 ± 0.018	II	Southern central
J052632.79+344915.9	14.763 ± 0.003	13.675 ± 0.002	13.049 ± 0.002	11.947 ± 0.024	11.273 ± 0.024	9.615 ± 0.052	7.974 ± 0.255	11.792 ± 0.046	11.272 ± 0.026	II	Southern central
J052505.00+344132.2	15.389 ± 0.004	14.324 ± 0.003	13.727 ± 0.004	12.776 ± 0.032	11.832 ± 0.026	8.964 ± 0.032	6.566 ± 0.070	12.354 ± 0.024	11.666 ± 0.022	II	Southern central
J052447.81+344251.5	16.700 ± 0.005	15.026 ± 0.005	13.974 ± 0.005	12.853 ± 0.025	12.079 ± 0.024	9.974 ± 0.081	8.326 ± 0.496	12.610 ± 0.027	12.089 ± 0.018	II	Southern central
J052457.20+344415.3	15.632 ± 0.002	13.992 ± 0.002	12.892 ± 0.002	11.644 ± 0.022	10.882 ± 0.021	8.261 ± 0.025	5.585 ± 0.045	11.590 ± 0.051	11.094 ± 0.016	II	Southern central
J052554.38+345439.1	13.717 ± 0.001	12.438 ± 0.001	11.523 ± 0.001	10.506 ± 0.022	9.986 ± 0.020	8.199 ± 0.022	6.202 ± 0.056	10.500 ± 0.027	10.006 ± 0.030	II	Southern central
J052552.02+345807.9	15.214 ± 0.049	13.988 ± 0.041	13.009 ± 0.036	11.505 ± 0.024	10.645 ± 0.022	8.141 ± 0.026	5.816 ± 0.057	11.218 ± 0.032	10.719 ± 0.024	II	Southern central
J052526.60+345756.5	15.353 ± 0.003	14.014 ± 0.002	13.104 ± 0.002	12.083 ± 0.023	11.510 ± 0.022	8.361 ± 0.039	6.033 ± 0.065	11.965 ± 0.032	11.494 ± 0.029	II	Southern central
J052510.53+345933.4	17.396 ± 0.006	15.514 ± 0.007	14.216 ± 0.006	12.520 ± 0.024	11.581 ± 0.022	8.838 ± 0.046	6.682 ± 0.088	12.259 ± 0.046	11.550 ± 0.031	II	Southern central
J052532.00+345835.7	16.105 ± 0.006	14.995 ± 0.005	14.220 ± 0.006	12.887 ± 0.057	12.213 ± 0.043	8.915 ± 0.042	6.652 ± 0.125	13.029 ± 0.045	12.474 ± 0.033	II	Southern central
J052532.08+345815.2	16.273 ± 0.006	14.911 ± 0.004	14.268 ± 0.006	12.455 ± 0.026	11.647 ± 0.023	9.057 ± 0.038	6.180 ± 0.081	13.575 ± 0.067	13.086 ± 0.049	II	Southern central
J052443.53+350044.1	15.185 ± 0.002	13.845 ± 0.002	13.030 ± 0.002	12.170 ± 0.026	11.466 ± 0.021	9.364 ± 0.075	7.233 ± 0.184	11.999 ± 0.039	11.484 ± 0.025	II	Southern central
J052447.00+350139.1	15.492 ± 0.003	14.127 ± 0.002	13.292 ± 0.003	12.519 ± 0.025	11.953 ± 0.024	9.495 ± 0.076	6.927 ± 0.106	12.214 ± 0.031	11.872 ± 0.029	II	Southern central

Table 4
(Continued)

ID	J(1.25 μm) (mag)	H(1.65 μm) (mag)	K_s(2.17 μm) (mag)	$W1$(3.4 μm) (mag)	$W2$(4.6 μm) (mag)	$W3$(12 μm) (mag)	$W4$(22 μm) (mag)	[3.6] (mag)	[4.5] (mag)	Class	Region
(1)	(2)	(3)	(4)	(5)	(6)	(7)	(8)	(9)	(10)	(11)	(12)
J052443.57+350132.7	14.588 ± 0.002	13.377 ± 0.001	12.694 ± 0.002	11.526 ± 0.024	10.745 ± 0.021	8.525 ± 0.048	5.919 ± 0.070	11.260 ± 0.033	10.711 ± 0.022	II	Southern central
J052435.61+350311.1	14.926 ± 0.002	13.611 ± 0.002	12.573 ± 0.002	10.675 ± 0.024	9.589 ± 0.021	7.390 ± 0.024	4.862 ± 0.037	⋯	⋯	II	Southern central
J052454.63+351155.2	15.006 ± 0.040	12.733 ± 0.024	11.585 ± 0.023	11.046 ± 0.023	10.623 ± 0.020	9.439 ± 0.050	6.911 ± 0.107	10.767 ± 0.036	10.614 ± 0.027	II	Southern central
J052545.12+345253.4	19.128 ± 0.006	15.776 ± 0.010	14.143 ± 0.006	12.722 ± 0.025	11.569 ± 0.023	12.030	6.937 ± 0.113	12.291 ± 0.032	11.541 ± 0.032	I	Southern central
J052532.61+343959.8	15.165 ± 0.005	14.123 ± 0.002	13.833 ± 0.004	12.963 ± 0.028	12.560 ± 0.033	10.966 ± 0.171	8.102	13.342 ± 0.035	13.007 ± 0.024	II	Southern central
J052451.42+344407.4	15.642 ± 0.004	14.359 ± 0.003	13.585 ± 0.003	12.752 ± 0.024	12.215 ± 0.023	10.612 ± 0.162	8.010 ± 0.368	12.773 ± 0.030	12.318 ± 0.017	II	Southern central
J052544.57+345017.9	14.832 ± 0.003	13.785 ± 0.002	13.412 ± 0.003	12.774 ± 0.032	12.203 ± 0.029	8.697 ± 0.035	5.909 ± 0.059	12.919 ± 0.040	12.336 ± 0.031	II	Southern central
J052533.03+345648.2	15.948 ± 0.005	14.681 ± 0.004	13.953 ± 0.005	12.872 ± 0.028	12.302 ± 0.026	8.621 ± 0.046	6.111 ± 0.092	12.636 ± 0.044	12.072 ± 0.035	II	Southern central
J052431.32+350323.0	14.824 ± 0.003	13.790 ± 0.002	13.254 ± 0.003	12.631 ± 0.025	12.120 ± 0.025	11.192	8.672	12.927 ± 0.042	12.523 ± 0.028	II	Southern central
J052638.58+343832.0	15.752 ± 0.004	14.556 ± 0.003	13.782 ± 0.004	12.831 ± 0.026	12.264 ± 0.026	10.373 ± 0.138	7.770	12.515 ± 0.040	12.177 ± 0.034	II	Southern central
SSTGLMCG170.6571 −00.2763	14.360 ± 0.051	12.852 ± 0.042	11.856 ± 0.034	⋯	⋯	⋯	⋯	9.930 ± 0.049	9.061 ± 0.027	I	Western
J052147.25+363913.3	17.607 ± 0.011	16.097 ± 0.017	14.836 ± 0.010	13.116 ± 0.025	13.116 ± 0.024	13.116 ± 0.075	13.116 ± 0.481	13.418 ± 0.039	12.593 ± 0.037	I	Western
J052011.01+363642.6	18.452 ± 0.013	16.510 ± 0.025	15.025 ± 0.012	13.824 ± 0.028	13.824 ± 0.028	13.824 ± 0.079	13.824 ± 0.174	13.294 ± 0.040	12.481 ± 0.029	I	Western
J051850.66+364604.5	18.637 ± 0.008	16.323 ± 0.017	14.506 ± 0.007	13.045 ± 0.030	13.045 ± 0.023	13.045 ± 0.046	13.045 ± 0.098	12.841 ± 0.052	11.986 ± 0.026	I	Western
J052154.76+363902.6	18.328 ± 0.004	15.495 ± 0.010	13.747 ± 0.004	12.585 ± 0.024	12.585 ± 0.020	12.585 ± 0.023	12.585 ± 0.039	12.012 ± 0.031	10.961 ± 0.033	I	Western
SSTGLMCG170.8113 +00.0141	19.093 ± 0.027	17.260 ± 0.045	15.989 ± 0.025	⋯	⋯	⋯	⋯	14.313 ± 0.046	13.373 ± 0.042	I	Western
SSTGLMCG170.7275 −00.1034	12.518 ± 0.027	11.344 ± 0.026	10.770 ± 0.024	⋯	⋯	⋯	⋯	9.956 ± 0.080	9.307 ± 0.084	II	Western
SSTGLMCG170.6601 −00.2456	14.513 ± 0.002	13.102 ± 0.001	12.385 ± 0.002	⋯	⋯	⋯	⋯	11.689 ± 0.133	11.134 ± 0.084	II	Western
J052138.86+363154.6	16.478 ± 0.008	15.289 ± 0.008	14.498 ± 0.007	14.291 ± 0.031	14.291 ± 0.032	14.291 ± 0.139	14.291 ± 0.348	13.774 ± 0.047	13.197 ± 0.034	II	Western
SSTGLMCG170.3771 −00.4082	16.108 ± 0.009	15.095 ± 0.005	14.648 ± 0.008	⋯	⋯	⋯	⋯	13.750 ± 0.044	13.393 ± 0.039	II	Western
J051901.53+364619.3	15.901 ± 0.005	14.647 ± 0.004	14.001 ± 0.005	13.217 ± 0.025	13.217 ± 0.025	13.217 ± 0.049	13.217 ± 0.037	12.939 ± 0.036	12.428 ± 0.034	II	Western
SSTGLMCG170.6607 −00.2330	16.877 ± 0.009	15.559 ± 0.010	14.638 ± 0.009	⋯	⋯	⋯	⋯	13.459 ± 0.050	12.781 ± 0.037	II	Western
J052124.92+363943.2	15.412 ± 0.004	14.254 ± 0.003	13.508 ± 0.003	12.571 ± 0.024	12.571 ± 0.022	12.571 ± 0.030	12.571 ± 0.025	12.380 ± 0.094	11.560 ± 0.077	II	Western
J052112.72+364002.1	17.519 ± 0.012	15.782 ± 0.013	14.949 ± 0.011	14.615 ± 0.033	14.615 ± 0.046	14.615	14.615	14.280 ± 0.051	13.869 ± 0.038	II	Western
J052104.02+364018.4	14.856 ± 0.003	13.735 ± 0.002	13.244 ± 0.003	12.633 ± 0.024	12.633 ± 0.023	12.633 ± 0.103	12.633 ± 0.251	12.526 ± 0.062	12.091 ± 0.025	II	Western
SSTGLMCG170.6534 −00.2514	18.094 ± 0.015	16.395 ± 0.022	15.193 ± 0.014	⋯	⋯	⋯	⋯	13.632 ± 0.052	13.035 ± 0.040	II	Western
J052036.29+362359.4	16.998 ± 0.014	15.875 ± 0.013	15.297 ± 0.013	14.207 ± 0.048	14.207 ± 0.048	14.207 ± 0.156	14.207 ± 0.406	14.167 ± 0.050	13.496 ± 0.054	II	Western
J052036.16+362354.8	16.983 ± 0.012	15.699 ± 0.011	15.121 ± 0.012	14.580 ± 0.063	14.580 ± 0.074	14.580 ± 0.348	14.580	14.113 ± 0.041	13.596 ± 0.048	II	Western
	13.536 ± 0.002	13.226 ± 0.001	12.914 ± 0.002	⋯	⋯	⋯	⋯	12.473 ± 0.031	12.279 ± 0.024	II	Western

Table 4
(Continued)

ID	J(1.25 μm) (mag)	H(1.65 μm) (mag)	K_s(2.17 μm) (mag)	$W1$(3.4 μm) (mag)	$W2$(4.6 μm) (mag)	$W3$(12 μm) (mag)	$W4$(22 μm) (mag)	[3.6] (mag)	[4.5] (mag)	Class	Region
(1)	(2)	(3)	(4)	(5)	(6)	(7)	(8)	(9)	(10)	(11)	(12)
SSTGLMCG170.0648 −00.4499											
J052142.24+364112.4	15.653 ± 0.007	14.695 ± 0.005	14.308 ± 0.007	13.891 ± 0.037	13.891 ± 0.038	13.891 ± 0.190	13.891	13.892 ± 0.044	13.580 ± 0.044	II	Western
J052200.03+363809.0	17.243 ± 0.017	16.100 ± 0.015	15.493 ± 0.016	14.861 ± 0.039	14.861 ± 0.049	14.861 ± 0.327	14.861	14.666 ± 0.040	14.099 ± 0.043	II	Western
SSTGLMCG170.8281 +00.0070	15.606 ± 0.003	14.100 ± 0.003	13.286 ± 0.003	⋯	⋯	⋯	⋯	12.294 ± 0.040	11.839 ± 0.045	II	Western
J052203.64+363838.1	16.491 ± 0.010	15.465 ± 0.009	14.930 ± 0.010	13.895 ± 0.027	13.895 ± 0.033	13.895	13.895	14.152 ± 0.055	13.777 ± 0.043	II	Western
SSTGLMCG170.8326 +00.0236	14.796 ± 0.003	13.834 ± 0.002	13.386 ± 0.003	⋯	⋯	⋯	⋯	12.710 ± 0.042	12.459 ± 0.038	II	Western
SSTGLMCG170.9449 +00.0712	15.721 ± 0.006	14.774 ± 0.005	14.242 ± 0.006	⋯	⋯	⋯	⋯	13.314 ± 0.049	12.991 ± 0.049	II	Western
J052201.51+363600.2	14.465 ± 0.002	13.442 ± 0.002	12.872 ± 0.002	11.834 ± 0.022	11.834 ± 0.022	11.834 ± 0.040	11.834 ± 0.148	11.846 ± 0.037	11.437 ± 0.025	II	Western
J052155.68+362323.6	15.615 ± 0.006	14.667 ± 0.005	14.223 ± 0.006	13.529 ± 0.026	13.529 ± 0.031	13.529 ± 0.077	13.529 ± 0.473	13.545 ± 0.030	13.170 ± 0.026	II	Western
J052132.58+361120.6	15.189 ± 0.007	14.717 ± 0.004	14.558 ± 0.007	14.403 ± 0.031	14.403 ± 0.058	14.403	14.403	14.396 ± 0.039	13.967 ± 0.087	II	Western
J052258.30+362733.8	⋯	16.073 ± 0.014	16.003 ± 0.028	14.157 ± 0.030	14.157 ± 0.048	14.157	14.157	14.474 ± 0.060	14.262 ± 0.068	II	Western
J052019.62+363622.8	18.279	17.344	14.281 ± 0.062	9.884 ± 0.020	7.997 ± 0.019	4.914 ± 0.011	2.323 ± 0.012	9.521 ± 0.042	8.308 ± 0.025	I	Western
J052009.53+363554.3	19.022 ± 0.011	16.422 ± 0.024	14.761 ± 0.010	12.839 ± 0.024	11.568 ± 0.022	8.786 ± 0.033	6.723 ± 0.097	12.586 ± 0.041	11.575 ± 0.036	I	Western
J052112.61+363921.7	⋯	16.590 ± 0.023	13.795 ± 0.004	11.219 ± 0.032	9.516 ± 0.021	7.407 ± 0.020	4.801 ± 0.061	10.828 ± 0.037	9.760 ± 0.022	I	Western
J051900.82+364948.2	13.950 ± 0.001	12.914 ± 0.001	12.188 ± 0.001	11.000 ± 0.023	9.762 ± 0.021	6.491 ± 0.016	4.228 ± 0.022	10.715 ± 0.028	9.591 ± 0.058	I	Western
J051811.79+370204.4	15.085 ± 0.002	13.574 ± 0.002	12.478 ± 0.002	10.999 ± 0.024	9.826 ± 0.021	7.136 ± 0.017	4.802 ± 0.032	10.693 ± 0.034	9.833 ± 0.025	I	Western
J052151.23+363914.1	15.877	14.423 ± 0.062	12.527 ± 0.031	10.668 ± 0.021	9.184 ± 0.019	7.097 ± 0.016	4.285 ± 0.031	10.473 ± 0.109	9.452 ± 0.043	I	Western
J052149.65+363846.5	17.282 ± 0.004	15.191 ± 0.008	13.624 ± 0.004	11.916 ± 0.023	10.538 ± 0.021	7.895 ± 0.022	5.368 ± 0.040	11.123 ± 0.031	10.285 ± 0.030	I	Western
J052132.70+362747.5	15.410 ± 0.004	14.351 ± 0.003	13.781 ± 0.004	12.905 ± 0.024	12.320 ± 0.025	9.675 ± 0.062	7.101 ± 0.109	12.809 ± 0.028	12.314 ± 0.024	II	Western
J051903.38+363940.6	14.860 ± 0.003	13.910 ± 0.002	13.063 ± 0.003	11.738 ± 0.022	10.998 ± 0.020	9.237 ± 0.037	6.797 ± 0.069	11.612 ± 0.032	10.965 ± 0.026	II	Western
J051909.03+364343.5	14.152 ± 0.002	13.288 ± 0.001	12.837 ± 0.002	12.419 ± 0.025	12.018 ± 0.023	9.471 ± 0.044	7.245 ± 0.124	12.349 ± 0.038	12.077 ± 0.036	II	Western
J052104.69+363959.6	14.294 ± 0.002	13.126 ± 0.001	12.681 ± 0.002	12.128 ± 0.023	11.583 ± 0.021	9.202 ± 0.034	5.680 ± 0.045	12.346 ± 0.045	12.116 ± 0.025	II	Western
J052104.71+363854.3	14.995 ± 0.003	13.844 ± 0.003	13.318 ± 0.003	12.722 ± 0.026	12.295 ± 0.024	10.437 ± 0.098	8.082 ± 0.302	12.457 ± 0.033	12.186 ± 0.021	II	Western
J052027.40+363529.5	16.542 ± 0.002	14.107 ± 0.003	12.698 ± 0.002	11.658 ± 0.023	10.453 ± 0.021	8.312 ± 0.025	6.183 ± 0.063	11.330 ± 0.037	10.536 ± 0.022	II	Western
J052102.97+364140.0	14.642 ± 0.003	13.689 ± 0.002	13.233 ± 0.003	12.630 ± 0.024	12.028 ± 0.024	10.064 ± 0.078	8.374 ± 0.296	12.504 ± 0.032	12.057 ± 0.021	II	Western
J051953.13+363841.4	14.352 ± 0.002	13.247 ± 0.002	12.600 ± 0.002	11.582 ± 0.023	10.668 ± 0.021	7.689 ± 0.021	5.226 ± 0.031	11.163 ± 0.026	10.481 ± 0.025	II	Western
J051929.09+364359.9	13.525 ± 0.001	12.457 ± 0.001	11.841 ± 0.001	11.171 ± 0.023	10.569 ± 0.022	8.382 ± 0.025	5.951 ± 0.054	10.977 ± 0.054	10.515 ± 0.029	II	Western
J052029.05+365339.7	11.758 ± 0.026	11.426 ± 0.032	11.065 ± 0.020	10.438 ± 0.024	9.945 ± 0.020	8.372 ± 0.025	6.532 ± 0.071	10.332 ± 0.029	9.936 ± 0.020	II	Western
J051855.54+364559.5	16.858 ± 0.001	14.063 ± 0.003	12.045 ± 0.001	10.167 ± 0.024	8.886 ± 0.021	6.745 ± 0.017	4.196 ± 0.022	9.922 ± 0.041	8.950 ± 0.036	II	Western
J051853.98+364616.0	14.107 ± 0.003	13.400 ± 0.002	13.097 ± 0.002	12.581 ± 0.024	12.307 ± 0.024	10.620 ± 0.112	6.240 ± 0.055	12.817 ± 0.035	12.768 ± 0.033	II	Western
J052159.13+363631.6	15.619 ± 0.003	14.112 ± 0.003	13.484 ± 0.003	12.793 ± 0.024	11.977 ± 0.022	9.064 ± 0.041	6.044 ± 0.055	12.566 ± 0.035	12.000 ± 0.025	II	Western
J052149.55+363910.4	15.410 ± 0.002	13.740 ± 0.002	12.852 ± 0.002	12.166 ± 0.023	11.556 ± 0.022	9.748 ± 0.052	6.318 ± 0.091	11.897 ± 0.029	11.530 ± 0.035	II	Western
J052200.37+363856.1	15.559 ± 0.002	13.822 ± 0.002	12.665 ± 0.002	11.615 ± 0.023	10.846 ± 0.020	8.649 ± 0.030	6.592 ± 0.085	11.213 ± 0.045	10.744 ± 0.030	II	Western
J052147.49+364042.4	14.392 ± 0.002	13.403 ± 0.002	12.815 ± 0.002	12.046 ± 0.023	11.507 ± 0.021	9.532 ± 0.058	7.826 ± 0.188	11.964 ± 0.035	11.572 ± 0.037	II	Western
J052151.47+364557.6	14.516 ± 0.002	13.518 ± 0.002	12.968 ± 0.002	12.250 ± 0.025	11.363 ± 0.021	9.157 ± 0.035	7.273 ± 0.130	12.020 ± 0.034	11.326 ± 0.027	II	Western
J052039.21+370144.7	15.381 ± 0.005	14.581 ± 0.005	13.818 ± 0.004	12.549 ± 0.024	12.066 ± 0.022	9.689 ± 0.052	6.663 ± 0.070	12.650 ± 0.062	12.246 ± 0.031	II	Western

Note. The IR photometric magnitudes of the identified YSO candidates. Column 1 lists the YSO ID from the database of *WISE* and *Spitzer*. Columns 2–4 list the photometric magnitudes of the 2MASS J, H, and K_s bands. Columns 5–8 list the photometric magnitudes of the *WISE* $W1$, $W2$, $W3$, and $W4$ bands. Columns 9 and 10 list the photometric magnitudes of the *Spitzer* IRAC [3.6 μm] and [4.5 μm] bands. Column 11 lists the classification of the YSOs. Column 12 lists the region where the YSOs are identified. For the photometric magnitudes without uncertainties, the values presented here are the upper limits.

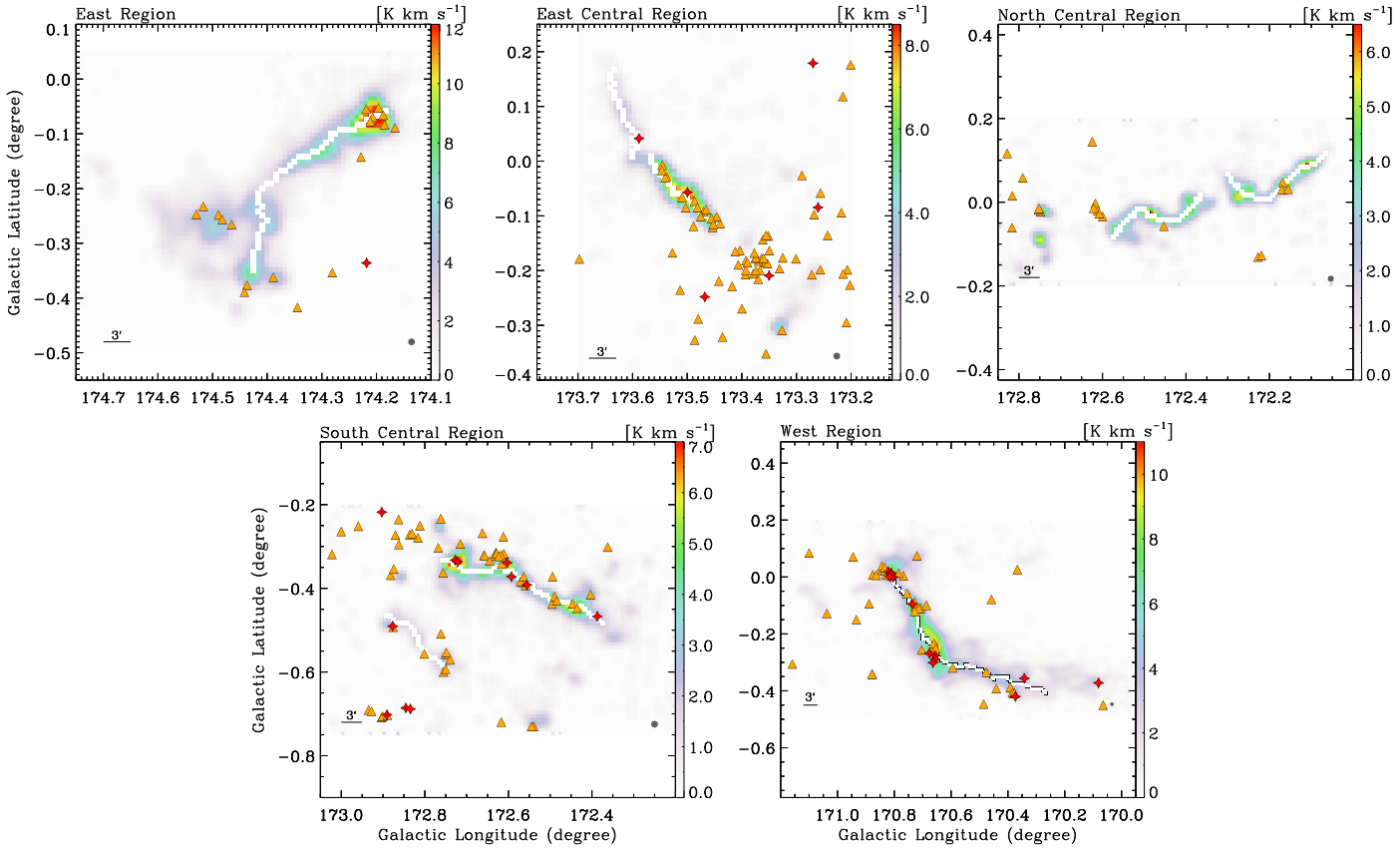

Figure 23. Distributions of YSO candidates identified in each region. The red stars represent Class I objects, and the yellow triangles represent Class II objects. The solid white lines show the positions of filaments. The backgrounds are the ^{13}CO integrated intensity maps of each region.

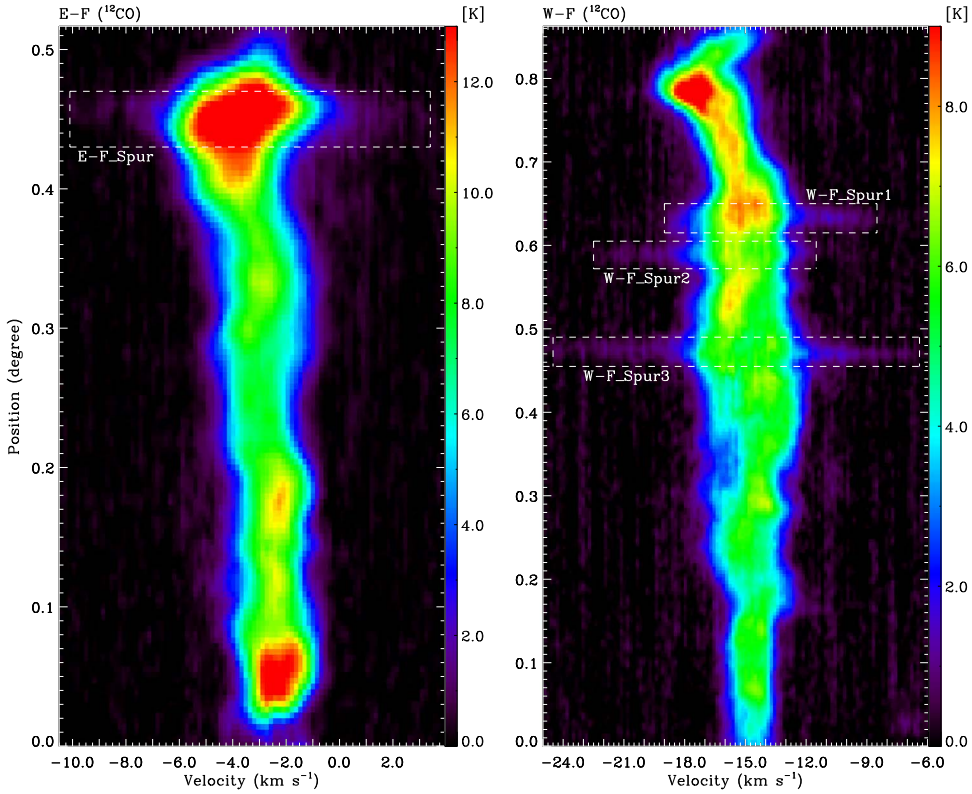

Figure 24. The ^{12}CO *PV* plots of E-F and W-F extracted along the directions of the solid arrowed lines and with the widths of the dashed boxes shown in Figures 6 and 14. The dashed rectangles indicate the positions of *PV* spur structures.

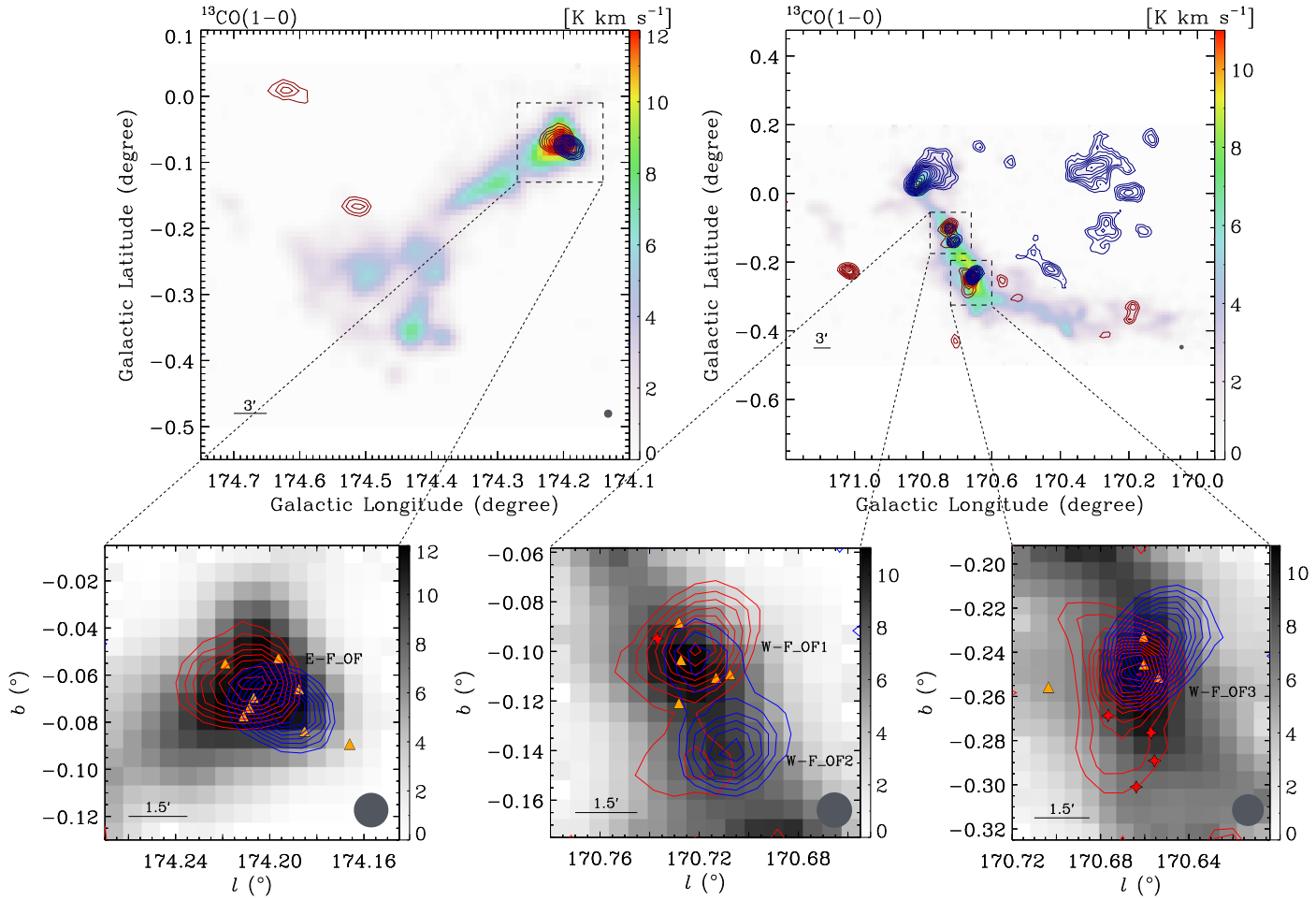

Figure 25. The ^{12}CO contours of the identified outflows with the backgrounds of the ^{13}CO integrated intensity maps. The red contours represent the redshifted lobes of the outflows, and the blue contours represent the blueshifted lobes of the outflows. The red stars in the bottom panels represent Class I objects, and the yellow triangles represent Class II objects.

Table 5
Properties of Outflows

Outflow	v_{center} (km s^{-1})	Δv_{blue} (km s^{-1})	Δv_{red} (km s^{-1})	$N_{H_2,blue}$ (10^{19} cm^{-2})	$N_{H_2,red}$ (10^{19} cm^{-2})	M_{blue} ($M_\odot$)	M_{red} ($M_\odot$)	P_{out} ($M_\odot$ km s^{-1})	E_{out} (10^{45} erg)
(1)	(2)	(3)	(4)	(5)	(6)	(7)	(8)	(9)	(10)
E-F_OF	−3.43	[−11.59, −6.92]	[0.39, 3.97]	4.35	2.43	0.79	1.39	16.81	1.28
W-F_OF1	−15.22	⋯	[−12.07, −5.79]	⋯	2.63	⋯	1.35	12.74	1.19
W-F_OF2	−15.05	[−22.86, −18.38]	⋯	2.52	⋯	0.95	⋯	7.41	0.58
W-F_OF3	−15.22	[−25.24, −18.21]	[−11.98, −6.19]	3.87	3.43	1.67	2.35	37.93	3.57

Note. Properties of identified outflows. Column 2 is the velocity of the line center. Columns 3 and 4 are the velocity ranges of the blue and red line wings. Columns 5 and 6 are the mean H_2 column densities of the blue and red lobes. Columns 7 and 8 are the masses of the blue and red lobes. Column 9 is the total momentum of the outflow. Column 10 is the total energy of the outflow.

display discontinuous features, only concentrating on the densest parts.

Based on the excitation temperature (with mean values ranging from 6.16 to 9.60 K) and H_2 column density traced by the ^{13}CO emission (with mean values ranging from 0.70×10^{21} to 6.53×10^{21} cm^{-2}) of the identified filaments, we derive the ^{13}CO LTE line mass to be from 20.24 to 161.91 $M_\odot$ pc^{-1}. We obtain the radial density profiles of filaments and find that most profiles present Gaussian-like shapes in the inner parts. The Gaussian fits to the inner parts lead to a mean FWHM width of 1.13 ± 0.01 pc.

After comparing LTE line mass with critical line mass, we find that the thermal pressure is not enough to support the fragmentation of filaments, and turbulence should be the dominant support against radial collapse. Most filaments have virial parameters smaller than 2 and thus are gravitationally bound. Four filaments (E-F, EC-F(S), SC-F(N), and W-F) have LTE line masses close to the virial line mass. The relationship of LTE mass and virial mass can be fitted as a power law of $M_{Vir} \propto M_{LTE}^{0.66\pm0.10}$.

We investigate the CO clumps in each region and find that 64% of them are associated with the filaments. The virialized clumps found in E-F and W-F are consistent with the locations

of the velocity oscillations, indicating that fragmentation could happen within these gravitationally bound filaments. Based on the complementary IR data, we find that most filaments have associated Class II objects. Only a few Class I objects are found to be located on EC-F(S), SC-F(N), and W-F. The locations of Class I objects are also the places where virialized clumps are found.

We suggest that these four filaments, E-F, EC-F(S), SC-F (N), and W-F, may contain star-forming activity, based on the evidence of detection in the $C^{18}O$ emission, virial parameters close to 1, and associated virialized clumps and Class I objects. Especially for E-F and W-F, where we have detected ^{12}CO outflows with typical mass, momentum, and energy of 1.42 $M_{\odot}$, 18.72 $M_{\odot}$ km s^{-1}, and 1.65 $\times$ 10^{45} erg, respectively, the star-forming activity should have already taken place.

We are grateful to all of the members of the Milky Way Imaging Scroll Painting CO line survey group, especially the staff of Qinghai Radio Station of PMO at Delingha, for the support during the observations. This work was supported by the National Key Research & Development of China under grant 2017YFA0402702 and funding from the European Unions Horizon 2020 research and innovation program under grant agreement No. 639459 (PROMISE). We acknowledge the support from NSFC through grant Nos. 11473069, 11503086, and 11629302. This research has made use of the NASA/IPAC Infrared Science Archive, which is operated by the Jet Propulsion Laboratory, California Institute of Technology, under contract with the National Aeronautics and Space Administration.

Software: GILDAS (Guilloteau & Lucas 2000; Pety 2005; Gildas Team 2013).

ORCID iDs

Fang Xiong https://orcid.org/0000-0001-8653-8992
Qizhou Zhang https://orcid.org/0000-0003-2384-6589
Min Fang https://orcid.org/0000-0001-8060-1321

References

Abergel, A., Boulanger, F., Mizuno, A., & Fukui, Y. 1994, ApJL, 423, L59
André, P., Di Francesco, J., Ward-Thompson, D., et al. 2014, in Protostars and Planets VI, ed. H. Beuther et al. (Tuscon, AZ: Univ. Arizona Press), 27
André, P., Men'shchikov, A., Bontemps, S., et al. 2010, A&A, 518, L102
Arce, H. G., Shepherd, D., Gueth, F., et al. 2007, in Protostars and Planets V, ed. B. Reipurth, D. Jewitt, & K. Keil (Tucson, AZ: Univ. Arizona Press), 245
Arzoumanian, D., André, P., Didelon, P., et al. 2011, A&A, 529, L6
Arzoumanian, D., André, P., Könyves, V., et al. 2019, A&A, 621, A42
Arzoumanian, D., André, P., Peretto, N., & Könyves, V. 2013, A&A, 553, A119
Arzoumanian, D., Shimajiri, Y., Inutsuka, S.-i., Inoue, T., & Tachihara, K. 2018, PASJ, 70, 96
Bachiller, R., & Tafalla, M. 1999, NATO Adv. Sci. Inst. Ser. C, 540, 227
Bally, J., Langer, W. D., Stark, A. A., & Wilson, R. W. 1987, ApJL, 312, L45
Benjamin, R. A., Churchwell, E., Babler, B. L., et al. 2003, PASP, 115, 953
Beuther, H., Ragan, S. E., Johnston, K., et al. 2015, A&A, 584, A67
Blake, G. A., Sutton, E. C., Masson, C. R., & Phillips, T. G. 1987, ApJ, 315, 621
Bontemps, S., André, P., Könyves, V., et al. 2010, A&A, 518, L85
Busquet, G., Zhang, Q., Palau, A., et al. 2013, ApJL, 764, L26
Carey, S. J., Clark, F. O., Egan, M. P., et al. 1998, ApJ, 508, 721
Carey, S. J., Feldman, P. A., Redman, R. O., et al. 2000, ApJL, 543, L157
Carey, S. J., Noriega-Crespo, A., Mizuno, D. R., et al. 2009, PASP, 121, 76
Castets, A., & Langer, W. D. 1995, A&A, 294, 835
Chandrasekhar, S., & Fermi, E. 1953, ApJ, 118, 116
Churchwell, E., Babler, B. L., Meade, M. R., et al. 2009, PASP, 121, 213
Contreras, Y., Garay, G., Rathborne, J. M., & Sanhueza, P. 2016, MNRAS, 456, 2041
Cox, N. L. J., Arzoumanian, D., André, P., et al. 2016, A&A, 590, A110
Devereux, N. A., & Young, J. S. 1990, ApJ, 359, 42
Fiege, J. D., & Pudritz, R. E. 2000, MNRAS, 311, 85
Fischera, J., & Martin, P. G. 2012, A&A, 542, A77
Frerking, M. A., Langer, W. D., & Wilson, R. W. 1982, ApJ, 262, 590
Garden, R. P., Hayashi, M., Gatley, I., Hasegawa, T., & Kaifu, N. 1991, ApJ, 374, 540
Gibson, D., Plume, R., Bergin, E., Ragan, S., & Evans, N. 2009, ApJ, 705, 123
Gildas Team 2013, Astrophysics Source Code Library, GILDAS: Grenoble Image and Line Data Analysis Software, , ascl:1305.010
Goldsmith, P. F., Heyer, M., Narayanan, G., et al. 2008, ApJ, 680, 428
Gong, Y., Mao, R. Q., Fang, M., et al. 2016, A&A, 588, A104
Guilloteau, S., & Lucas, R. 2000, in ASP Conf. 217, Imaging at Radio through Submillimeter Wavelengths, ed. J. G. Mangum & S. J. E. Radford (San Francisco, CA: ASP), 299
Gutermuth, R. A., Megeath, S. T., Myers, P. C., et al. 2009, ApJS, 184, 18
Hacar, A., Kainulainen, J., Tafalla, M., Beuther, H., & Alves, J. 2016, A&A, 587, A97
Hacar, A., & Tafalla, M. 2011, A&A, 533, A34
Hacar, A., Tafalla, M., & Alves, J. 2017, A&A, 606, A123
Hacar, A., Tafalla, M., Forbrich, J., et al. 2018, A&A, 610, A77
Hatchell, J., Richer, J. S., Fuller, G. A., et al. 2005, A&A, 440, 151
Henning, T., Linz, H., Krause, O., et al. 2010, A&A, 518, L95
Inoue, T., & Fukui, Y. 2013, ApJL, 774, L31
Inoue, T., Hennebelle, P., Fukui, Y., et al. 2018, PASJ, 70, S53
Jackson, J. M., Finn, S. C., Chambers, E. T., Rathborne, J. M., & Simon, R. 2010, ApJL, 719, L185
Jackson, J. M., Rathborne, J. M., Shah, R. Y., et al. 2006, ApJS, 163, 145
Kauffmann, J., Bertoldi, F., Bourke, T. L., Evans, N. J., II, & Lee, C. W. 2008, A&A, 487, 993
Kirk, H., Klassen, M., Pudritz, R., et al. 2015, ApJ, 802, 75
Koch, E. W., & Rosolowsky, E. W. 2015, MNRAS, 452, 3435
Koenig, X. P., & Leisawitz, D. T. 2014, ApJ, 791, 131
Könyves, V., André, P., Men'shchikov, A., et al. 2015, A&A, 584, A91
Kusune, T., Sugitani, K., Nakamura, F., et al. 2016, ApJL, 830, L23
Li, F. C., Xu, Y., Wu, Y. W., et al. 2016, AJ, 152, 92
Li, G.-X., Urquhart, J. S., Leurini, S., et al. 2016, A&A, 591, A5
Loren, R. B. 1989, ApJ, 338, 925
Lu, X., Zhang, Q., Liu, H. B., et al. 2018, ApJ, 855, 9
MacLaren, I., Richardson, K. M., & Wolfendale, A. W. 1988, ApJ, 333, 821
Mangum, J. G., & Shirley, Y. L. 2015, PASP, 127, 266
Marsh, K. A., Whitworth, A. P., & Lomax, O. 2015, MNRAS, 454, 4282
Marsh, K. A., Whitworth, A. P., Lomax, O., et al. 2017, MNRAS, 471, 2730
Men'shchikov, A., André, P., Didelon, P., et al. 2010, A&A, 518, L103
Milam, S. N., Savage, C., Brewster, M. A., Ziurys, L. M., & Wyckoff, S. 2005, ApJ, 634, 1126
Molinari, S., Swinyard, B., Bally, J., et al. 2010, A&A, 518, L100
Myers, P. C. 2009, ApJ, 700, 1609
Nagasawa, M. 1987, PThPh, 77, 635
Nakamura, F., Hanawa, T., & Nakano, T. 1993, PASJ, 45, 551
Ossenkopf-Okada, V., & Stepanov, R. 2019, A&A, 621, A5
Ostriker, J. 1964, ApJ, 140, 1056
Palmeirim, P., André, P., Kirk, J., et al. 2013, A&A, 550, A38
Peretto, N., & Fuller, G. A. 2009, A&A, 505, 405
Pety, J. 2005, in Proc. Meeting of the French Astronomical and Astrophysical Society, SF2A-2005 , ed. F. Casoli et al. (Paris: French Astronomical and Astrophysical Society)
Planck Collaboration, Adam, R., Ade, P. A. R., et al. 2016, A&A, 586, A135
Planck Collaboration, Ade, P. A. R., Aghanim, N., et al. 2015, A&A, 576, A104
Ragan, S. E., Henning, T., Tackenberg, J., et al. 2014, A&A, 568, A73
Reid, M. J., Dame, T. M., Menten, K. M., et al. 2016, ApJ, 823, 77
Richer, J. S., Shepherd, D. S., Cabrit, S., Bachiller, R., & Churchwell, E. 2000, in Protostars and Planets IV, ed. V. Mannings, A. P. Boss, & S. S. Russell (Tucson, AZ: Univ. Arizona Press), 867
Sanhueza, P., Jackson, J. M., Zhang, Q., et al. 2017, ApJ, 841, 97
Santos, F. P., Busquet, G., Franco, G. A. P., Girart, J. M., & Zhang, Q. 2016, ApJ, 832, 186
Saral, G., Hora, J. L., Willis, S. E., et al. 2015, ApJ, 813, 25
Schneider, S., & Elmegreen, B. G. 1979, ApJS, 41, 87
Schuller, F., Menten, K. M., Contreras, Y., et al. 2009, A&A, 504, 415
Scoville, N. Z., Sargent, A. I., Sanders, D. B., et al. 1986, ApJ, 303, 416
Shan, W., Yang, J., Shi, S., et al. 2012, ITTST, 2, 593
Skrutskie, M. F., Cutri, R. M., Stiening, R., et al. 2006, AJ, 131, 1163

Solomon, P. M., Rivolo, A. R., Barrett, J., & Yahil, A. 1987, ApJ, 319, 730
Sousbie, T. 2011, MNRAS, 414, 350
Tomisaka, K. 1995, ApJ, 438, 226
Van Loo, S., Keto, E., & Zhang, Q. 2014, ApJ, 789, 37
Vuong, M. H., Montmerle, T., Grosso, N., et al. 2003, A&A, 408, 581
Wang, K., Testi, L., Ginsburg, A., et al. 2015, MNRAS, 450, 4043
Wang, K., Zhang, Q., Testi, L., et al. 2014, MNRAS, 439, 3275
Werner, M. W., Roellig, T. L., Low, F. J., et al. 2004, ApJS, 154, 1
Whitney, B., Benjamin, R., Meade, M., et al. 2011, BAAS, 43, 241.16
Williams, J. P., de Geus, E. J., & Blitz, L. 1994, ApJ, 428, 693
Wright, E. L., Eisenhardt, P. R. M., Mainzer, A. K., et al. 2010, AJ, 140, 1868
Xiong, F., Chen, X., Yang, J., et al. 2017, ApJ, 838, 49
Zucker, C., Battersby, C., & Goodman, A. 2015, ApJ, 815, 23